



Deliverable 15.8: Synthesis of irradiation results under repository conditions

Work Package 15

This project has received funding from the European Union's Horizon 2020 research and innovation programme 2014-2018 under grant agreement N°847593.



<http://www.ejp-urad.eu/>

Document information

Project Acronym	EURAD
Project Title	European Joint Programme on Radioactive Waste Management
Project Type	European Joint Programme (EJP)
EC grant agreement No.	847593
Project starting / end date	1st June 2019 – 30 May 2024
Work Package No.	15
Work Package Title	Container Corrosion under Disposal conditions
Work Package Acronym	ConCorD
Deliverable No.	15.8
Deliverable Title	Synthesis of irradiation results under repository conditions
Lead Beneficiary	Subatech / CNRS
Contractual Delivery Date	December 2023
Actual Delivery Date	14/05/2024
Type	Report
Dissemination level	Public
Authors	Lola Sarrasin (Subatech), Muhammad Faiz Al Rasyid Tisyadi (Subatech), Abdesselam Abdelouas (Subatech), Šárka Šachlová (UJV), Vlastislav Kašpar (UJV), David Dobrev (UJV), Daniel Götz (UJV), Kateřina Kolomá (UJV), Petr Večerník (UJV), Milan Zuna (UJV), Ursula Alonso (CIEMAT), Mikel Diéguez (CIEMAT), Carla Soto (CIEMAT), Ana María Fernández (CIEMAT), Miguel García-Gutiérrez (CIEMAT), Pedro Valdivieso (CIEMAT), Tiziana Missana (CIEMAT)

To be cited as:

Sarrasin L., Tisyadi M.F., Abdelouas A., Šachlová Š., Kašpar V., Dobrev D., Götz D., Kolomá K., Večerník P., Zuna M., Alonso U., Diéguez M., Soto C., Fernández A.M., Gutiérrez M.G., Valdivieso P., Missana T. (2024): Synthesis of irradiation results under repository conditions. Final version as of 13.05.2024 of deliverable D.15.8 of the HORIZON 2020 project EURAD. EC Grant agreement no: 847593.

Disclaimer

All information in this document is provided "as is" and no guarantee or warranty is given that the information is fit for any particular purpose. The user, therefore, uses the information at its sole risk and liability. For the avoidance of all doubts, the European Commission or the individual Colleges of EURAD (and their participating members) has no liability in respect of this document, which is merely representing the authors' view.

Acknowledgement

This document is a deliverable of the European Joint Programme on Radioactive Waste Management (EURAD). EURAD has received funding from the European Union’s Horizon 2020 research and innovation programme under grant agreement No 847593.

Status of deliverable		
	By	Date
Delivered (Lead Beneficiary)	Abdesselam Abdelouas - SUBATECH	07/05/2024
Verified (WP Leader)	Nikitas Diomidis	13/05/2024
Reviewed (Reviewers)	Fraser King, Christina Lilja, Valérie Maillot, Satoru Suzuki, Mehran Behazin, Guido Bracke	21/03/2024
Approved (PMO)	Bernd Grambow	14/05/2024
Submitted to EC (Coordinator)	Andra (Coordinator)	14/05/2024

Executive Summary

The objective of the present study was the assessment of irradiation-accelerated corrosion of canister materials in realistic environments and irradiation conditions. The experiments were designed to represent the conditions expected in the repository with the inclusion of buffer materials at different saturation levels, groundwater compositions, temperature, and redox conditions. The collaboration between partners in this work provides additional information on the potential influence of the type of bentonite used, the nature of the irradiation source (Co-60, Cs-137), the effect of water saturation (63%-100% relative humidity), and the dose rate (0.4-657 Gy/hr).

Contrasting results were obtained about the effect of gamma irradiation on steel corrosion. The corrosion was enhanced in experiments conducted by SUBATECH and CIEMAT while the steel corrosion decreased under irradiation at high temperature (150°C) in experiments conducted by UJV but at quite different experimental conditions. Experiments conducted under controlled water saturation at 25°C (SUBATECH) showed a strong effect of radiation, which enhanced steel corrosion compared to reference non-irradiated samples. Nevertheless, the lowest percentage of relative humidity (63% RH) showed the highest corrosion rate (as high as 250 µm per year), which then decreased with increasing water saturation (100%). In the case of experiments using C-steel contacting compacted MX-80 bentonite at different saturation levels (60 and 100%) (CIEMAT), the corrosion rate of C-steel was higher in the presence of gamma irradiation relative to reference samples and increased with increasing saturation from 60% to 100% (in contrast to experiments conducted by SUBATECH). Similar experiments by CIEMAT using copper showed only minor corrosion under irradiation. Experiments with steel and fully saturated MX-80 or BCV bentonite conducted by UJV showed lower corrosion rates under irradiation compared to reference experiments at 150°C, while gamma radiation had no significant effect on steel corrosion at lower temperatures (90°C and room temperature). Nevertheless, similarities were found for all experimental configurations such as the decrease of corrosion rate with increasing time or typical corrosion products such as siderite, magnetite or Fe-hydroxides. Furthermore, no clear impact of the dose rate or the type of irradiation (Co-60 vs. Cs-137) on the steel corrosion was found. Finally, we conclude that radiolysis effect on steel corrosion should be investigated further to elucidate the mechanisms governing the corrosion process (corrosion rate and products) under anticipated repository conditions. Among the subjects to be developed we distinguish water vapor radiolysis, in particular the yield of radiolysis products as a function of relative humidity, which impacts the corrosion kinetics. Also, the combined role of temperature and radiolysis on steel corrosion needs to be better understood.

Table of contents

Executive Summary	4
Table of contents	5
List of figures	8
List of Tables	12
Glossary.....	14
1. Methodology of tests performed by Subatech on C-steel corrosion in non-saturated water conditions.....	15
1.1 Overview	15
1.2 Test specimens (C-steel and clay)	15
1.2.1 Steel preparation	15
1.2.2 Clay preparation	16
1.3 Salt solutions	17
1.4 Assembly	17
1.5 Experimental setup	18
1.6 Irradiation	19
1.7 Disassembly and post-test analysis	19
1.7.1 Disassembly	19
1.7.2 Gas measurement using micro-gas chromatography (μ -GC)	20
1.7.3 Mass loss	20
1.7.4 Surface SEM-EDX.....	21
1.7.5 XRD	21
1.8 Results.....	21
1.8.1 Gas chromatography	21
1.8.2 Visual inspections	23
1.8.3 Mass loss	27
1.8.4 Surface SEM-EDX.....	30
1.8.5 Surface XRD.....	32
1.9 Discussion	35
2. Experiments performed by UJV.....	37
2.1 Overview.....	37
2.2 Test specimens.....	37
2.2.1 Carbon steel samples	37
2.2.2 Bentonite samples	37
2.2.3 Saturation solution	37

2.3	Experimental design, irradiation and loading conditions	38
2.4	Disassembly	40
2.5	Post-test analysis.....	40
2.5.1	Post-test analysis of steel.....	40
2.5.2	Post-test analysis of bentonite.....	41
2.6	Results of tests performed by UJV	42
2.6.1	Mass loss.....	42
2.6.2	SEM-EDX and LOM.....	44
2.6.3	Profilometry.....	51
2.6.4	XRD and Raman spectroscopy	55
2.6.5	Bentonite chemical composition	56
2.6.6	Cation exchange capacity	58
2.6.7	Water leachates.....	59
2.7	Discussion	62
2.7.1	Factors affecting steel corrosion rate	62
2.7.2	Factors affecting composition of corrosion products	62
2.8	Summary and conclusions of UJV testing.....	63
3	Corrosion tests performed by CIEMAT under gamma irradiation conditions	64
3.1	Overview.....	64
3.2	Test specimens.....	65
3.2.1	Metal coupons	65
3.2.2	Metal cleaning procedure	67
3.2.3	Selected iron and copper oxides	67
3.2.4	Bentonite.....	68
3.2.5	Bentonite porewater.....	68
3.3	Experimental set-ups.....	69
3.3.1	Set-up to analyse powder materials: unirradiated and gamma irradiated.....	69
3.3.2	Set-up to analyse metal corrosion in water: unirradiated and gamma irradiated	70
3.3.3	Metal coupons / bentonite samples	73
3.3.1	Set up to analyse magnetite / bentonite samples: unirradiated and gamma irradiated	74
3.4	Irradiation conditions	78
3.5	Disassembly and post-test analyses	79
3.5.1	Disassembly and visual inspection.....	79
3.5.2	Water analyses	80
3.5.3	Mass loss measurements.....	80
3.6	Results by CIEMAT	82

EURAD Deliverable 15.8 – Synthesis of irradiation results under repository conditions

3.6.1	Irradiated powder materials	82
3.6.2	Metal corrosion in different bentonite porewaters: unirradiated and irradiated	84
3.6.3	Magnetite / bentonite samples.....	87
3.6.4	Metal canister / bentonite samples	88
3.6.5	Irradiated compacted bentonite samples (no metal)	93
3.7	Summary and conclusions by CIEMAT	94
References	95
Appendix	99

List of figures

Figure 1 Grinding/Polishing Machine.	15
Figure 2 Diamond Wire Saw.....	16
Figure 3 The chamber used for relative humidity control.	16
Figure 4 Photos of steel and clay assembly.....	17
Figure 5 Cell and samples setup (a) steel+clay, (b) steel alone.	18
Figure 6 Irradiation cell.	18
Figure 7 GSM D1 Gamma ¹³⁷ Cs irradiator.	19
Figure 8 Cutting of the corroded steel sample.	20
Figure 9 Gas chromatography.....	20
Figure 10 Comparison of H ₂ Production Rates for Steel Alone Samples.	21
Figure 11 Comparison of average H ₂ production rate as a function of relative humidity of steel alone samples.	22
Figure 12 Comparison of H ₂ Production Rates for Steel and Clay Samples.	23
Figure 13 Comparison of average H ₂ production rate as a function of relative humidity of steel and clay samples.	23
Figure 14 Visual inspection and optical microscope images of steel alone samples irradiated for 10 days in three conditions (a) RH63% (F-40), (b) RH76% (F-36), and (c) RH99% (F-38).	24
Figure 15 Visual inspection and microscope images of steel+bentonite samples (atmosphere face) after 42 days of irradiation (a)RH63% (F-31), (b) RH76% (F27), (c)RH99% (F29)	24
Figure 16 Visual inspection and microscope images of steel+bentonite samples (clay face) after 42 days of irradiation (a)RH63% (F-31), (b) RH76% (F28 with F27 microscope image), (c)RH99% (F29)	25
Figure 17 Visual inspection of steel+bentonite samples after 26 days of exposure (a)RH63% (F-69), (b) RH76% (F70), (c)RH99% (F66) (top: atmosphere face, bottom: bentonite face)	26
Figure 18 Corrosion layer transported in clay from unirradiated sample F25	26
Figure 19 Visual inspection of 99% humidity samples with irradiation time of (a) 10 days and (b) 36 days.	27
Figure 20 Steel only sample exposed to ambient humidity (a) F46 sample with (b) microscope image, (c) untreated sample.....	27
Figure 21 Corrosion rate of steel coupons hydrated at 25°C and different RH as a function of time. In the presence of radiation at a dose rate of 400 Gy/h	29
Figure 22 Corrosion rate of steel coupons in contact with bentonite hydrated at 25°C and different RH as a function of time.	30
Figure 23 Corrosion rate of steel coupons in contact with bentonite hydrated at 25°C for 21 days and different RH.....	30
Figure 24 SEM photo of steel hydrated at 76% RH (side facing the atmosphere) for 14 days in the experiment with bentonite (Sample F58).....	31
Figure 25 EDX spectrum of steel hydrated at 63% RH for 10 days showing the presence of Fe, O and traces of Si and Ca.	31

Figure 26 EDX spectrum of steel hydrated at 63% RH for 10 days showing the presence of Fe, O and Cl.	32
Figure 27 Schematic of the reaction mechanisms and approximate time scales for production of various species during water radiolysis [Robira, 2018].....	36
Figure 28 Left – carbon steel disks, right – outer case of the canister in the Czech concept.	37
Figure 29 Left – corrosion cell, right – carbon steel samples inside of the corrosion cell.	38
Figure 30 Left – steel vessels containing steel cells connected by metal capillaries with saturation medium situated in the irradiation area, right - steel cell containing compacted BCV bentonite and carbon steel coupons during disassembly (cell no. 22).....	39
Figure 31 Corrosion rate of steel samples loaded at BCV bentonite at 150 °C , 90 °C and at laboratory temperature (RT) for 18 months. IR – irradiated, NIR – unirradiated.....	44
Figure 32 Corrosion rate of steel samples embedded at MX-80 bentonite heated up at 150 °C, 90 °C and at laboratory temperature (RT) for 18 months. IR – irradiated, NIR – unirradiated.....	44
Figure 33 Steel microstructure ferritic-pearlitic (left) and ferritic-pearlitic with spheroidal areas (right) (cell no. 2).....	45
Figure 34 Corrosion layer on the surface of irradiated steel samples embedded in BCV bentonite heated at 150 °C for 12 months (cell no. 5). SEM images including red line indicating position of the profile analysed by EDS (left) and the profile analysis.....	46
Figure 35 Corrosion layer on the surface of unirradiated steel samples embedded in BCV bentonite heated up at 150 °C for 12 months (cell no. 6). SEM images including red line indicating position of the profile analysed by EDS (left) and the profile analysis.....	47
Figure 36 Corrosion layer on the surface of irradiated steel samples embedded in BCV bentonite heated up at 90 °C for 12 months (cell no. 14). SEM images including red line indicating position of the profile analysed by EDS (left) and the profile analysis (right).	48
Figure 37 Corrosion layer on the surface of unirradiated steel samples embedded in BCV bentonite heated up at 90 °C for 12 months (cell no. 15). SEM images including red line indicating position of the profile analysed by EDS (left) and the profile analysis (right).	49
Figure 38 Corrosion layer on the surface of irradiated steel samples embedded in MX80 bentonite heated at 150 °C for 18 months (cell no. 9). SEM images including red line indicating position of the profile analysed by EDS (left) and the profile analysis.	50
Figure 39 Corrosion layer on the surface of irradiated steel samples embedded in BCV bentonite heated at 150 °C for 18 months (cell no. 9). SEM images including red line indicating position of the profile analysed by EDS (left) and the profile analysis.....	51
Figure 40 Comparison of the profilometry analysis of the BLANK steel sample (on the left) with unirradiated steel sample loaded in BCV bentonite at laboratory temperature for 12 months (on the right).....	52
Figure 41 Comparison of the profilometry analysis of steel samples embedded in BCV bentonite heated up at 150 °C and irradiated for 6 (cell no. 1), 9 (cell no. 3) and 12 (cell no. 5) with the unirradiated ones (cells no. 2, 4 and 6).	54
Figure 42 Comparison of the profilometry analysis of steel samples embedded in BCV bentonite heated up at 90 °C and irradiated for 9 (cell no. 12) and 12 (cell no. 14) with the unirradiated ones (cells no. 13 and 15).....	55
Figure 43 Fe ₂ O ₃ (a), MnO (b), CaO (c), MgO (d), K ₂ O (e) and Na ₂ O (f) content in original bentonite (BCV_2017_7) and bentonite heated up at 150 °C (150), 90 °C (90) and at ambient temperature (RT), irradiated (IR) or unirradiated (NIR).....	58

Figure 44 Concentration of Na⁺ (a), K⁺ (b), Ca²⁺ (c), Mg²⁺ (d), HCO₃⁻ (e), Cl⁻ (f) a SO₄²⁻ (g) in water leachates from BCV bentonite heated up at 150 °C (150), 90 °C (90) or laboratory temperature (RT), irradiated (IR) or unirradiated (NIR), loaded for 12 months..... 62

Figure 45 – (a) Carbon steel sample sent by Jacobs (UK) of material representative of canister design by NAGRA (CH). (b) Cylindrical test tubes extracted to obtain metal coupons of different diameter. (c) Carbon steel discs of 1.9 cm in diameter and 1.6 mm thickness used for irradiation experiments. 66

Figure 46 – (a) Cylindrical test tube reference T102 190°-224° of Cu-OFP, representative material of their canister design of SKB (SE) sent to CIEMAT (ES). (b) Example of Cu-OFP coupons of 1.9 cm in diameter and 1.6 mm thickness cut for irradiation experiments. 66

Figure 47 – Selected corrosion products. From Left to Right: Fe₂O₃, Fe₃O₄, Cu₂O and CuO commercial nano-powder oxides. 68

Figure 48 – (a) Powder FEBEX bentonite grounded and sieved to a fraction < 0.5 mm. (b) Example of compacted bentonite sample hydrated with porewater at desired saturation degree. 68

Figure 49 – Selected corrosion products, powder oxides in high-density polyethylene tubes for irradiation experiments. 69

Figure 50 – Samples of different metal coupons immersed in 5 mL of different bentonite porewater (PW-1.4, PW-1.6, composition in Table 8) or deionised water (DW) prepared in isotactic polypropylene tubes. 71

Figure 51 – Closed cell designed for samples simulating metal canister/bentonite interface: (a) PVC open cylinder, (b) compacted bentonite sample. (c) bentonite inserted in the PVC ring, (d) copper metal disc (e) copper disc placed on the surface of the clay tablet, (f) closed cell. 73

Figure 52 – Picture of sixteen closed cells installed with copper and carbon steel metal coupons, or magnetite oxide, placed over one surface of compacted bentonite samples, at different conditions (Table 22) prepared for gamma radiation experiments under aerobic conditions. 74

Figure 53 – (a) Samples introduced in a watertight metal container equipped to be introduced at a depth of 4 m into the irradiation pool facility to be placed in the circular compartments containing the ⁶⁰Co sources. (b). Samples inside CIEMAT’s Nayade ⁶⁰Co gamma irradiation pool facility. 78

Figure 54 – Picture of disassembling of a closed cell containing a sample simulating metal canister / bentonite interface after irradiation. 80

Figure 55 – XRD patterns measured on selected powder Cu and Fe oxides (Table 18) and on FEBEX bentonite, comparing unirradiated powder samples and gamma-irradiated at 14 kGy accumulated dose (dose rate 66 Gy/h). 83

Figure 56 – Comparative FT-IR spectra obtained on powder unirradiated FEBEX bentonite clay and after gamma-irradiation at 140 kGy (dose rate 697 Gy/h). The main bands and groups representative of di-octahedral smectites are indicated. 84

Figure 57 – Appearance of the Cu-OFP metal discs dismantled after immersion in bentonite porewaters (Table 17) and deionised water under three conditions: (Left) unirradiated (middle) gamma irradiated with accumulated dose of 14 kGy and (Right) gamma irradiated with accumulated dose of 140 kGy. Pictures showed the comparison of altered (uncleaned surfaces) and cleaned surfaces for mass loss measurements. 85

Figure 58 – Appearance of the C-steel metal discs dismantled after immersion in bentonite porewaters (Table 17) and deionised water under three conditions: (Left) unirradiated (middle) gamma irradiated with accumulated dose of 14 kGy and (Right) gamma irradiated with accumulated dose of 140 kGy. Pictures showed the comparison of altered (uncleaned surfaces) and cleaned surfaces for evaluating mass loss measurements. 85

Figure 59 – Metal concentrations measured in unfiltered solution after metal disc immersion in 5 mL of different bentonite porewaters PW1.4 and PW1.6 (Table 17) and in deionised water (DW) irradiated at different conditions (0, 14 kGy and 140 kGy). (a) Cu in solution in mg/l (Cu-OFP experiments) and (b) Fe in solution in mg/l (C-steel experiments). 87

Figure 60 – Comparison of XRD patterns measured on (red) magnetite contacting bentonite compacted sample at 1.4 g/cm³, hydrated at 100% saturation and gamma-irradiated at 14 kGy accumulated dose (dose rate 66 Gy/h) and on (black) unirradiated powder magnetite. 88

Figure 61 – Appearance of the Cu-OFP metal discs dismantled after contact with compacted bentonite at two compaction densities and with two degrees of water saturation, under three conditions: (Left) Unirradiated, (middle) Gamma irradiated with accumulated dose of 14 kGy ((right) Gamma irradiated with accumulated dose of 14 kGy. . Pictures show the discs altered after opening and later cleaned. 89

Figure 62 – Appearance of the C-steel metal discs dismantled after contact with compacted bentonite at two compaction densities and with two degrees of water saturation, under three conditions: (Left) Unirradiated, (middle) Gamma irradiated with accumulated dose of 14 kGy ((right) Gamma irradiated with accumulated dose of 14 kGy. .. Pictures show the discs altered after opening and later cleaned.89

Figure 63 Example of SEM images obtained on the surface of a C-steel disc of experiment reference T3-10, which corresponds to a sample contacted to compacted bentonite at 1.4 g/cm³ and 100% water content, irradiated at 14 kGy, where higher corrosion rate was measured. The number in the images are areas analysed by EDAX. 92

Figure 64 Comparative RAMAN spectra obtained on the bentonite surface of sample T3-12, corresponding to a C-steel disc contacting a compacted bentonite sample at 1.6 g/cm³ and 100 % hydrates. The spectra fits with that of a goethite sample measured at the same conditions. 93

Figure 65 Comparative XRD patterns measured on bentonite samples which were irradiated in compacted state (1.4 or 1.6 g/cm³) and full water saturated. 94

List of Tables

Table 1 Composition of the P235GH steel	15
Table 2 Composition of salt solutions and corresponding relative humidity values.	17
Table 3 Corrosion experiments of steel coupons under different experimental conditions (RH, time, and dose).....	28
Table 4 Reference corrosion experiments of steel.....	28
Table 5 Corrosion experiments of steel coupons in contact with bentonite under different experimental conditions (RH, time, and dose).	29
Table 6 Corrosion products formed in experiments with steel coupons under different experimental conditions (RH, time, and dose).	32
Table 7 Corrosion products formed in experiments with steel coupons in contact with bentonite under different experimental conditions (RH, time, and dose).	33
Table 8 Chemical composition of synthetic granitic water (Červinka et al. 2018).	38
Table 9 A list of experimental cells and loading conditions.	39
Table 10 Corrosion rates of steel samples given in $\mu\text{m y}^{-1}$. AVG – average, $\pm L$ – confidence interval of the Student's distribution at the significance level $\alpha = 0.05$, IR – irradiated, NIR – unirradiated, 6 (resp. 9, 12 or 18) – the length of heating period in months, MX80 – MX-80 bentonite.....	43
Table 11 Deviation from the reference Mean value and variance from reference point based on profilometry.	52
Table 12 Semiquantitative XRD of randomly oriented powder mounts.	56
Table 13 Chemical composition of BCV bentonite heated up at 150 °C (150), 90 °C (90) and at ambient temperature (RT), irradiated (IR) or unirradiated (NIR) (in wt.%). The data were recalculated to the 0.00 wt.% of loss of ignition.	57
Table 14 The CEC analysed spectroscopically (CEC_{vis}), the sum of exchangeable cations (CEC_{sum}) and the proportions of exchangeable cations in the BCV_input bentonite and BCV bentonite heated up to 150 °C (150), irradiated (IR) or unirradiated (NIR) for 6 (6m), 9 (9m), 12 (12m) and 18 months (18m).	59
Table 15 Concentration of water leachates in BCV_input and BCV heated up at 150 °C (150), 90 °C (90), ambient temperature (RT), irradiated (IR) and unirradiated (NIR).	59
<i>Table 16 – Composition of Cu-OFP sample reference T102 190° -224° provided by SKB (SE). Traces concentration indicated in part per million (ppm).</i>	<i>67</i>
<i>Table 17 – Chemical composition (M) of synthetic pore waters respectively prepared for FEBEX bentonite samples compacted at 1.4 (PW-1.4) and 1.6 g/cm³ (PW-1.6). Recipes from (Fernandez & Rivas, 2005).</i>	<i>69</i>
<i>Table 18 – Nature and conditions of selected powder materials that were characterised under three conditions: (i) unirradiated, (ii) gamma irradiated at accumulated dose of 14 kGy and (iii) gamma irradiated at accumulated dose of 140 kGy.</i>	<i>70</i>
<i>Table 19 – List of metal samples immersed in waters for irradiation. The table includes the type of sample according to the gamma radiation dose, the reference, the type of metal coupon or oxide, the bentonite type and compaction dry density (none in this case), the type of added water (Table 8), the saturation conditions and added volume, the redox conditions, temperature and type of device used for irradiation.</i>	<i>72</i>

<i>Table 20 – Dimensions and characteristics of compacted bentonite samples prepared at different compaction densities, with different water saturation degree (w.c. in %).</i>	74
<i>Table 21 – List of metal / bentonite samples prepared as reference unirradiated. The table includes the type of sample according to received radiation, the reference, the type of metal coupon or oxide included, the bentonite type and compaction dry density, the type of added water (Table 8), the saturation degree and water volume, the redox conditions, temperature and type of device used for irradiation.</i>	75
<i>Table 22 – List of metal / bentonite samples prepared for gamma-irradiation at 14 kGy. The table includes the type of sample according to received radiation, the reference, the type of metal coupon or oxide included, the bentonite type and compaction dry density, the type of added water (Table 8), the saturation degree and water volume, the redox conditions, temperature and type of device used for irradiation.</i>	76
<i>Table 23 – List of metal / bentonite samples prepared for gamma-irradiation at 140 kGy. The table includes the type of sample according to received radiation, the reference, the type of metal coupon or oxide included, the bentonite type and compaction dry density, the type of added water (Table 8), the saturation degree and water volume, the redox conditions, temperature and type of device used for irradiation.</i>	77
Table 24 – Corrosion rate determined for Cu-OFP and C-steel discs, immersed in 5 mL different bentonite porewaters (Table 17) and deionised water. Samples were unirradiated, irradiated at 14 kGy and irradiated at 140 kGy. Corrosion rates were estimated considering 12 days of experiment and are based on mass loss measurements. (n.d.: not determined)	86
Table 25 Corrosion rates determined for Cu-OFP and C-steel discs contacting compacted bentonite samples at two different compaction densities and hydration at two saturation degrees (w.c. %). Triplicate samples were unirradiated, irradiated at 14 kGy and irradiated at 140 kGy. Corrosion rates were estimated considering 12 days of experiment and are based on mass loss measurements.	91

Glossary

CIEMAT	Centro de Investigaciones Energéticas, Medioambientales y Tecnológicas
Cu-OFP	Oxygen-free phosphorus-doped copper
DGR	Deep Geological Repository
DW	Deionised water
FEBEX	Full-scale Engineered Barriers Experiment
HDPE	High density polyethylene
NAGRA	Swiss National Cooperative for the Disposal of Radioactive Waste
PW-1.4	Reference bentonite pore water at 1.4 g/cm ³ compaction density
PW-1.6	Reference bentonite pore water at 1.6 g/cm ³ compaction density
SKB	Swedish Nuclear Fuel and Waste Management Company
w.c.	water content

1. Methodology of tests performed by Subatech on C-steel corrosion in non-saturated water conditions

1.1 Overview

Unlike corrosion in saturated conditions, and according to the best of our knowledge, the literature on corrosion of steel in controlled unsaturated conditions under repository conditions is scarce. These unsaturated conditions are supposed to last for more or less long periods depending on the repository design and host rock properties, following repository closure. The canister may then be subjected to water vapour hydration in the presence of radiation. Hence, the experiments developed at Subatech are aimed at evaluating the atmospheric corrosion of carbon-steel under gamma radiation with and without the presence of clay.

1.2 Test specimens (C-steel and clay)

1.2.1 Steel preparation

The coupons used for these experiments were made of P235GH carbon steel. The steel composition is given in **Erreur ! Source du renvoi introuvable**. Table 1.

Table 1 Composition of the P235GH steel

Element	C	Mn	Si	P	S	Cr	Mo	Ni	Al	Cu	Nb	Ti	V	N
Wt. %	≤	=	≤	≤	≤	≤	≤	≤	≥	≤	≤	≤	≤	≤
	0.16	0.60-1.20	0.35	0.025	0.015	0.30	0.08	0.0	0.020	0.30	0.020	0.030	0.020	0.012

Carbon steel coupons of dimensions 20 x 10 x 2 mm are polished using the help of a grinding machine and silicon carbide grinding paper (Figure 1). The coupon was first polished using a P240 grit paper to flatten the surface of any large cracks or blemishes on the surface. After the initial grind, the coupon is polished with several steps to achieve the intended smoothness (until P4000, FEPA-P standards, 5 µm). This process is repeated for each side of the coupon.

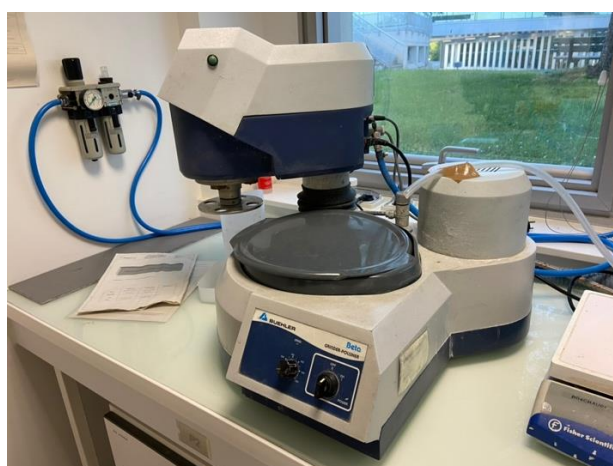


Figure 1 Grinding/Polishing Machine.

After the initial polishing/grinding, the sample is cut using a diamond wire saw for half the length to create two coupons of 10x10x2 mm in dimension (Figure 2). The freshly cut side of the sample is then polished to the same finish as the other sides. Lastly the sample goes through a final polishing step using 3 µm

diamond suspension on all sides. The dimension of the coupon is then measured using a digital vernier calliper.



Figure 2 Diamond Wire Saw.

1.2.2 Clay preparation

Granular Wyoming sodium bentonite (MX-80) provided by Nagra was used for this study. The sample initially consisted of a powder in which pellets of various sizes were present. For the experimental needs, the clay was crushed in a ceramic mortar and the grain size controlled with a 200 μm sieve to obtain a fine powder. The clay was then equilibrated to the desired relative humidity by placing it in a close container with saturated salt solution to control the relative humidity (Figure 3).

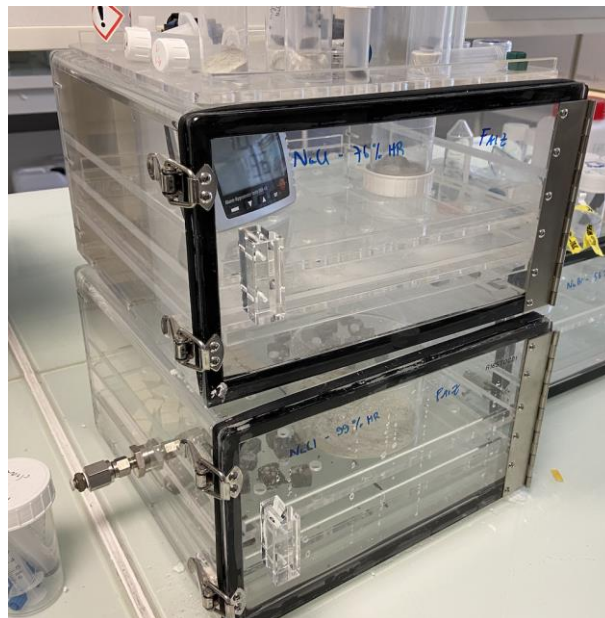


Figure 3 The chamber used for relative humidity control.

1.3 Salt solutions

The relative humidity was controlled during the experiments using salt solutions. The solutions were used to obtain clay with a given amount of water rather than adding and mixing solutions with the clay. The powdered clay was placed in a sealed box containing the salt solution until it reached the equilibrium before using in the experiments. The water content evolution inside the clay was followed by weighing and drying the clay in an oven at 105°C for at least 24 hours. The measurements showed that the clay needed at least 1 week in the humid environment to guarantee that equilibrium was reached.

The solutions used to control the relative humidity are given in Table 2. Saturated salt solutions were used to reach the different relative humidity values (63%, 76 %, 99%) [O'Brien, 1948; Young, 1967; Pitzer et al., 1979]. Over-saturated solution of NaBr and NaCl are used to achieve 63% and 76% RH respectively, while a 1.75% w/v diluted NaCl solution was used to achieve 99% RH. These solutions are used both for the purpose of clay hydration and maintaining the relative humidity inside of the irradiation cell.

Table 2 Composition of salt solutions and corresponding relative humidity values.

Salt	RH(%)	Reference	Note
Oversaturated NaBr	63	F E M O'Brien (1948)	According to the reference, NaBr should yield 57% RH however measurement shows 63%
Oversaturated NaCl	76	Young, J. F. (1967)	-
1.75% w/v NaCl	99	Pitzer, et al. (1979)	-

1.4 Assembly

Experiments involving clay require the sample to be formed into a pellet to achieve the desired compaction level. Target compaction level for this experiment is around 1.4 to 1.6 g/cm³ dry density. For steel+clay samples, the steel coupon sits on top of the pellet so that one side faces the atmosphere while the other face is in contact with the clay (Figure 4). Clay compaction is manually done using a pressing machine and formed into pellets with 20mm diameter. The pellet thickness varies depending on the level of hydration of the clay. Clay with higher humidity tends to be thinner after the compaction using the same initial clay mass (around 3 grams) due to the water content.

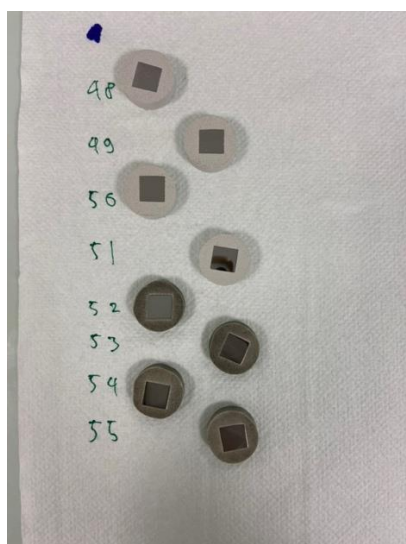


Figure 4 Photos of steel and clay assembly.

The samples were prepared the day the corrosion experiment started to avoid any corrosion due to the contact with the humid clay.

1.5 Experimental setup

- Irradiation cell assembly

Cells used in the experiment hold two sets of experiments (steel+clay or steel alone) (Figure 5). The steel coupon was placed on the top of the bentonite and pressed with one side facing bentonite and one side facing the head space of the cell. For steel+clay configuration, the samples are stacked vertically using sample holders with 3ml of salt solution placed beforehand underneath (Figure 5a). For steel only configuration, the steel coupons are placed above one cylindrical sample holder and a sample holder with slits which the coupon occupies (Figure 5b). As Figure 5 shows, in both configurations, each cell has two samples. Regarding the naming, samples are coded with the name of the operator and the sample number (e.g. sample F-10, meant the tenth coupon prepared by operator Faiz). The lists for each configuration of samples are found in the appendix.

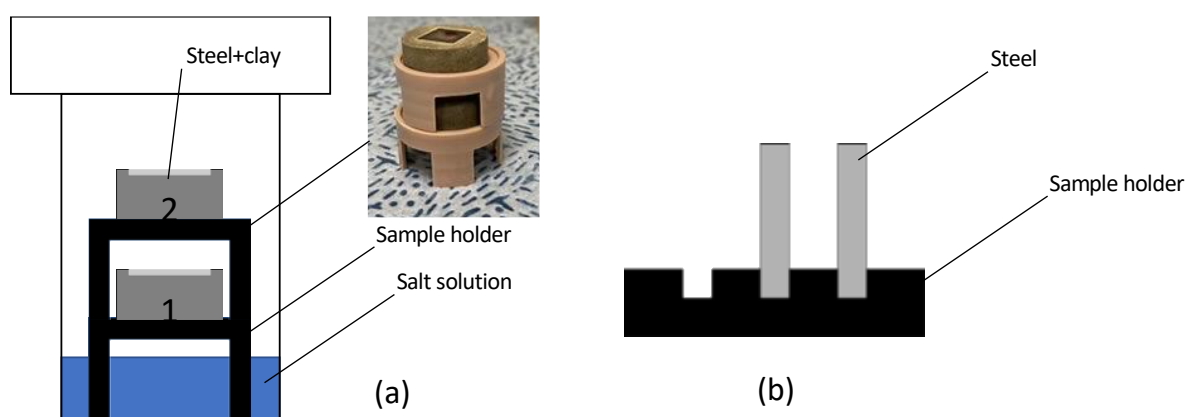


Figure 5 Cell and samples setup (a) steel+clay, (b) steel alone. The volume of the cell is 47.4 cm³, and the size of each coupon is 10 x 10 x 2 mm.

Details of the irradiation cell can be seen in Figure 6. Hence, for experiments conducted under argon atmosphere, the cell is purged with Ar gas at 0.2 bars for 10 minutes. For this process due to the presence of solution on the bottom of the cell, purging of the environment is only done in the head space reaching the solution, so no sparging of the solution is done, which does not exclude traces of oxygen.



Figure 6 Irradiation cell.

1.6 Irradiation

Gamma irradiation experiments have been conducted in a GSM D1 Gamma ^{137}Cs (120 TBq; $E_\gamma=0,66\text{MeV}$) located in the Arronax Cyclotron facility (France) (Figure 7). The experiments were conducted in the bottom of the sample compartment allowing a dose rate of 400 Gy/h, at room temperature (25°C) measured inside the irradiator. We chose a high dose rate to increase to exasperate the effect of radiolysis on steel corrosion given the time constraint to allow as many experiments to be conducted as possible.

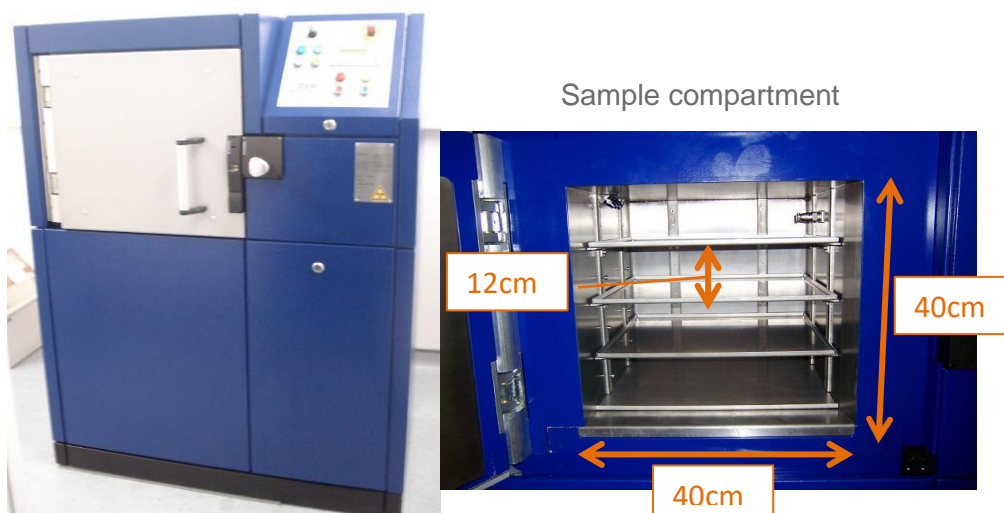


Figure 7 GSM D1 Gamma ^{137}Cs irradiator.

At the end of the run, the sample is dried of any potential water or humidity on the surface using drying paper and then transferred and stored inside a glovebox under Argon condition to avoid further corrosion. The sample is only taken out of the glovebox for analysis or manipulations.

1.7 Disassembly and post-test analysis

1.7.1 Disassembly

After the irradiation was stopped, the gas inside the cell was measured using an Agilent $\mu\text{-GC}$, to check for leakage. The cells were then opened and the steel coupon removed from the compacted clay using tweezers. The samples were gently cleaned from the residual clay and dried using ethanol. They were then stored under Ar in a glovebox with a controlled environment. The saturated salt solution is discarded and the cells washed with water in an ultrasonic bath.

The coupons were analysed by XRD and then cut in 3 pieces in order to perform various analysis with each sample (Figure 8).

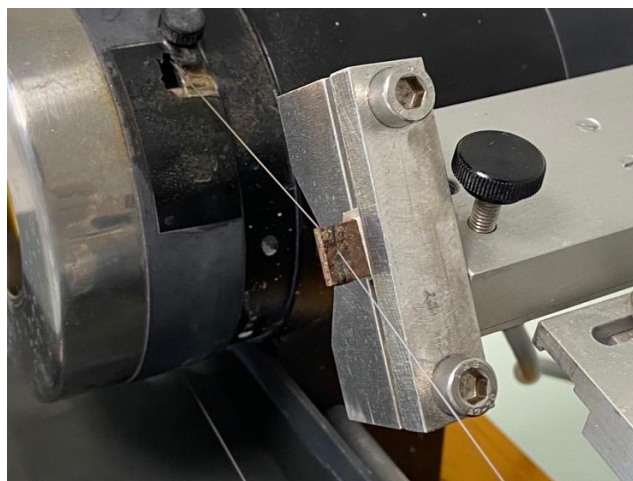


Figure 8 Cutting of the corroded steel sample.

The steel samples were cut in 3 pieces using the diamond wire saw (Figure 8), the first larger part was used for XRD measurement, then for the mass loss measurement, the second small part was used to observe the surface of the sample and the third part was used to analyse the cross-section. The latter were prepared by embedding the metal in Araldite resin and polished up to 4 μm using SiC disks.

1.7.2 Gas measurement using micro-gas chromatography ($\mu\text{-GC}$)

The gaseous atmosphere in the sealed irradiation cell was analysed using μGC (Agilent Technologies 490) (Figure 9). Its H_2 measurement channel consists of a heated injector, a 4m 5A molsieve column, using Argon as vector gas, and a TCD detector. H_2 was quantified using standards.

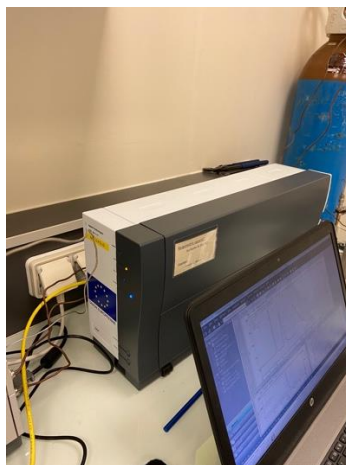


Figure 9 Gas chromatography.

1.7.3 Mass loss

The corrosion rates were evaluated by mass loss measurement. The steel sample is immersed in 15% HCl inhibited with 5g/L hexamethyltetramine. The sample was then rinsed with demineralized water and neutralized with sodium carbonate before a last rinse with demineralized water and a drying with ethanol. The mass was recorded with an accuracy of 10^{-4} g.

The corrosion rate calculated in μm per year is calculated by the following formula described in NACE (2012) and Malaret (2022):

$$CR (\mu\text{m}/\text{y}) = \frac{3650 \times \Delta m (\text{mg})}{d (\text{g} \cdot \text{cm}^{-3}) \times S (\text{cm}^2) \times t (\text{d})}$$

Where:

CR: corrosion rate ($\mu\text{m}/\text{y}$)

Δm : calculated as the difference between the initial mass (m_0) and the final mass (m_f) in mg

t: specific contact time measured in hours in days

A: total surface area measured of the steel sample in cm^2

d: density measured in grams per cubic centimetre (g/cm^3) (7.87 for P235GH steel)

1.7.4 Surface SEM-EDX

The micro morphology was investigated by Scanning Electron Microscope (SEM) (JEOL JSM-5800LV) operating at 15kV. Quantitative elemental mappings with Energy Dispersive X-Ray (EDX) were performed with a SAMx (NumeriX+) energy dispersive spectrometer mounted on the SEM.

1.7.5 XRD

Crystalline phases were identified by X-Ray Diffraction (XRD) (D8 Advance Bruker with Ni filtered Cu $K\alpha = 1.5406 \text{ \AA}$, 25mA, 100W) performed on matrix samples. The XRD patterns were collected in the 2θ range $10\text{-}85^\circ$ with 0.018° steps and 3 s per step.

1.8 Results

1.8.1 Gas chromatography

Examples of results of hydrogen measurement in the headspace of the irradiation cells can be seen in Figure 10-Figure 13. One can see that the hydrogen concentration seems to increase with increasing time and dose in particular between 0 and 21 days and stabilize after for experiment at 63% RH, likely due to water radiolysis. Steel corrosion may also contribute into hydrogen production. Oxygen was not detected excluding any leakage from the air. The first batch of samples is the steel alone samples. For higher RH (76%, 99%) only 2 data points were obtained due to experimental limitations.

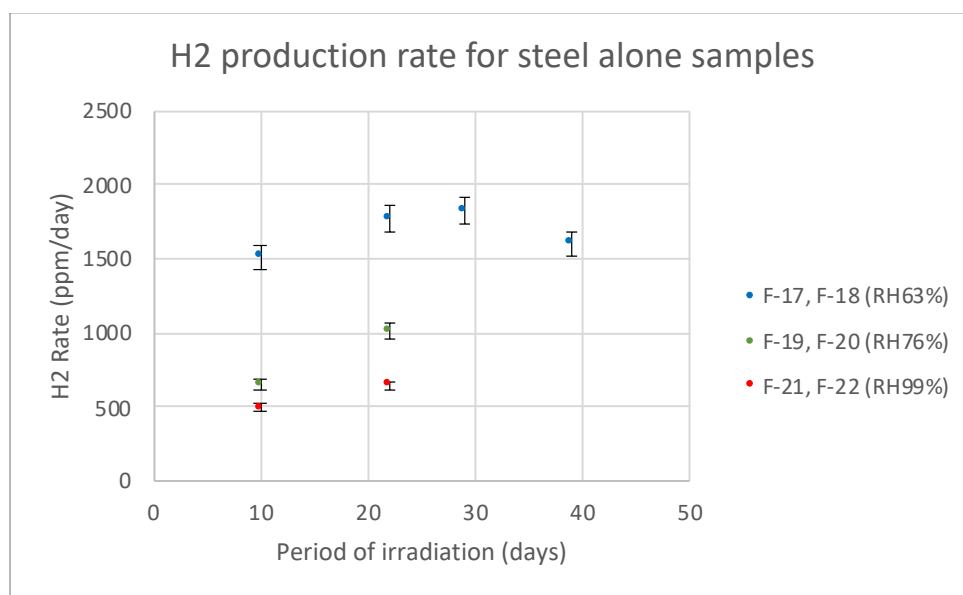


Figure 10 Comparison of H₂ Production Rates for Steel Alone Samples.

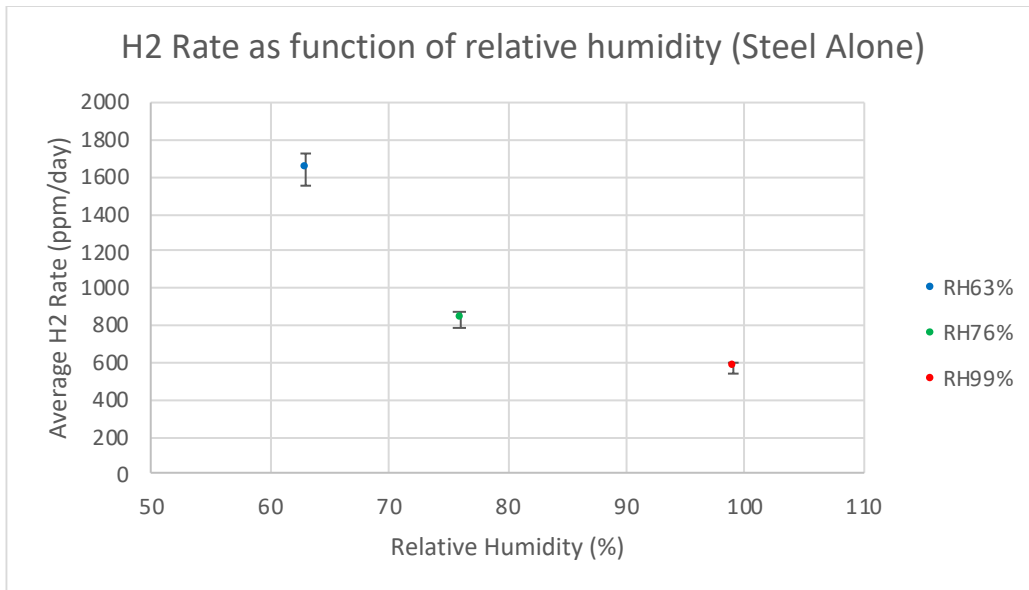


Figure 11 Comparison of average H₂ production rate as a function of relative humidity of steel alone samples.

As can be seen from the Figure 11, samples in lower relative humidity (RH 63%) have higher production rate of H₂ gas. Figure 10 shows that initially there seems to be an increase of the H₂ production until the period of thirty t days which is followed by a decrease afterwards. This might indicate the length of time needed before the corrosion begins stabilizing. Taking the average rate of H₂ production into account (Figure 11), we can see a decrease as the relative humidity goes up.

The next batch of samples are the steel and clay samples. Figure 12 shows the evolution of the H₂ production rate of samples in each relative humidity conditions. A similar trend can be seen in that samples with lower relative humidity have higher production rate of H₂. It can be seen there are some fluctuations along the irradiation period, however, there seems to be a tendency to stabilize after around 30 days of irradiation. It can also be seen that for F-29 and F-30, the first two points of the data has an unusually low value, and this can be attributed to a leak found in the irradiation cell that is fixed after the GC measurement on day 22 of the irradiation. Figure 13 shows the comparison of average H₂ production as a function of relative humidity, which shows a similar tendency as the steel alone samples, which is that as the relative humidity goes up the production of H₂ goes down.

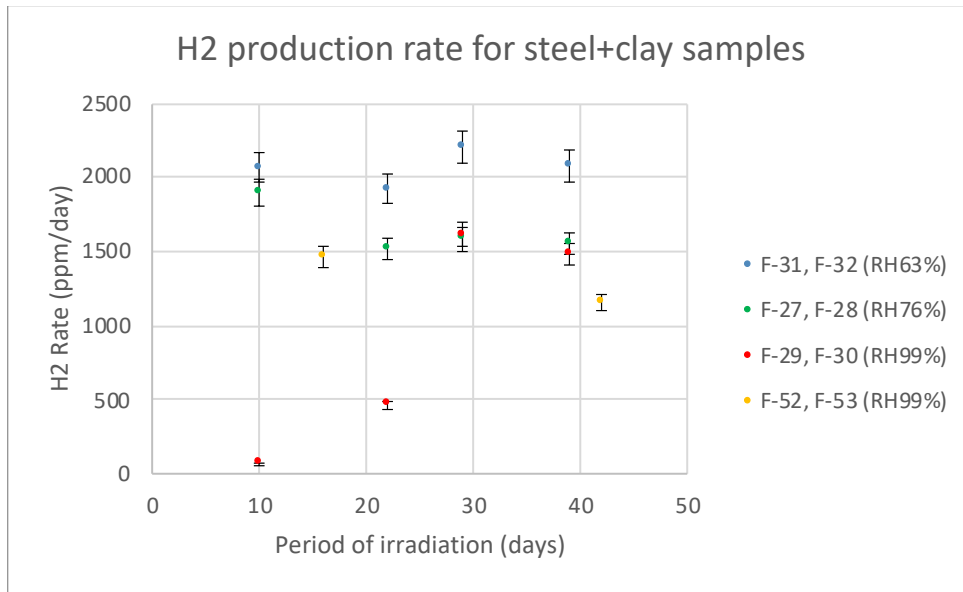


Figure 12 Comparison of H₂ Production Rates for Steel and Clay Samples.

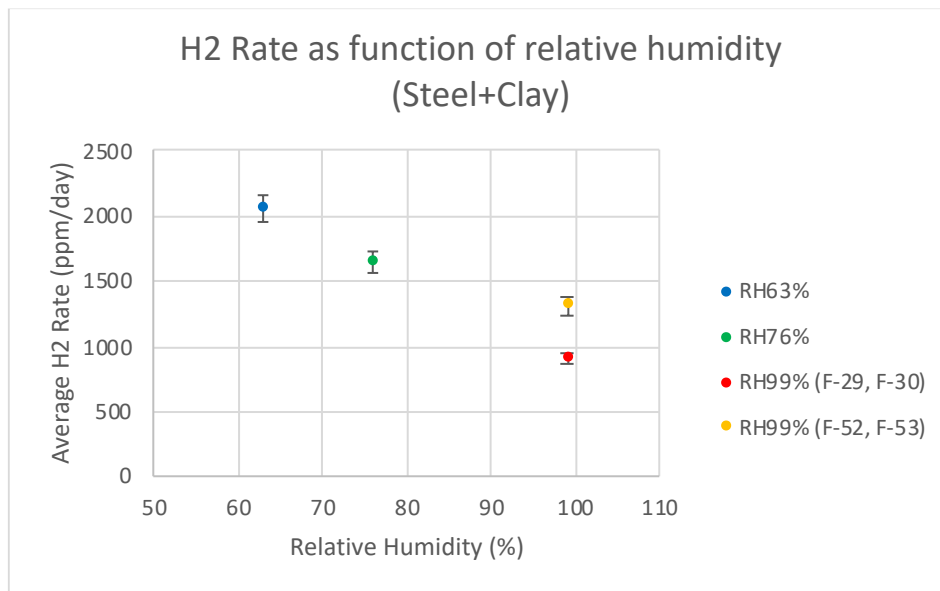


Figure 13 Comparison of average H₂ production rate as a function of relative humidity of steel and clay samples.

1.8.2 Visual inspections

Visual inspection is done for samples in all configurations. Visual inspections show results that with lower relative humidity, more corrosion layer is developed than higher humidity. Figure 14 show the comparison between samples in steel alone configuration for different relative humidity values.

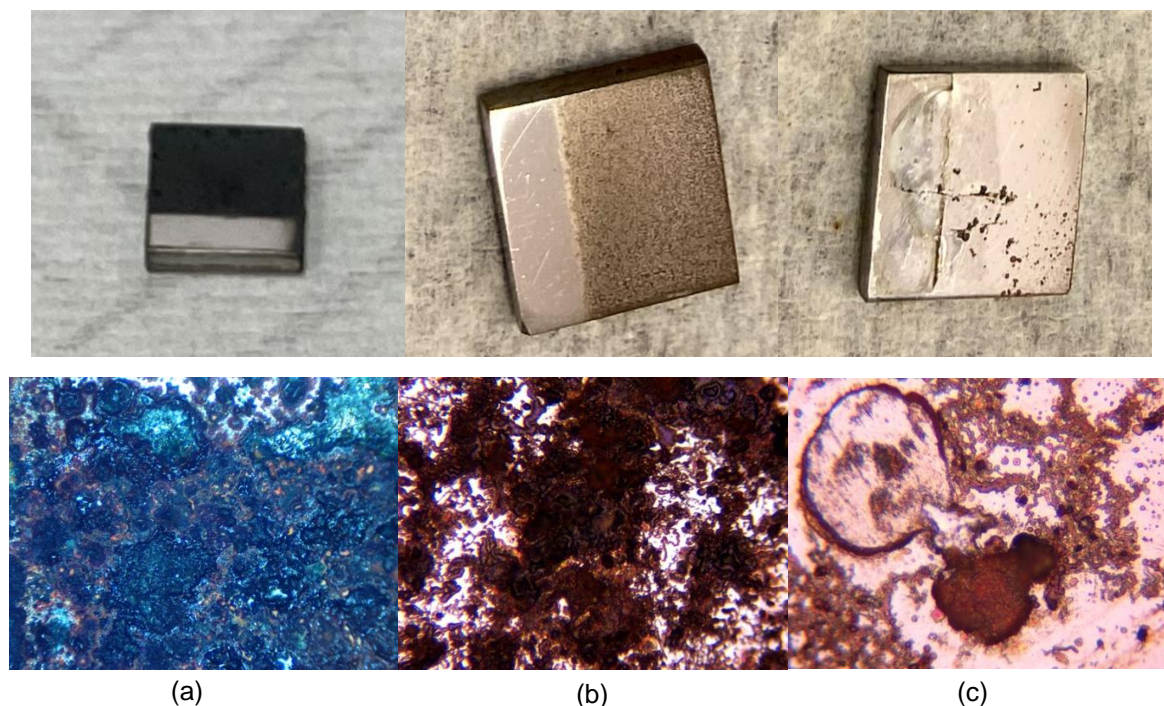


Figure 14 Visual inspection and optical microscope images of steel alone samples irradiated for 10 days in three conditions (a) RH63% (F-40), (b) RH76% (F-36), and (c) RH99% (F-38).

Figure 14 shows the surface appearance of corroded steel coupons at different RH. One can see that the corrosion layer seems to be more developed at the lowest RH. Thicker and darker corrosion layer can be seen in the sample with lower relative humidity, while very little corrosion is detected on samples of higher humidity.

Alongside the steel alone samples, samples with bentonite are also visually inspected. Figure 15 shows the corrosion layer of the atmosphere face of the steel coupon while Figure 16 shows the clay facing side.

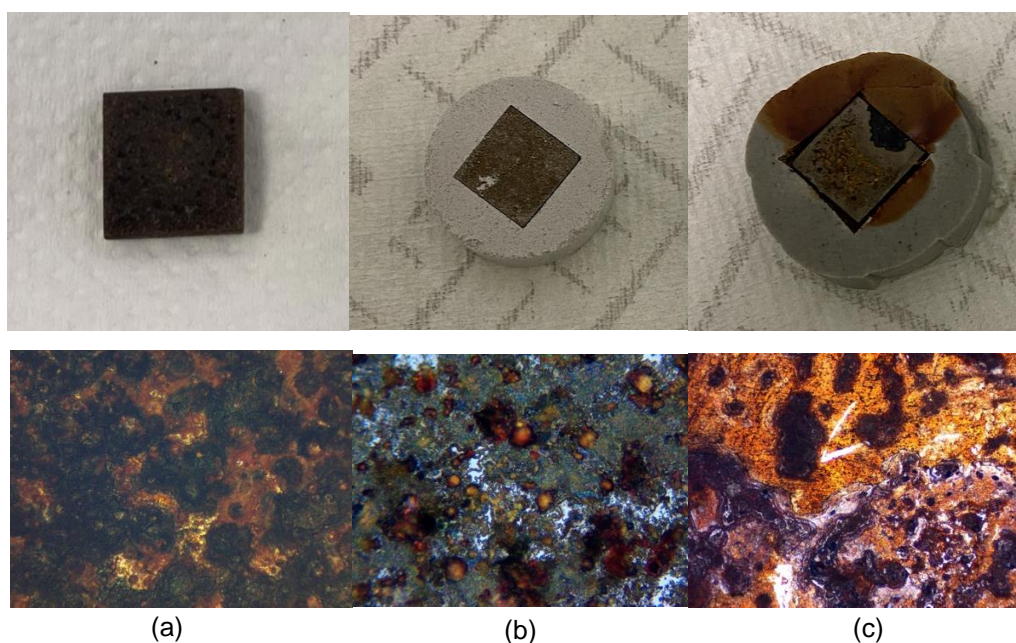


Figure 15 Visual inspection and microscope images of steel+bentonite samples (atmosphere face) after 42 days of irradiation (a)RH63% (F-31), (b) RH76% (F27), (c)RH99% (F29)

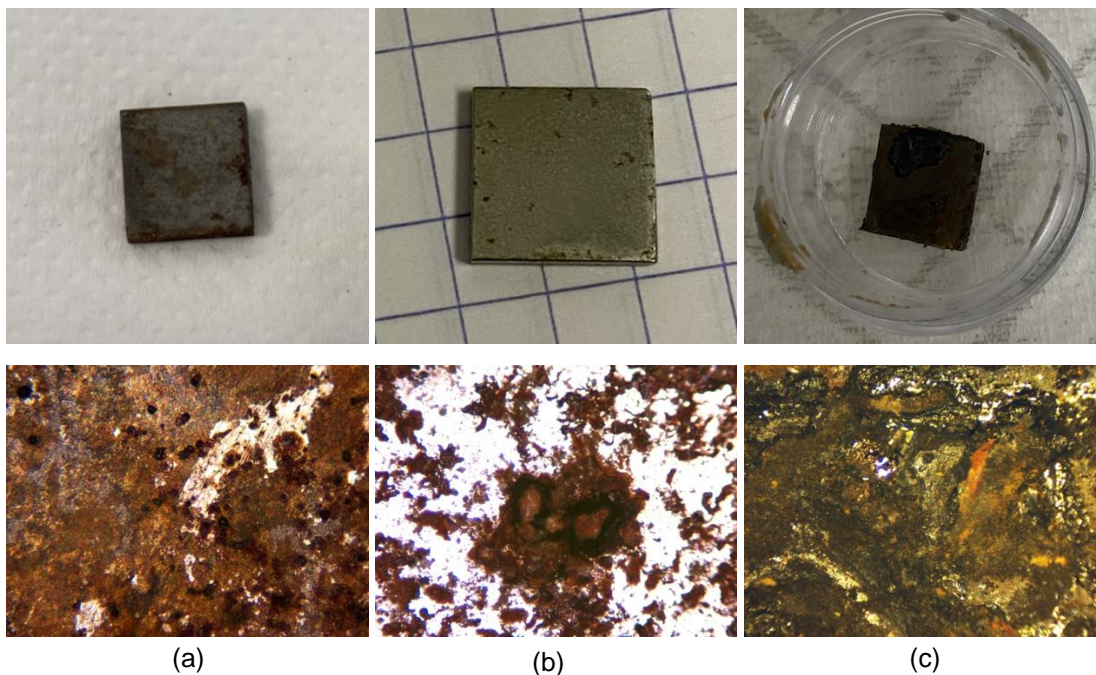


Figure 16 Visual inspection and microscope images of steel+bentonite samples (clay face) after 42 days of irradiation (a)RH63% (F-31), (b) RH76% (F28 with F27 microscope image), (c)RH99% (F29)

As can be seen from the figures above, the corrosion layer of the atmosphere face and the clay face is different. Atmosphere face shows more corrosion layer compared to the clay face for samples of RH63% and 76%, while it tends to be the opposite for 99%. We also observe that the corrosion layer in the RH99% sample (orange colour) would also be transported through the clay as can be seen in Figure 15c. We would also find similar results in the unirradiated samples shown in

Figure 17. It can also be seen in the figure that there is a formation of a water layer on the surface of the atmosphere face. This is true for both irradiated and unirradiated samples.

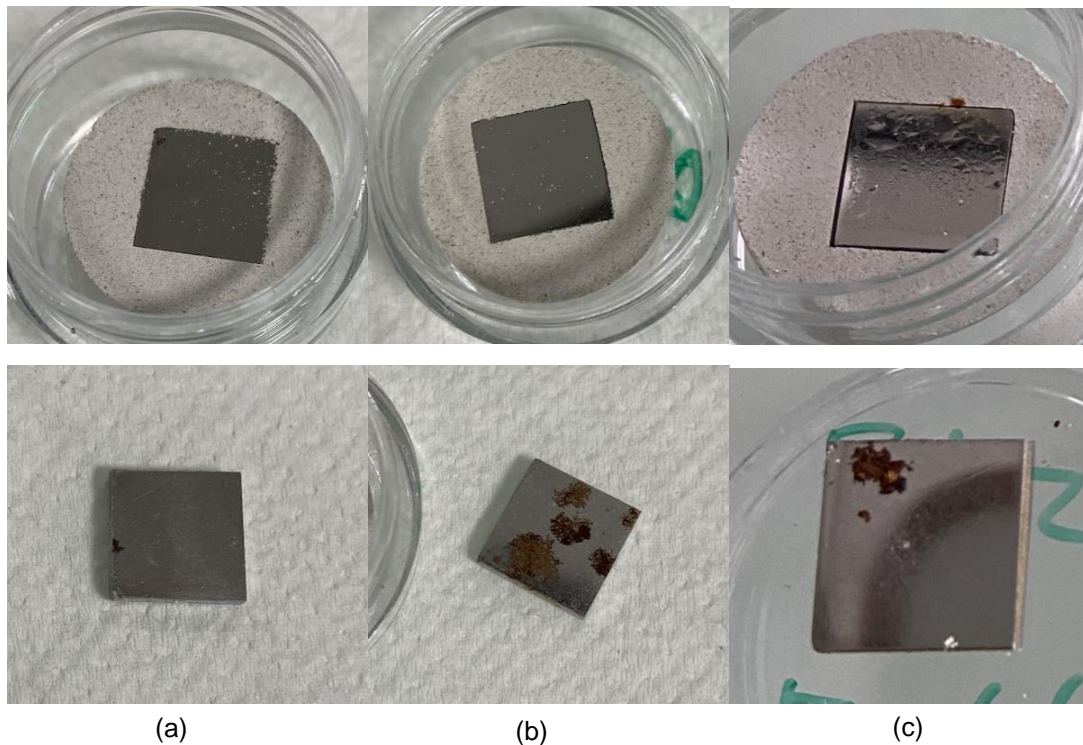


Figure 17 Visual inspection of steel+bentonite samples after 26 days of exposure (a)RH63% (F-69), (b) RH76% (F70), (c)RH99% (F66) (top: atmosphere face, bottom: bentonite face)



Figure 18 Corrosion layer transported in clay from unirradiated sample F25

Alongside the effect of relative humidity, the effect of irradiation time is also analysed. It has been found that with longer irradiation time, thicker corrosion layers are developed. This difference can be most significantly observed in the comparison between samples of 99% humidity that was irradiated for 10 days compared to 36 days (Figure 19). Samples with different relative humidity also show this tendency.

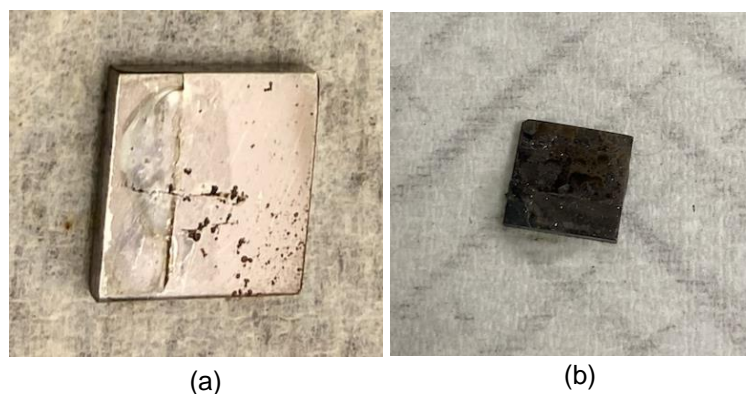


Figure 19 Visual inspection of 99% humidity samples with irradiation time of (a) 10 days and (b) 36 days.

Lastly, visual inspection is also done to the sample exposed to ambient humidity (about 50-60%). These samples developed very little to no corrosion layer as can be observed in Figure 20.

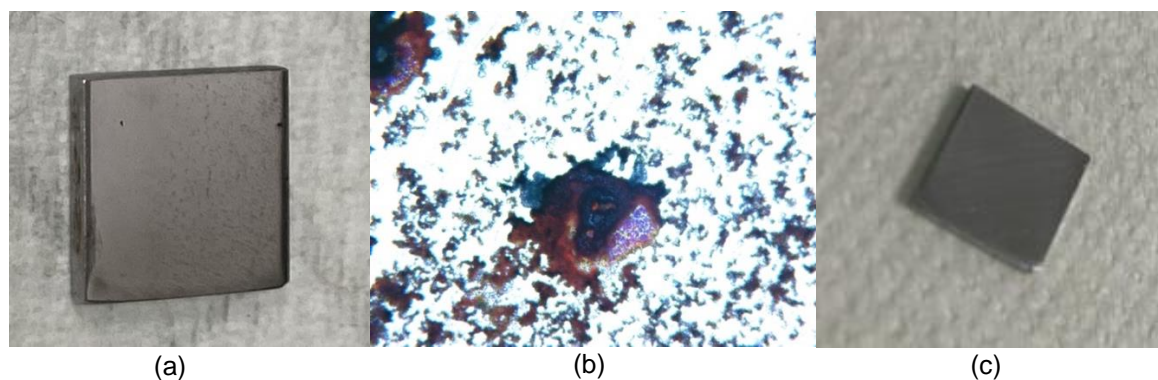


Figure 20 Steel only sample exposed to ambient humidity (a) F46 sample with (b) microscope image, (c) untreated sample.

1.8.3 Mass loss

Two types of experiments were conducted: (1) steel and (2) Steel + clay. All experiments were conducted under argon atmosphere. Reference samples (without irradiation) were prepared for the experiments using the steel. Table 3 shows experimental conditions and corrosion rates obtained for the experiments with the steel alone. The reference sample experiments (without irradiation) results are shown in Table 4. The results of reference samples hydrated at 63 and 99% RH for 26 days show only small corrosion rates of about 1 $\mu\text{m}/\text{year}$.

The results of the steel corrosion under irradiation are plotted in Figure 21. The first result to be highlighted is the very high corrosion rate obtained at the lowest RH (63%), which decreased from 427 $\mu\text{m}/\text{y}$ at 7d to 232 $\mu\text{m}/\text{y}$. For experiments at higher RH (76% and 99%) the corrosion rates are much lower but still decrease with time from 32 $\mu\text{m}/\text{y}$ (at 7d) to 16 $\mu\text{m}/\text{y}$ (39 d) for experiments at 76% and from 170 $\mu\text{m}/\text{y}$ to 10 $\mu\text{m}/\text{y}$ for experiments at 99%. The decrease of corrosion rate with time maybe due the formation of protective corrosion layer that slows down the diffusion of corroding species (i.e. water radiolysis products).

Experiments L19 and F46 (Ambient) were conducted without any RH control, meaning no addition of saline solution. In this case the headspace was flashed with argon and the containers were placed in the gamma irradiator for 7 and 10 days. Comparing the results of these experiments (samples L19 and F46) with their counterparts with controlled RH at 63% (samples F33 and F40) or RH at 70% (samples

F37 and F42), one can notice that the corrosion rate in the absence of saline solution (water) is lower than that in the experiments with controlled RH using saline aqueous solution, which can continuously provide water molecules in the head space.

Table 3 Corrosion experiments of steel coupons under different experimental conditions (RH, time, and dose).

Sample		Relative Humidity (%)	Target Total Dose (kGy)	Irradiation time (days)	Corrosion rate ($\mu\text{m}/\text{year}$)	Error of Corrosion Rate ($\mu\text{m}/\text{year}$)	Error in Percentage
L	19	Ambient	50	7	24.2	2.3	10%
F	46		100	10	23.2	2.3	10%
F	33	63	50	7	426.9	2.4	1%
F	40		100	10	290.9	4.0	1%
F	18		200	21	247.3	1.8	1%
F	23		400	39	232.5	0.5	0%
F	37	76	50	7	32.2	3.8	12%
F	42		100	10	35.0	3.8	11%
F	20		200	21	33.7	1.1	3%
F	72		400	39	16.2	0.6	4%
F	38	99	50	7	170.3	2.3	1%
F	45		100	10	14.1	2.3	16%
F	21		200	21	1.5	1.7	119%
F	74		400	36	10.6	0.7	6%

Table 4 Reference corrosion experiments of steel.

Sample		Temperature ($^{\circ}\text{C}$)	Relative Humidity (%)	Exposure period (days)	Corrosion rate ($\mu\text{m}/\text{year}$)	Error of Corrosion Rate ($\mu\text{m}/\text{year}$)	Error in Percentage
F	90	25	63	26	0	-	-
F	92	25	99	26	1.0159	0.8989	88%

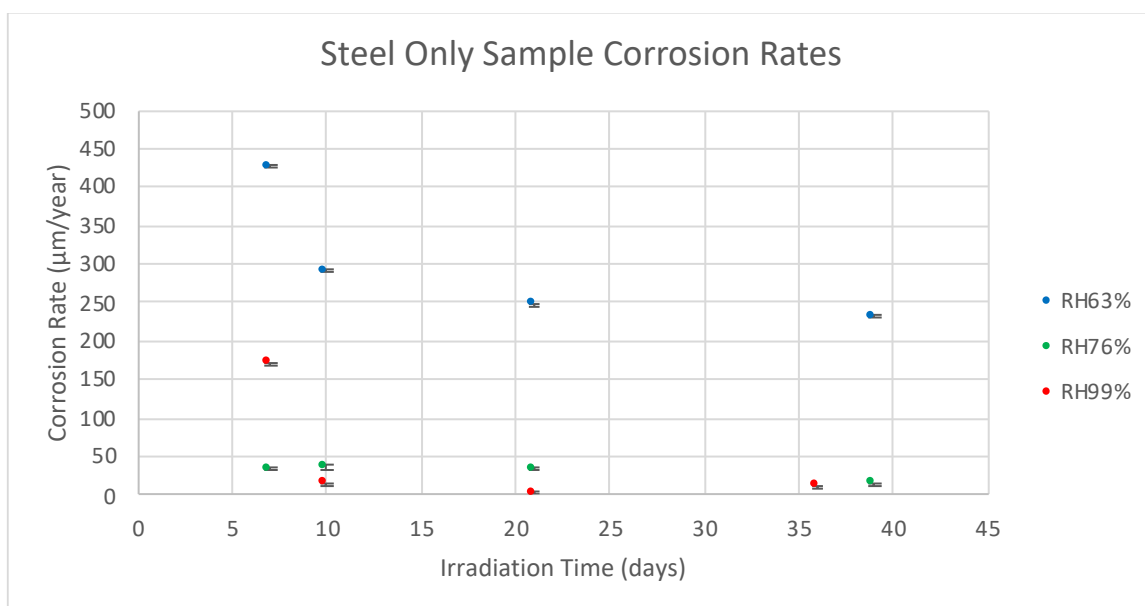


Figure 21 Corrosion rate of steel coupons hydrated at 25°C and different RH as a function of time. In the presence of radiation at a dose rate of 400 Gy/h

The results of steel corrosion in contact with bentonite as a function of RH and time (total dose) are given in Table 5. The experiments were conducted between 7 and 39 days at room temperature. The total dose was between 50 and 400 kGy. As with the experiments using steel alone, one can notice that the higher corrosion rate was encountered for experiments at the lowest RH of 63%. Also, the corrosion rate decreases with increasing time for all the experiments (Figure 22 and Figure 23). Figure 23 clearly shows that, as with the experiments using the steel alone, the corrosion rate at the lowest RH of 63% is very high compared to experiments at the highest RH (100%).

Table 5 Corrosion experiments of steel coupons in contact with bentonite under different experimental conditions (RH, time, and dose).

Sample		Relative Humidity (%)	Target Total Dose (kGy)	Irradiation time (days)	Corrosion rate (µm/year)	Error of Corrosion Rate (µm/year)	Error in Percentage
F	10	63	50	7	107.3	5.1	5%
F	1		100	12	129.0	3.1	2%
F	48		200	21.5	52.3	1.7	3%
F	31		400	39	29.5	0.9	3%
F	12	76	50	7	21.0	5.5	26%
F	58		100	14	59.0	2.7	5%
F	50		200	21.5	18.2	1.7	9%
F	27		400	39	6.4	0.9	8%
F	15	99	50	7	39.4	5.5	14%
F	60		100	14	58.0	2.7	11%
F	54		200	21.5	10.1	1.8	18%
F	29		400	39	28.0	1.0	2%
F	76	H2O (~100%)	200	21	2.6	1.7	67%

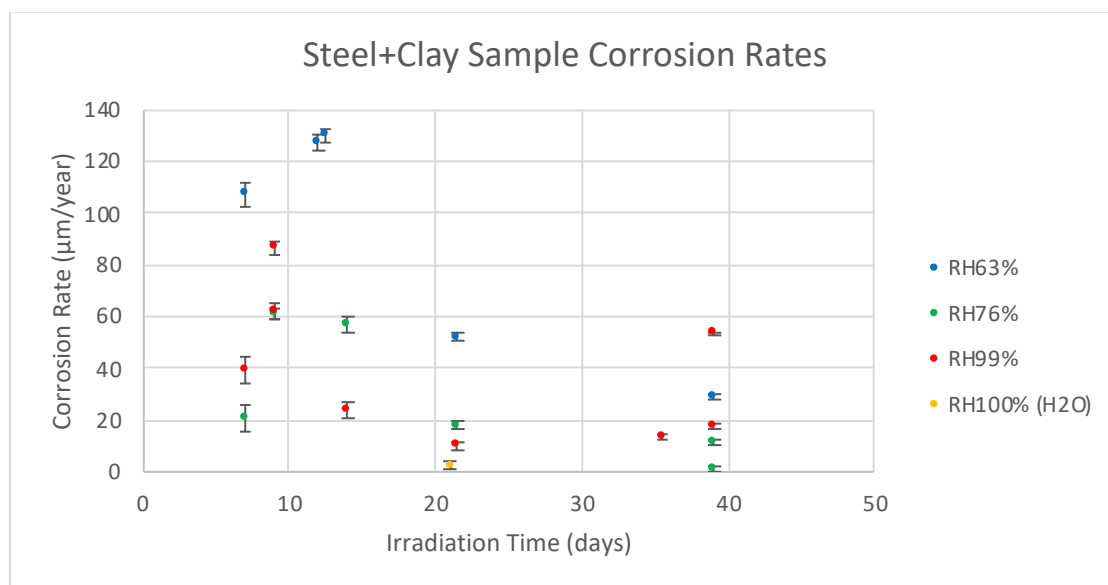


Figure 22 Corrosion rate of steel coupons in contact with bentonite hydrated at 25°C and different RH as a function of time.

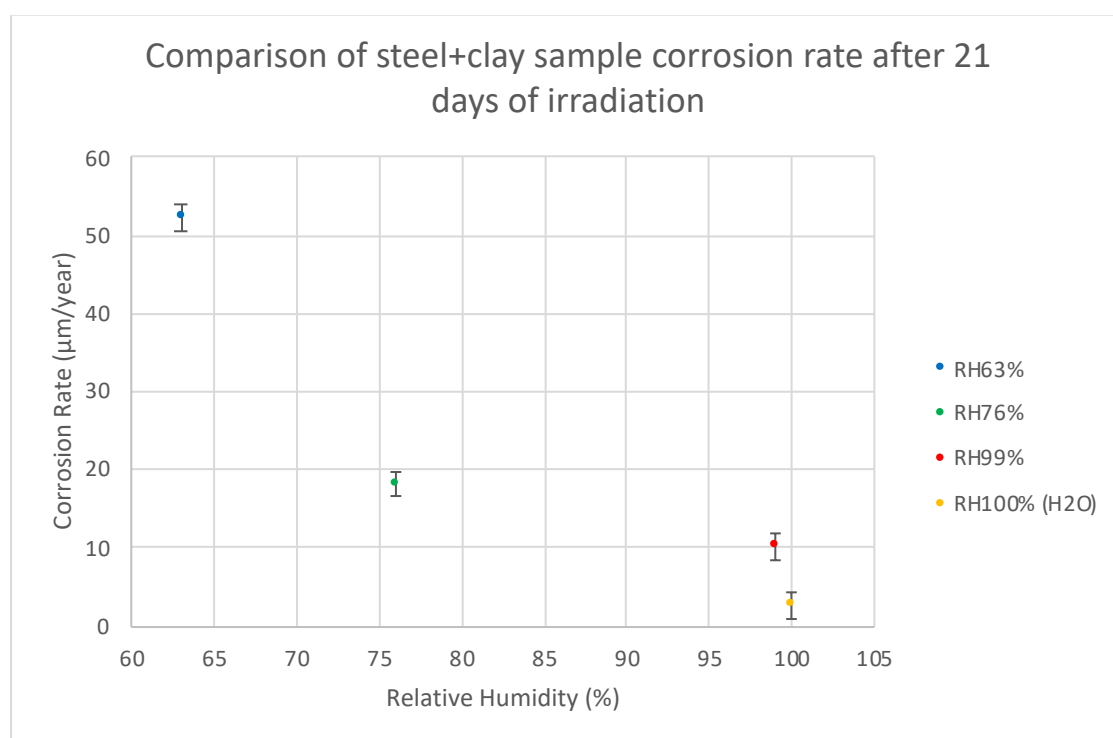


Figure 23 Corrosion rate of steel coupons in contact with bentonite hydrated at 25°C for 21 days and different RH.

1.8.4 Surface SEM-EDX

SEM cross-section of the corroded steel shows the formation of a thick corrosion layer (30-40 µm) for the steel corroded at 76% for 14 days reaching a total dose of 100 kGy (Figure 24). The EDX analysis revealed the presence of Fe, O and traces of Ca and Si (Figure 25) and sometimes Cl (Figure 26). Elements such as Si and Mn found could be detected as part of the P235GH steel composition, however Ca and Cl suggests the presence of phases such as Calcite and Akaganeite respectively.



Figure 24 SEM photo of steel hydrated at 76% RH (side facing the atmosphere) for 14 days in the experiment with bentonite (Sample F58).

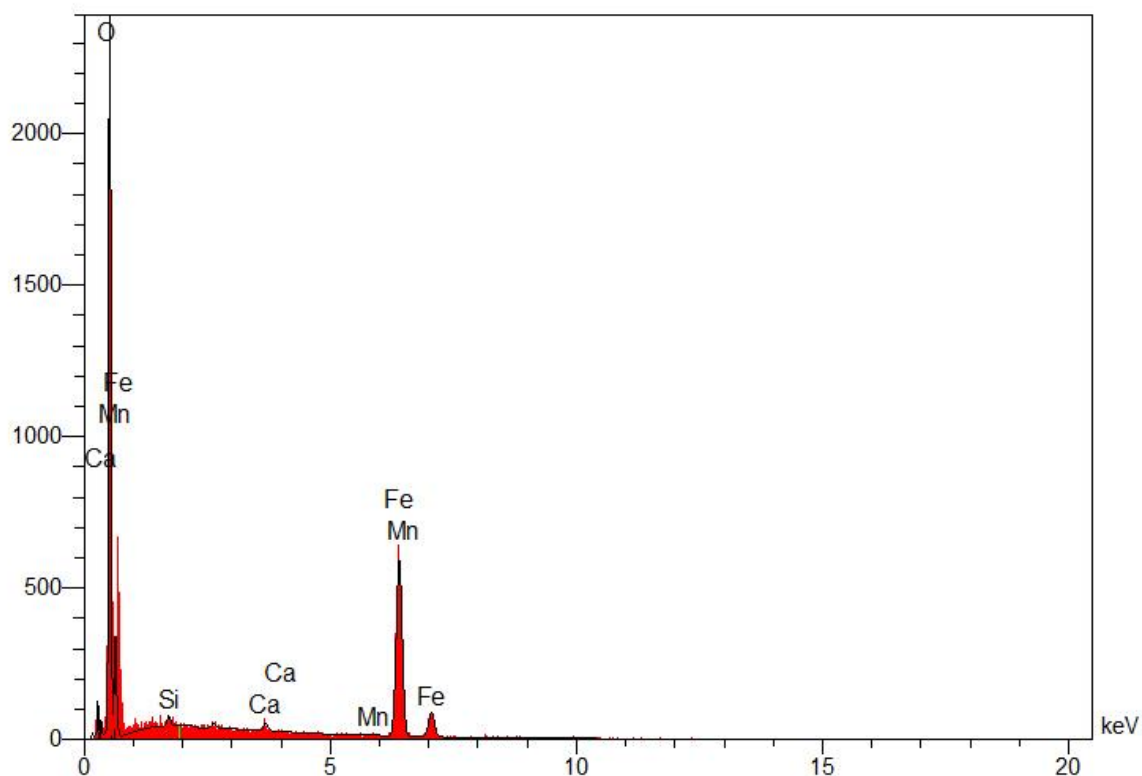


Figure 25 EDX spectrum of steel hydrated at 63% RH for 10 days showing the presence of Fe, O and traces of Si and Ca.

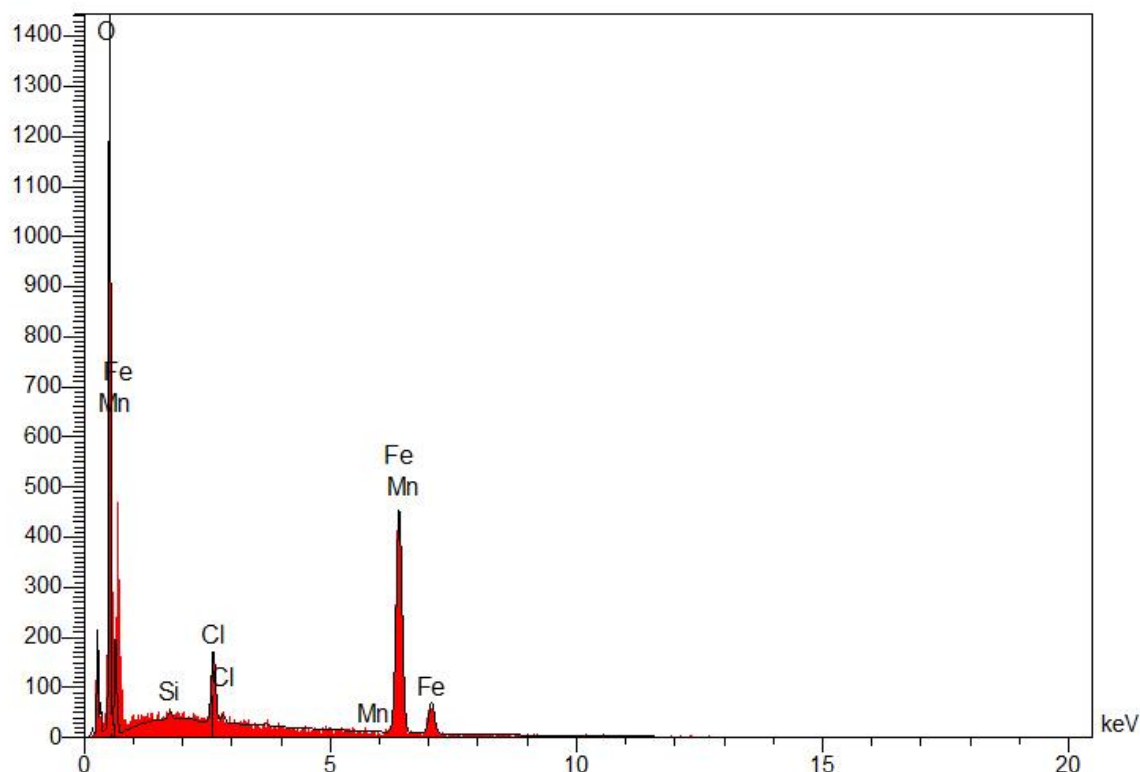


Figure 26 EDX spectrum of steel hydrated at 63% RH for 10 days showing the presence of Fe, O and Cl.

1.8.5 Surface XRD

The results of XRD studies for steel alone experiments are summarized in Table 6. The experiments conducted at ambient atmosphere without RH control did not show detectable phases. Regardless of the RH, the major corrosion products are magnetite (Fe_3O_4), siderite (FeCO_3), goethite (FeOOH), and akaganeite (beta $\text{Fe}^{3+}(\text{O},\text{OH},\text{Cl})$) and to a lesser extent chukanovite ($\text{Fe}_2(\text{CO}_3)(\text{OH})_2$), that has been only found at near saturation conditions (99%) together with hematite.

It is interesting to highlight the mixture between phases stable in reducing conditions (e.g. siderite, magnetite) and phases requiring oxidizing conditions (e.g. goethite, ferrihydrite). Given that the experiments are conducted in tight containers pre-flashed with Ar, one can reasonably suggest that oxidizing radiolysis products such as the $\text{OH}\cdot$ radical or H_2O_2 molecules may create localised oxidizing conditions at the interface water vapour / steel.

Table 6 Corrosion products formed in experiments with steel coupons under different experimental conditions (RH, time, and dose).

Sample	Relative Humidity (%)	Total Dose (kGy)	Phases	
			M: Major phase (> 5%) m: minor phase (< 5%) tr: trace (<1%)	
L	19	Ambient	50	Only iron detected
F	46	Ambient	100	Only iron detected

F	33	63	50	Siderite 12.9% (M), Goethite: 7.1% (M), Magnetite: 8.4% (M), Iron: 71.6% (M)
F	40	63	100	Akaganeite: 13.1% (M), Goethite: 19.1% (M), Fougerite: 10.8 (M), Magnetite: 12.9% (M), Siderite: 6.7% (M), Ferrihydrite: 24.8% (M), Fe _{0.8} Mn _{0.2} 4.6% (m), Iron: 8.1% (M)
F	18	63	200	Goethite: 12.6% (M), Siderite: 15.5% (M), SiC: 49.3% (M), Feroxyhyte: 16.2% (M), Iron: 6.4% (M)
F	23	63	400	Goethite: 14.1% (M), Siderite: 16.6% (M), Magnetite: 8.4% (M), SiC: 54% (M), Fe _{0.8} Mn _{0.2} : 5.2% (M), Iron: 1.7% (m)
F	37	76	50	Akaganeite: 5.7% (M), Goethite: 2.4% (m), Magnetite: 1.3% (m), Iron: 90.6% (M)
F	42	76	100	Goethite: 4.7% (m), Magnetite: 6.8% (M), Siderite: 8.1% (M), Iron: 80.3% (M)
F	20	76	200	Akaganeite: 17.4% (M), Calcite: 3.7 (m), Iron: 78.9% (M)
F	72	76	400	Goethite: 16.9% (M), Magnetite: 3.1% (m), Iron: 79.9% (M)
F	38	99	50	Not detected any phases
F	45	99	100	Akaganeite: 1.5% (m), Siderite: 1.1% (m), Iron: 97.4%
F	21	99	200	Goethite: 1.6% (m), Hematite: 0.4 (tr), Iron: 97.9% (M)
F	74	99	400	Chukanovite: 6.8% (M), Magnetite: 1.3% (m), Siderite: 0.9% (tr), Goethite: 2.1% (m), Iron: 88.9% (M)

The results of XRD studies for steel in contact with bentonite experiments are summarized in Table 7. It seems that the presence of bentonite has led to the formation of a variety of phases that were not detected in experiments with the steel alone. Still the major phases are magnetite, siderite, goethite and akaganeite. The presence of calcite and montmorillonite may be initially present in bentonite.

The experiments conducted at ambient atmosphere without RH control did show detectable phases. Regardless of the RH, the major corrosion products are magnetite (Fe₃O₄), siderite (FeCO₃), goethite (FeOOH), and akaganeite (beta Fe³⁺ (O,OH,Cl)) and to a lesser extent chukanovite (Fe₂(CO₃)(OH)₂), that has been only found at near saturation conditions (99%) together with hematite.

Table 7 Corrosion products formed in experiments with steel coupons in contact with bentonite under different experimental conditions (RH, time, and dose).

Sample	Relative Humidity (%)	Total Dose (kGy)	Phases	
			M: Major phase (> 5%) m: minor phase (< 5%) tr: trace (<1%) Atm: atmospheric side Clay: side in contact with bentonite	
F	10	63	50	Atm: Magnetite: 4.8% (m), Siderite: 3.0% (m), Calcite: 23.1% (M), Xifengite?: 2.2% (m), Iron: 66.9% (M) Clay: Magnetite: 0.5% (tr), Calcite: 0.4% (tr), Montmorillonite: 1.3% (m), Iron: 97.7% (M)

EURAD Deliverable 15.8 – Synthesis of irradiation results under repository conditions

F	1	63	100	<p>Atm: Goethite: 12.3% (M), Siderite: 11% (M), Magnetite: 7.2% (M)</p> <p>Clay: Goethite: 1.2% (m), Magnetite: 0.4% (tr), Calcite: 0.6% (tr), Montmorillonite: 1.8% (m), knife: 29.2% (M), Iron: 66.9% (M)</p>
F	56	63	100	<p>Atm: Siderite: 5.8% (M), Magnetite: 5.4% (M), Xifengite?: 5.6% (M), Lepidocrocite: 5.1% (M), SiC: 34.3% (M), Ringwoodite?: 6.2% (M), Iron: 37.5% (M)</p> <p>Clay: Magnetite: 1.1% (m), Montmorillonite: 2.7% (m), Magnesium Calcite: 31% (M), Iron: 65.2% (M)</p>
F	48	63	200	<p>Atm: Magnetite: 1.4% (m), Iron: 98.6% (M)</p> <p>Clay: Magnetite: 1.2% (m), Magnesium Calcite: 6.2% (M), Montmorillonite: 2.2% (m), Fe0.5Mg1.5O5: 2.3% (m), Iron: 88.1% (M)</p>
F	31	63	400	<p>Atm: Calcite: 7.2% (M), Goethite: 16% (M), Siderite: 34.8% (M), Akaganeite: 13.7% (M), Xifengite?: 4.5% (m), Iron: 23.8% (M)</p> <p>Clay: Calcite: 2.4% (m), Iron: 97.6%</p>
F	12	76	50	<p>Atm: Magnetite: 0.7% (tr), Akaganeite: 2.3% (m), Magnesium Calcite: 4.7% (m), Iron: 92.3% (M)</p> <p>Clay: Almost nothing detected, Magnetite: 0.4% (tr), Iron: 99.6% (M)</p>
F	4	76	100	<p>Clay: Magnetite: 0.5% (tr), Calcite: 1.9% (m), Iron: 97.6% (M)</p>
F	58	76	100	<p>Atm: Siderite: 8.6% (M), Magnesium Calcite: 30.2% (M), Akaganeite: 8.7% (M), Montmorillonite: 1.4% (m), Iron: 51.1% (M)</p> <p>Clay: Akaganeite: 6.8% (M), Calcite: 1.5% (m), Magnetite: 1.4% (m), Akermanite: 9.2% (M), Pigeonite: 3.6% (m), Siderite: 2.8% (m), Iron: 74.8% (M)</p>
F	50	76	200	<p>Atm: Goethite: 3.3% (m), Calcite: 11.1% (M), Akaganeite: 6.2% (M), Magnetite: 1.5% (m), Siderite: 0.8% (tr), Cronstedtite: 3.2% (m) Iron: 73.9% (M)</p> <p>Clay: Siderite: 3.7% (m), Akaganeite: 6.7% (M), Calcite: 0.9% (tr), Montmorillonite: 2.1% (m), Iron: 86.5% (M)</p>
F	27	76	400	<p>Atm: Goethite: 5.4%, Calcite: 1.4% (m), Iron: 93.2% (M)</p> <p>Clay: Siderite: 2.2% (m), Goethite: 0.8% (tr), Akaganeite: 2% (m), Magnesium Calcite: 3.2% (m), Montmorillonite: 2% (m), Iron: 89.8% (M)</p>
F	28	76	400	<p>Atm: Goethite: 6.6% (M), Iron: 93.4%</p> <p>Clay: Nothing detected, unidentified peak at 31.518 (very small)</p>
F	15	99	50	<p>Atm: Goethite: 2% (m), Iron: 98% (M)</p> <p>Clay: Goethite: 1.1% (m), Calcite: 1.6% (m), Montmorillonite: 1.1% (m), Iron: 95.1% (M)</p>
F	8	99	100	<p>Clay: Goethite: 3.2% (m), Calcite: 1.3% (m), Montmorillonite: 1.4% (m), Iron: 94.1%</p>
F	9	99	100	<p>Clay: Goethite: 7.6% (M), Calcite: 2.1% (m), Montmorillonite: 1.7% (m), Iron: 88.7% (M)</p>
F	60	99	100	<p>Atm: Goethite: 1.3% (m), Akaganeite: 3.1% (m), Lepidocrocite: 0.6% (tr), Montmorillonite: 3.1% (m), Calcite: 1.7% (m), Linzhiite?: 0.9% (tr), Chukanovite: 3.6% (m), Iron: 85.8% (M)</p> <p>Clay: Siderite: 5.2% (M), Akaganeite: 3.7% (m), Goethite: 1.1% (m), Magnesium Calcite: 1.6% (m), Lepidocrocite: 1% (tr), Chukanovite: 3.6% (m), Linzhiite?: 0.8% (tr), Iron: 78.2% (M)</p>
F	54	99	200	<p>Atm: Siderite: 1.6% (m), Hematite: 0.5% (tr), Ulvospinel: 0.8% (tr), Linzhiite: 0.5% (tr), Iron: 96.7% (M)</p> <p>Clay: Magnesium Calcite: 3.4% (m), Siderite: 11.4% (M), Lepidocrocite: 0.6% (tr), Goethite: 0.8% (tr), Chukanovite: 3.6% (m), Linzhiite?: 1% (m), Iron: 72.1% (M)</p>

F	52	99	400	<p>Atm: Goethite: 1.1%, Siderite: 6.5% (M), Lepidocrocite: 1.4% (m), Chukanovite: 8.6% (M), Magnetite: 0.5% (tr), Magnesium Calcite: 2.1% (m), Iron: 79.8% (M)</p> <p>Clay: Siderite: 14.5% (M), Linzhiite: 1.2% (m), Calcite: 5.3% (M), Magnetite: 1.0% (tr), Lepidocrocite: 1.5% (m), Akaganeite: 3.3% (m), Iron: 73.2% (M)</p>
F	30	99	400	<p>Atm: Siderite: 10.7% (M), Goethite: 5.0% (M), Lepidocrocite: 2% (m), Magnetite: 2.8% (m), Iron: 79.4%</p> <p>Clay: Siderite: 11.1% (M), Goethite: 4.5% (m), Calcite: 4.3% (m), Iron: 80.1% (M)</p>
F	29	99	400	<p>Atm: Goethite: 1.5% (m), Calcite: 5.8% (M), Iron: 92.7%</p> <p>Clay: Magnetite: 1.1% (m), Calcite: 6.2% (M), Siderite: 6.5% (M), Montmorillonite: 2.8% (m), Quartz: 2.2% (m), Iron: 81.2% (M)</p>
F	76	H2O (~100%)	200	<p>Atm: Siderite: 2.4% (m), Montmorillonite: 1.4% (m), Ferrihydrite: 1.1% (m), Linzhiite: 0.8% (tr), Birnessite: 0.8% (tr), Iron: 93.4% (M)</p> <p>Clay: Calcite: 3% (m), Siderite: 1.4% (m), Goethite: 0.6% (tr), C6Co0.7Fe0.3KN6Ni: 1.0% (tr), Montmorillonite: 2% (m), Iron: 92.1% (M)</p>

1.9 Discussion

The water radiolysis scheme can be seen in Figure 27, showing the different steps leading to the formation of water radiolysis products. Among them oxidizing species such as OH^{*} radicals or H₂O₂ molecules that can lead to iron oxidation to Fe²⁺ and further to Fe³⁺ species. Hence, even under de-aerated conditions Fe³⁺-based corrosion products (e.g. goethite) were frequently identified on the steel corroded at 63%, 76% and 99% RH.

An important result to highlight is that the highest corrosion rate was obtained at the lowest RH of 63%. This can be explained by the enhanced release of H₂ from the very thin layer of water at the steel (solid) interface, about 2-3 layers of H₂O as indicated by Ebert et al. (1991). Hydrogen fast release inhibits the reaction of its recombination with OH^{*} radicals as shown in the following equation:



The inhibition of the reaction consuming HO^{*} radicals (see equation above) keeps them available for interaction with the steel surface and the formation of magnetite Fe₃O₄ (containing Fe²⁺), and ultimately goethite FeOOH (containing Fe³⁺). This hypothesis is supported by the results of H₂ production as a function of RH (Figure 13). In fact, the highest production rate of H₂ was observed in the experiments with the highest corrosion rate at the lowest humidity 63% (more H₂ escaped from the few water layers in contact with the steel to the headspace), and decreased with increasing RH from 63% to 76% and then to 99%, corresponding to lower corrosion rates.

This finding merits further analysis particularly in the situation of deep geological repositories where unsaturated conditions are expected to last for thousands of years prior to complete saturation of the site.

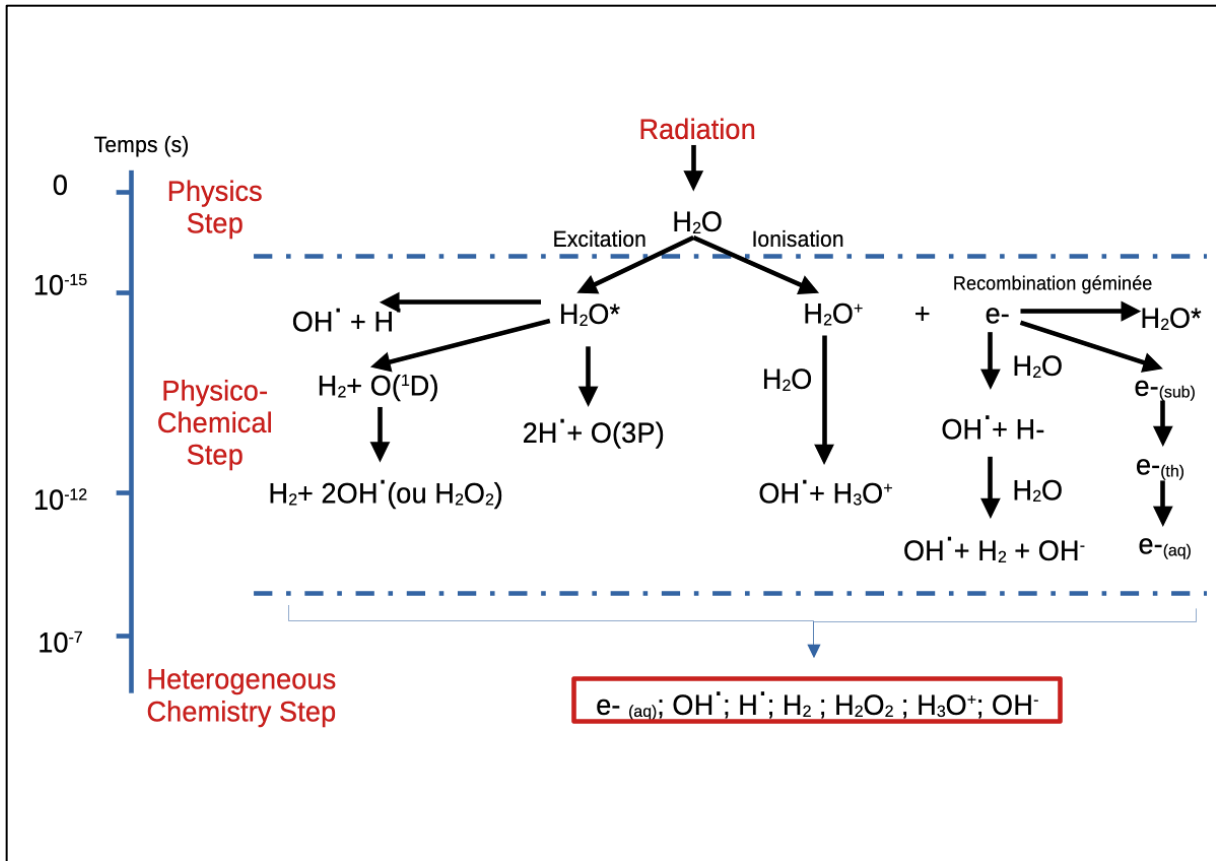


Figure 27 Schematic of the reaction mechanisms and approximate time scales for production of various species during water radiolysis [Robira, 2018]

2. Experiments performed by UJV

2.1 Overview

The degree of corrosion was investigated in respect to different dose rates, temperature, and saturation. Experimental design consisted of bentonite with embedded carbon steel samples compacted and saturated in modules, inserted in sealed chambers (mounted in anaerobic box), irradiated (^{60}Co source) and constantly heated at 150 °C for 6, 9, 12 and 18 months.

The dose rate (0.4 Gy h^{-1}) was calculated simulating conditions, close to the fuel assembly at the define temperature (Pospíšková et al. 2017). Modules were closed, keeping anaerobic conditions inside. The reference non-irradiated modules were allocated in the anaerobic box under corresponding temperature to compare irradiated and non-irradiated systems.

Complementary modules were designed used for an estimation of microbial survivability after exposure at given conditions (EURAD CONCORD Task 4).

2.2 Test specimens

2.2.1 Carbon steel samples

The discs (10 mm in diameter, 1 mm thick) composed of carbon steel S355J2H (supplied by Škoda, Figure 28) were obtained by cutting a tube, which serves as the outer casing for the Czech canister concept (Pospíšková et al. 2017). The steel discs were prepared out of the weld by crosscutting and grinding using grinding wheel with 46K grit.



Figure 28 Left – carbon steel disks, right – outer case of the canister in the Czech concept.

2.2.2 Bentonite samples

Two types of bentonite were used in the corrosion experiment: a calcium-magnesium bentonite (BCV) from the Czech Republic (provided by KERAMOST, Plc., Czech Republic) and a sodium bentonite (MX-80) that served as a reference material (provided by CIEMAT).

2.2.3 Saturation solution

A synthetic granitic water (SGW3, Table 8) was used as a saturation medium in all experiments designed by UJV. Chemical composition of SGW3 was calculated representing waters typical for the Rožná mine formation (the Bohemian Massif) layers located 1000-1200 m below the surface (Červinka et al. 2018).

Table 8 Chemical composition of synthetic granitic water (Červinka et al. 2018).

c (mg/l)	Na ⁺	K ⁺	Ca ²⁺	Mg ²⁺	F ⁻	Cl ⁻	NO ₃ ⁻	SO ₄ ²⁻	HCO ₃ ⁻
SGW3	89.4	0.7	1.3	0.1	9.9	18.7	-	10.5	163.5

2.3 Experimental design, irradiation and loading conditions

The experiment consisted of 23 cells – each containing compacted bentonite with embedded steel coupons (Figure 29). According to the DGR concept (Pospiskova et al. 2017) initial bentonite moisture content was adjusted to 15 % (cells heated up at 150 °C) and 20 % (cells heated up at 90 °C). The dry density of compacted bentonite was 1600 kg/m³. In each corrosion cell, there are 12 carbon steel samples that are divided into three layers, each layer containing four steel samples. The cells were compacted at hydraulic press machine MEGA 11-300 DM1S (Form+Test Seidner+Co GmbH, Germany). The cells were compacted under aerobic conditions simulating the initial stage of the repository.

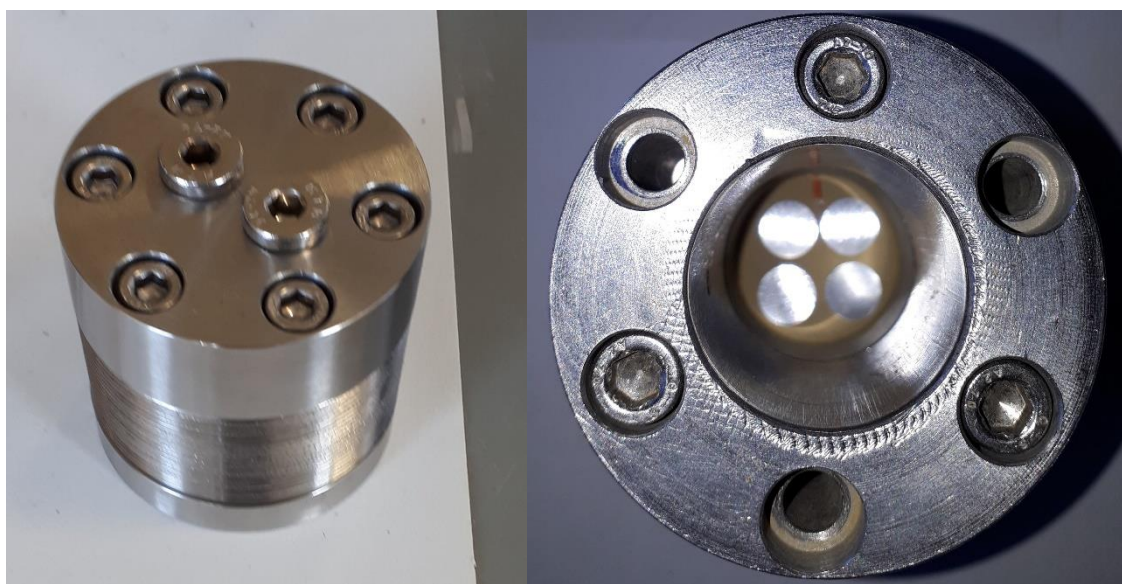


Figure 29 Left – corrosion cell, right – carbon steel samples inside of the corrosion cell.

The cells were connected to capillaries and saturated under the pressure of 5 MPa for the whole loading period (Figure 30). The saturation pressure was applied through pressure exchanger in which a piston is pressurized by Ar. The water was de-oxidized in the glove box (GP CONCEPT, Jacomex, France) prior to its usage. All experimental cells were loaded in Ar atmosphere in the glove box or in the steel vessels filled by Ar prior to their welding. Nine cells were subjected to ⁶⁰Co irradiation (dose rate at samples ~ 0.4 Gy.h⁻¹, Figure 30). Nine cells were heated up without irradiation. The heating was adjusted to the appropriate temperatures (87-90 °C, 146-150 °C). The rest of the cells was saturated under Ar atmosphere in the glove box (reference cells) at ambient temperature (~ 21 °C). The complete list of experimental cells and loading conditions are summarised in Table 9.



Figure 30 Left – steel vessels containing steel cells connected by metal capillaries with saturation medium situated in the irradiation area, right - steel cell containing compacted BCV bentonite and carbon steel coupons during disassembly (cell no. 22).

Table 9 A list of experimental cells and loading conditions.

Cell No.	Bentonite	w initial (%)	w final (%)	Loading period (months)	T (°C)	Radiation (Gy.h ⁻¹)	Dismantling
1	BCV	15	21.14	6	150	0.4	2022-11-01
2	BCV	15	21.28	6	150	-	2022-11-01
3	BCV	15	25.06	9	150	0.4	2023-01-31
4	BCV	15	21.96	9	150	-	2023-01-31
5	BCV	15	20.54	12	150	0.4	2023-05-04
6	BCV	15	9.29	12	150	-	2023-05-04
7	BCV	15	22.61	18	150	0.4	2023-11-07
8	BCV	15	22.33	18	150	-	2023-11-07
9	MX80	15	16.57	18	150	0.4	2023-11-07
10	MX80	15	20.00	18	150	-	2023-11-07
11	MX80	15	19.58	18	RT	-	2023-11-07
12	BCV	20	20.86	9	90	0.4	2023-01-31
13	BCV	20	24.55	9	90	-	2023-01-31
14	BCV	20	23.24	12	90	0.4	2023-05-04
15	BCV	20	23.93	12	90	-	2023-05-04
16	BCV	20	18.34	18	90	0.4	2023-11-07

17	BCV	20	21.78	18	90	-	2023-11-07
18	MX80	20	20.57	18	90	0.4	2023-11-07
19	MX80	20	20.42	18	90	-	2023-11-07
20	BCV	20	22.58	6	RT	-	2022-11-01
21	BCV	20	24.54	9	RT	-	2023-01-31
22	BCV	20	23.77	12	RT	-	2023-05-04
23	BCV	20	23.94	18	RT	-	2023-11-07

2.4 Disassembly

The heating of heated cells was stopped 1 day prior to disassembly due to the safety reasons. The saturation and irradiation were stopped at the same time. After cooling the steel vessels were opened. The cells were disassembled in the glove box under Ar atmosphere (Figure 30). Three types of loaded material were obtained: steel specimens, bentonite for geochemical and mineralogical analyses, bentonite for microbiological analyses (Concord Task 4, ConCorD Deliverable 15.9).

2.5 Post-test analysis

2.5.1 Post-test analysis of steel

Mass loss

Steel samples were subjected to decontamination according to the standard. A solution of hydrochloric acid inhibited by urotropine was applied. The standard prescribes gradual immersion of steel samples in the solution for 10 minutes. After each immersion, the samples were washed with demineralised water and ethanol and dried. Immersion and washing were repeated twice. Immediately after decontamination the steel samples were weighed using Precisa 240A analytical balances (Precisa Gravimetrics AG, Switzerland) with the 0.1 mg resolution, the same as before exposure. The weighing was done in triplicate. The corrosion rate was calculated as a mass loss divided by exposure time and surface area of the steel samples and multiplied by the steel density ($7.85 \text{ g}\cdot\text{cm}^{-3}$, ČSN EN 10210-1).

2.5.1.1 Visual inspections

The surface of the steel samples was documented using an Olympus SZX10 stereomicroscope (Olympus Corporation, Japan). Images of both sides of the samples were taken.

2.5.1.2 XRD

Corrosion products on metal samples were determined by X-ray diffraction analysis with the PANalytical XPertPRO MPD (PANalytical, B. V., Almelo, Netherlands). The following measurement conditions were used: CoK α radiation (voltage 40 kV, current 30 mA), fast linear detector PIXCel 3D and reflective Bragg-Brentano arrangement. In the primary beam, we used an integrated iCore module with a Bragg-Brentano HD mirror, a 6 mm mask, a 0.03 rad Soller diaphragm, and a 0.25° divergence diaphragm. In the diffracted beam, we used an integrated dCore module with 0.25° anti-dispersion diaphragm and 0.02 rad Soller diaphragm. The measurement range was 4 to 80° 2theta with a step of 0.0131°.

Raman spectroscopy

Micro-Raman spectra of samples were measured by dispersive Raman spectrometer (Nicolet model DXR2-Raman microscopy, Thermo Electron Scientific Instruments LLC, USA) equipped with confocal microscope Olympus. As an excitation source, a laser having wavelength 532 nm and input power maximum 10mW was used. Full range grating (spectral range 3500 – 50 cm⁻¹), 25 µm confocal pinhole apertures and CCD detector (a multi-channel cooled CCD camera) were used. Samples were measured with following parameters: laser power: 0,5 mW - 2 mW, aperture 25 pinhole, objective L50x, collect exposure time: 2 s, sample exposures 200, background exposure 200. All recorded spectra were analyzed after fluorescence correction or baseline correction using OMNIC software (Thermo Electron Scientific Instruments LLC, USA).

2.5.1.3 SEM-EDX in cross-section

Microscopical analysis of corroded steel samples was conducted on stereomicroscope Nikon SMZ 745, light microscope Nikon Eclipse MA200 (Nikon Metrology, Ins.) and scanning electron microscope TESCAN AMBER (Tescan Group, a.s.) combined with energy dispersive spectrometer Oxford UltimMax 100 (SEM-EDS, Oxford Instruments plc.). Prior to the SEM-EDS analysis the steel surface was coated with carbon.

2.5.1.4 Profilometry

The profilometry was conducted employing 4-axes optical profilometer RedLux (RedLux Ltd., Southampton, UK). Laboratory of optical profilometry consisting of two sliding and two rotary axes. The rotary axes move with the sample and the shift axes move with the sensor. All axes use optical position sensors and linear motors. The sensor is a point confocal sensor. The principle of the analysis is based on the colour aberration of the lens (chromatic aberration) and is used to measure the distance from the measured object very accurately. According to the manufacturer's values, linear axes have a resolution of 100 nm, rotary axes 10" (arcsecond). The resolution of the point confocal sensor stated by the manufacturer is 20 nm. A profilometer records the position of individual points on a surface with a certain frequency. The frequency of point scanning can be set in both circumferential and longitudinal directions. The data were evaluated using the Matlab software (MathWorks, Inc.).

2.5.2 Post-test analysis of bentonite

2.5.2.1 Chemical composition

The chemical composition of bentonite was determined by X-ray fluorescence analysis (XRF). The spectrometer ARL 9400 (Thermo Fisher Scientific Inc.). The XRF method was chosen because of the small amount of sample needed to be analysed. The XRF analysis included the determination of the loss on ignition (LOI) at 850 °C. The total carbon content (C_{tot}) and the total sulphur content (S_{tot}) were determined spectrophotometrically using the ELTRA CS 580 analyser (ELTRA GmbH, Germany) from a naturally wet sample.

2.5.2.2 XRD

X-ray powder diffraction patterns of bentonite samples were measured on the Empyrean, series III instrument, the same as corrosion products on steel samples (Section 2.5.1.1). For the bentonite samples, the loading time was 600 sec/step. This represented an analysis of about 4 hours. The samples were adjusted for measurement in back-loading cuvettes. The measured diffractograms were evaluated using HighScorePlus, version 5.1.0b, Malvern PANalytical b.v., Almelo, NL (Degen et al. 2014) by comparison with database data contained in the PDF-4+ database (PDF-4+ database 2023). Estimates of mass fractions (QPA) of individual crystalline phases were performed using the Rietveld method (Rietveld et al. 1969) using Profex 4.3.6 / BGMN 4.2.23 (Bergmann et al. 1998, 2001; Döbelin and Kleeberg 2015). We used models obtained from ICSD (ICSD database 2022) and PDF-4+ (PDF-4+ database 2023). We used a structural model from BGMN (Bergmann et al. 1998).

2.5.2.3 Water leachates

The determination of leachable ions was performed by a series of batch experiments in different ratios of solid and liquid phase (s:l) into MilliQ water. The phase ratio (s:l) used in the interpretation indicates the ratio of dried bentonite to water. The samples were dried at 105 °C prior to the leaching. The phase interaction time (14 days) is considered long enough to achieve solid/liquid equilibrium (Roy et al. 1993; Hofmanová et al. 2019). Subsequently, the liquid phase was separated by centrifugation, filtered through a 0.20 µm membrane filter (Millipore®). The main cations (Na⁺, K⁺, Mg²⁺, Ca²⁺, Fe^{x+}) and anions (Cl⁻, F⁻, SO₄²⁻, NO₂⁻, NO₃⁻, HCO₃⁻) were analysed in all solutions. Anions were analysed employing capillary zone electrophoresis CE 7100 (Agilent Technologies, Santa Clara, USA) with UV detection. Cations were analysed employing double beam flame atomic absorption spectrophotometer SavantAA Σ (GBC Scientific Equipment Pty Ltd, Australia). The content of carbon dioxide forms (species) was analysed based on alkalimetric titration following the standard procedure ČSN 75 7373 (2001).

2.5.2.4 Cation exchange capacity

The CEC and exchangeable cations were determined by the Cu(II)-triethylenetetramine (Cu-trien) method (Meier and Kahr 1999; Ammann et al. 2005). Cu-trien (0.01 mol/L) was mixed with dried (105 °C) samples in the solid-to-liquid ratio of 25 g/L. After interaction for 30 minutes, the suspensions were centrifuged, and supernatants were analysed. The Cu²⁺ concentration was determined by UV/Vis spectrophotometer Specord 205 (Ana-lytik Jena, DEU). The concentration of displaced cations (Na⁺, K⁺, Ca²⁺, Mg²⁺) was determined by atomic absorption spectrometer SavantAA (GBC Scientific Equipment, AUS). Two values of cation exchange capacity were derived: CEC_{Vis} from copper depletion and CEC_{SUM} by summing equivalent concentrations of displaced cations.

2.5.2.5 Scanning electron microscopy

The samples were studied using a JEOL SEM JSM 6510LV scanning electron microscope (JEOL, Ltd.) with an attached Oxford Instruments INCAx-actSN 55847 EDS analyser (Oxford Instruments plc.) operating at a resolution of 133 eV measured at 5.9 keV. The SEM microscope is equipped with a tungsten cathode, which allows work in the "low vacuum" mode. Due to the fact, that the studied materials were prepared from electrically non-conductive material and contained weakly bound water, the measurement was carried out in the "low vacuum" mode at an air pressure of 50 Pa. Under these conditions, there was neither charging of the surface of the samples by the action of the electron beam nor problems with achieving the necessary vacuum. The EDS analysis was carried out using a semi-quantitative method without standards using the company's software. Both microscopic images and EDS analyses were taken at an accelerating voltage of 25 kV.

2.6 Results of tests performed by UJV

2.6.1 Mass loss

The steel samples were embedded in bentonite in three layers in each cell. All experiments aimed to fully homogeneous saturation of experimental cells within the experiment. Thus, corrosion rate is expected to be comparable in all steel specimens in the cell under these conditions. Fully saturated cells exhibit very low confidence intervals (e.g., 0.1 µm y⁻¹) of corrosion rate indicating homogeneous saturation of the cell within the experiment. The cells no. 2, 3, 13, 15 and 17 indicate higher corrosion rate of the steel samples located in two layers close to the source of saturation medium. The steel samples located in the third outermost layer in the cell indicated lower corrosion rate. This heterogeneity in the individual layers is explained by inhomogeneous saturation of the cell. Lower water content decreased a corrosion rate of the steel samples. The inhomogeneity of the saturation is reflected by higher confidence intervals of corrosion rate (2.1–4.1 µm y⁻¹) (Table 10).

The corrosion rates indicated small variation of corrosion rate in the steel samples embedded at BCV bentonite heated up at 150 °C and irradiated for 6, 9, 12 and 18 months (10.1 ± 2.0–12.3 ± 2.1 µm y⁻¹).

Unirradiated samples indicated the highest corrosion rate after 6 months of thermal loading ($24.3 \pm 2.2 \mu\text{m y}^{-1}$) and the corrosion rate decreased with loading time (13.3 ± 1.6 – $18.0 \pm 1.9 \mu\text{m y}^{-1}$). The samples embedded at BCV bentonite heated up at 90 °C (both irradiated and unirradiated) indicate the highest corrosion rates after 6 months of loading (14.9 ± 1.7 – $17.4 \pm 4.1 \mu\text{m y}^{-1}$). The lowest corrosion rates were observed in samples stored at laboratory temperature without any irradiation (Table 10, Figure 31).

Table 10 Corrosion rates of steel samples given in $\mu\text{m y}^{-1}$. AVG – average, $\pm L$ – confidence interval of the Student's distribution at the significance level $\alpha = 0.05$, IR – irradiated, NIR – unirradiated, 6 (resp. 9, 12 or 18) – the length of heating period in months, MX80 – MX-80 bentonite.

Cell no.	Sample no.	Bentonite	AVG	$\pm L$
1	BCV150IR6	BCV	12	1.5
3	BCV150IR9	BCV	11.1	1.9
5	BCV150IR12	BCV	12.3	2.1
7	BCV150IR18	BCV	10.1	2
2	BCV150NIR6	BCV	24.3	3.2
4	BCV150NIR9	BCV	18	1.9
6	BCV150NIR12	BCV	13.3	1.6
8	BCV150NIR18	BCV	17.5	1.1
12	BCV90IR9	BCV	14.9	1.7
14	BCV90IR12	BCV	11.7	1.8
16	BCV90IR18	BCV	9.3	1.4
13	BCV90NIR9	BCV	17.4	4.1
15	BCV90NIR12	BCV	13.1	2.1
17	BCV90NIR18	BCV	12.9	2.3
20	BCVRTNIR6	BCV	6	0.8
21	BCVRTNIR9	BCV	4.7	0.2
22	BCVRTNIR12	BCV	3.6	0.6
23	BCVRTNIR18	BCV	2.6	0.1
9	MX80150IR18	MX80	17.2	0.3
10	MX80150NIR18	MX80	18.9	0.3
11	MX80RTNIR18	MX80	2.2	0.1
18	MX8090IR18	MX80	4.7	0.1
19	MX8090NIR18	MX80	4.5	0.7

Different corrosion rates were observed when steel samples were embedded at MX-80 bentonite (Figure 32). The highest corrosion rates were observed when steel samples were embedded at MX-80 bentonite and heated up at 150 °C (both irradiated and unirradiated, $17.2 \pm 0.3 \mu\text{m y}^{-1}$, resp. $18.9 \pm 0.3 \mu\text{m y}^{-1}$). The steel samples embedded at MX-80 bentonite heated up at 90 °C indicate much lower corrosion rates ($2.2 \pm 0.1 \mu\text{m y}^{-1}$ resp. $4.7 \pm 0.1 \mu\text{m y}^{-1}$) comparable to those of thermally unloaded samples ($4.5 \pm 0.7 \mu\text{m y}^{-1}$) (Figure 32).

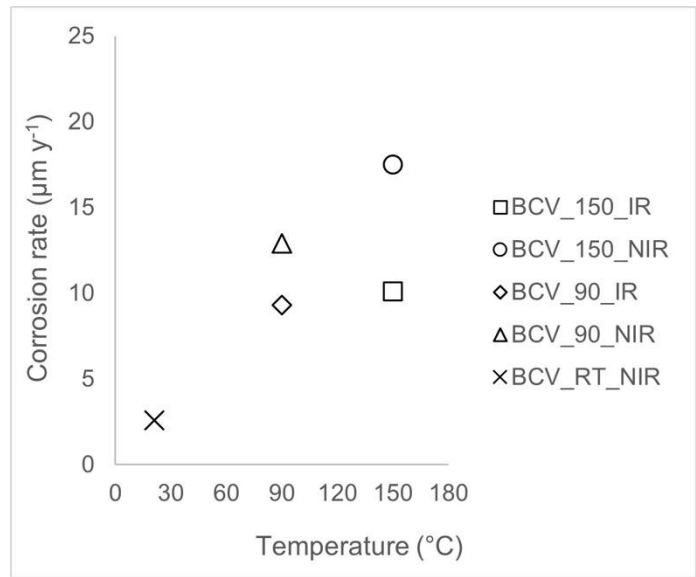


Figure 31 Corrosion rate of steel samples loaded at BCV bentonite at 150 °C , 90 °C and at laboratory temperature (RT) for 18 months. IR – irradiated, NIR – unirradiated.

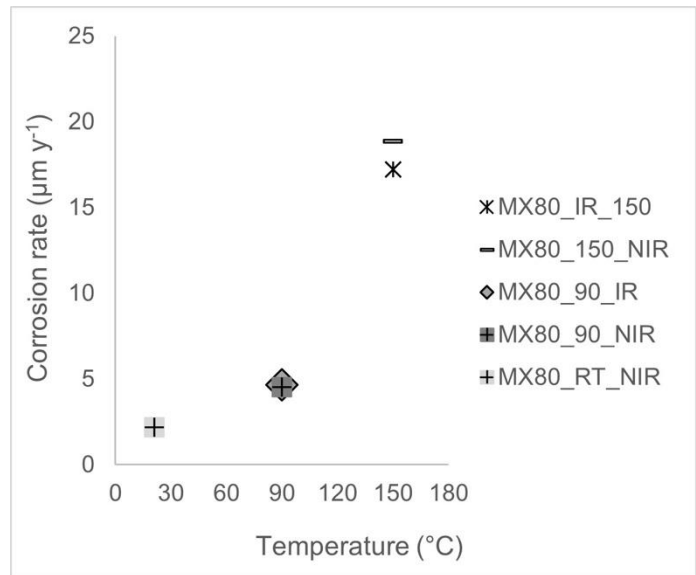


Figure 32 Corrosion rate of steel samples embedded at MX-80 bentonite heated up at 150 °C, 90 °C and at laboratory temperature (RT) for 18 months. IR – irradiated, NIR – unirradiated.

2.6.2 SEM-EDX and LOM

Light optical microscopy (LOM) analysis confirmed ferritic-pearlitic microstructure of steel samples (Figure 33). The transition from ferritic-pearlitic microstructure to spheroidal microstructure was observed only in one steel sample in BCV bentonite in the cell no. 2 heated up at 150 °C without irradiation for 6 months. Pearlite was found forming lamellae up to 30 µm thick in all steel samples. The steel's surface roughness revealed the presence of surface depressions, which were approximately 25–30 µm deep and filled with corrosion products. These corrosion products formed a layer partially covering the steel surface for samples loaded for 6–9 months or completely covering it. The thickness of the corrosion layer varied, ranging from 10 to 45 µm, and was directly correlated with the duration of loading.

Irradiation and thermal loading at 150 °C led to the formation of thinner corrosion layers, typically ranging from 10 to 20 µm (Figure 34). Similar thickness of corrosion layer (5 to 20 µm) was found in the steel samples that remained unirradiated (Figure 35). More extensive corrosion layers (20 to 45 µm thick)

were identified in the steel samples heated up at 90 °C (Figure 36-Figure 37) showing no difference regarding to the irradiation.

Employing SEM-EDS analysis it was found different composition of corrosion products dependent on the temperature of thermal loading. Two discrete layers originated at 90 °C: a layer of Fe-oxide (Fe-oxy-hydroxide) and a layer of carbonates mixed with minerals coming from bentonite. On the other hand, the steel samples heated up at 150 °C contain: a layer composed of Fe-Si-O(OH) and a layer of carbonates mixed with minerals coming from bentonite (Figure 33-Figure 35). The formation of Fe-Si-O(OH) layer is more obvious in samples heated at 150 °C and irradiated (Figure 34). These results partially correlate with the composition of corrosion products determined through XRD analysis. These included magnetite, Fe-rich carbonates, and a mixture of magnetite and clay minerals originating from the bentonite. The presence of Fe-Si-rich phases was not identified.

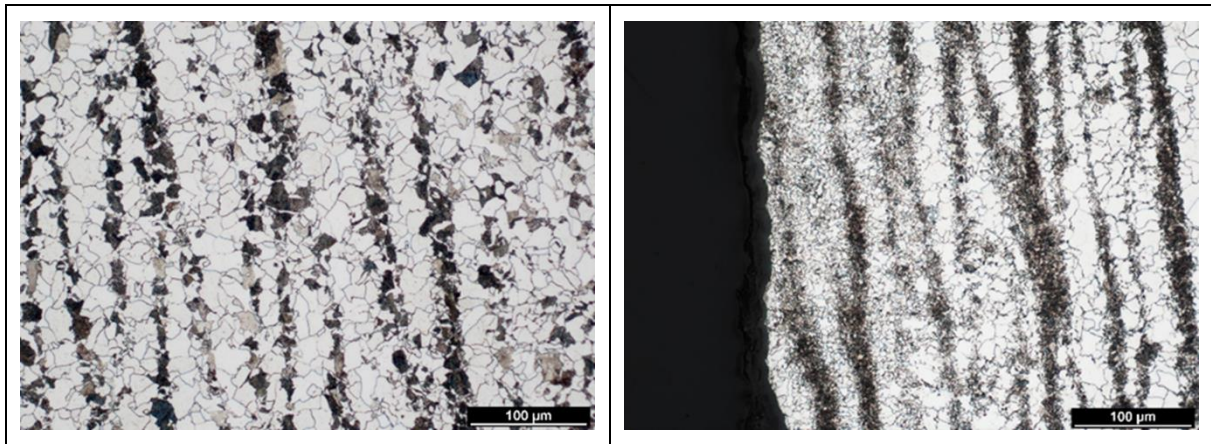


Figure 33 Steel microstructure ferritic-pearlitic (left) and ferritic-pearlitic with spheroidal areas (right) (cell no. 2).

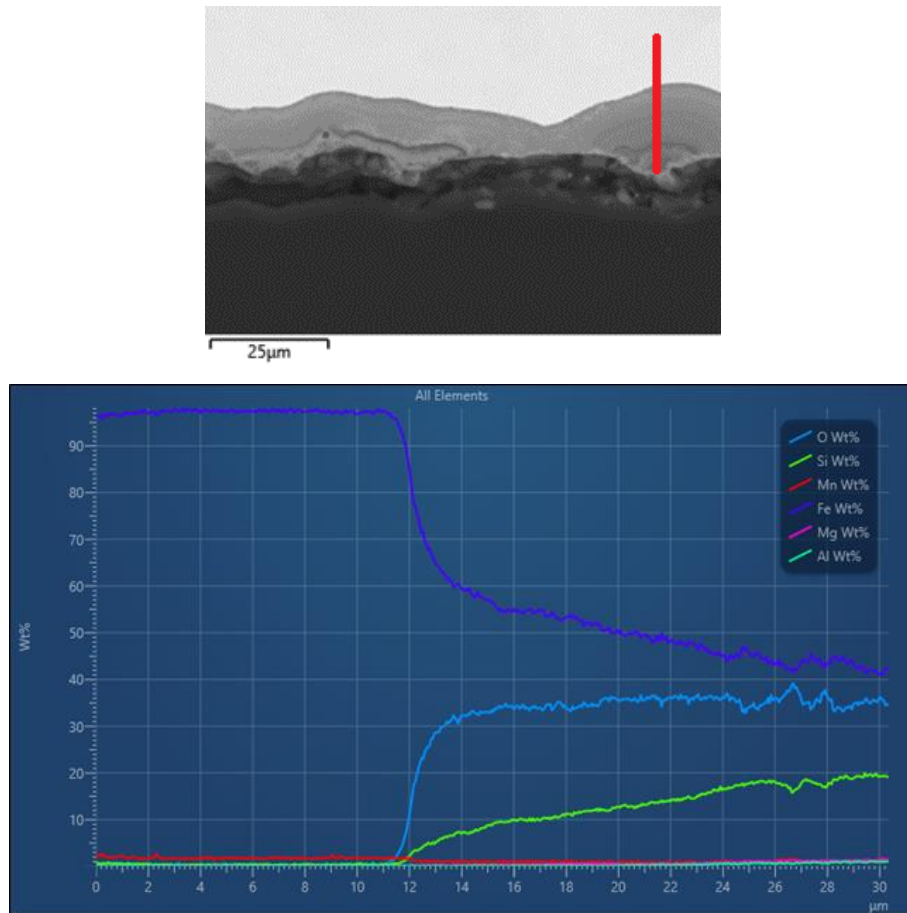


Figure 34 Corrosion layer on the surface of irradiated steel samples embedded in BCV bentonite heated at 150 °C for 12 months (cell no. 5). SEM images including red line indicating position of the profile analysed by EDS (left) and the profile analysis.

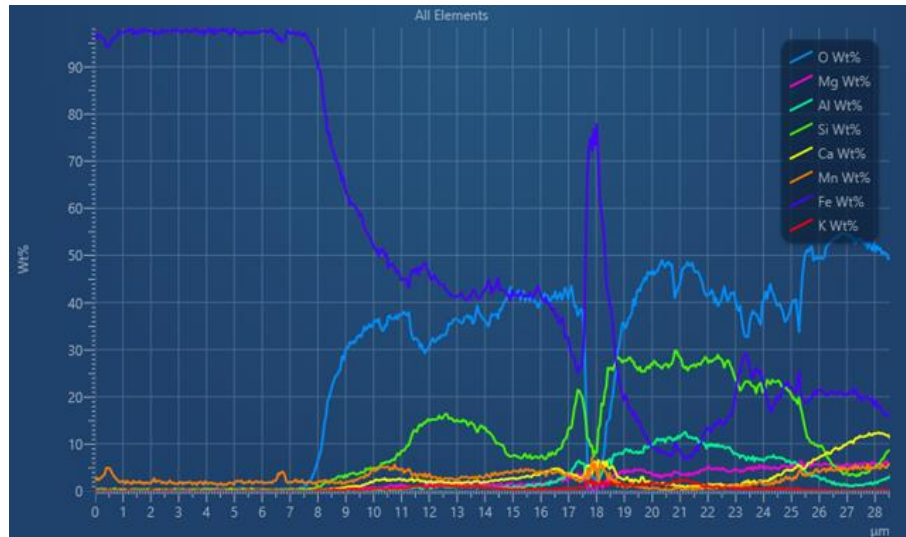
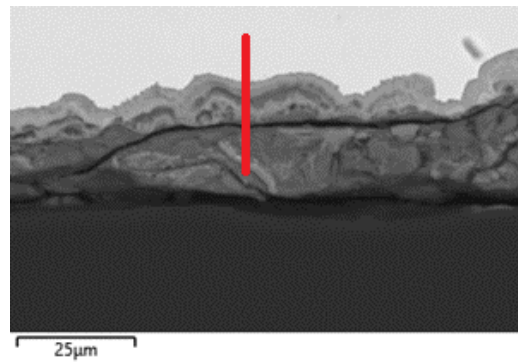


Figure 35 Corrosion layer on the surface of unirradiated steel samples embedded in BCV bentonite heated up at 150 °C for 12 months (cell no. 6). SEM images including red line indicating position of the profile analysed by EDS (left) and the profile analysis.

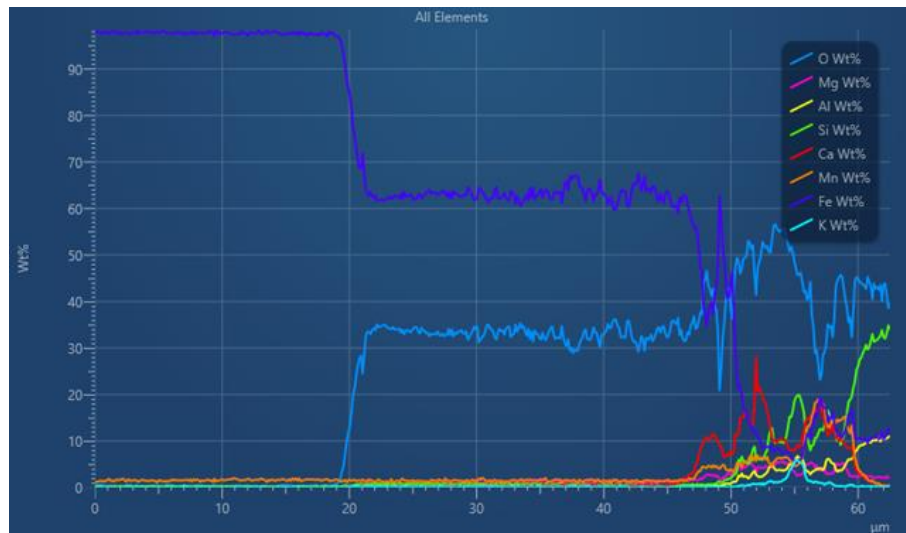
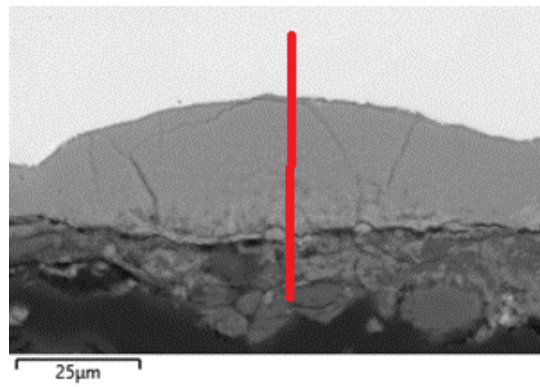


Figure 36 Corrosion layer on the surface of irradiated steel samples embedded in BCV bentonite heated up at 90 °C for 12 months (cell no. 14). SEM images including red line indicating position of the profile analysed by EDS (left) and the profile analysis (right).

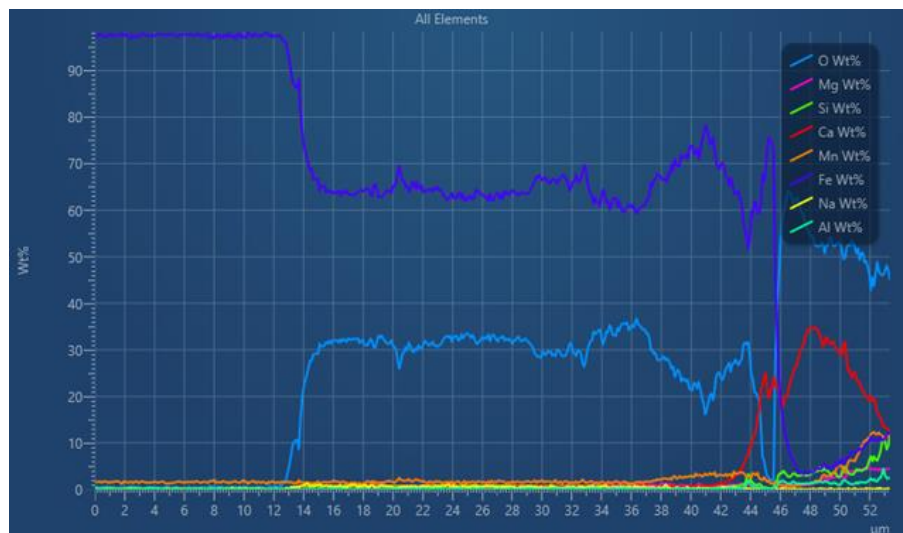
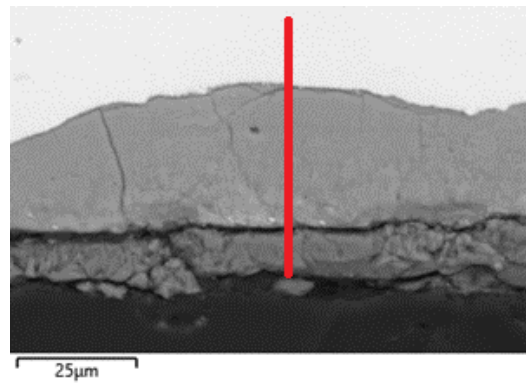


Figure 37 Corrosion layer on the surface of unirradiated steel samples embedded in BCV bentonite heated up at 90 °C for 12 months (cell no. 15). SEM images including red line indicating position of the profile analysed by EDS (left) and the profile analysis (right).

Steel samples embedded in MX80 bentonite heated up at 150 °C and irradiated for 18 months exhibited corrosion layer 30-50 μm thick (Figure 38). The thickness of the corrosion layer is comparable or slightly higher comparing to those embedded in BCV bentonite and loaded under similar conditions (Figure 39). Both corrosion layers are typical with Fe-Si-O composition.

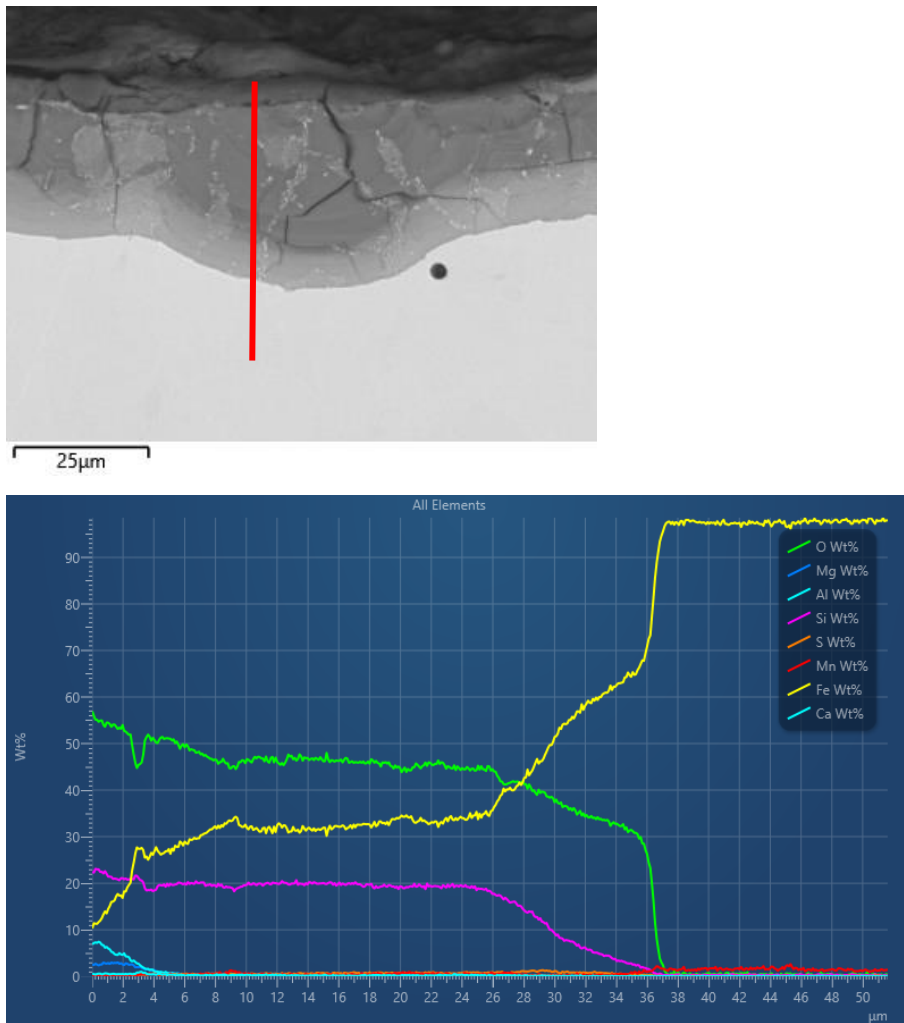


Figure 38 Corrosion layer on the surface of irradiated steel samples embedded in MX80 bentonite heated at 150 °C for 18 months (cell no. 9). SEM images including red line indicating position of the profile analysed by EDS (left) and the profile analysis.

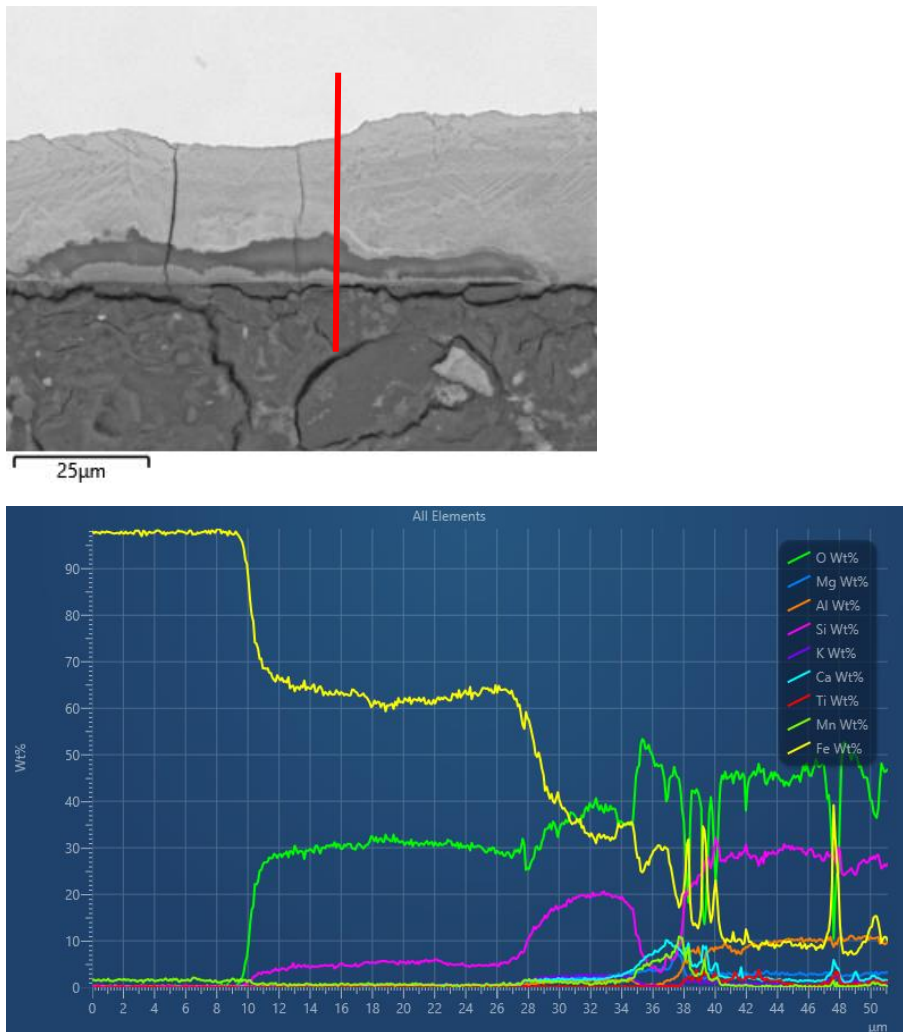


Figure 39 Corrosion layer on the surface of irradiated steel samples embedded in BCV bentonite heated at 150 °C for 18 months (cell no. 9). SEM images including red line indicating position of the profile analysed by EDS (left) and the profile analysis.

2.6.3 Profilometry

Based on the profilometry analysis it was confirmed surface corrosion of the steel samples embedded in the BCV bentonite. The degree of the corrosion was quantified based on the mean value and variation, both related to the reference plane. The mean value and colour map of the BLANK sample (Figure 40, Table 11) reflect roughness of the surface related to the steel preparation and grinding prior to the experiment. Lower mean values of the selected steel samples (e.g., cells no.1–5) comparing to the BLANK steel sample reflect limitations connected to the profilometry analysis as well as surface smoothing connected to the corrosion (Table 11).

Table 11 Deviation from the reference Mean value and variance from reference point based on profilometry.

Cell no.	Side A			Side B		
	Mean value (µm)	Standard mean deviation (µm)	Variation (µm ²)	Mean value (µm)	Standard mean deviation (µm)	Variation (µm ²)
1	0.00	3.35	11.24	n.a.	n.a.	n.a.
3	0.00	3.72	13.85	-0.02	4.21	17.74
5	0.16	4.95	24.46	0.18	4.54	20.61
2	0.02	3.29	10.85	n.a.	n.a.	n.a.
4	-0.03	4.43	19.59	0.08	4.21	17.71
6	0.36	4.76	22.63	0.03	5.51	30.33
12	0.28	5.54	30.66	1.15	8.64	74.65
14	-2.00	9.71	94.3	-0.64	6.73	45.25
13	-1.35	11.08	122.72	-0.46	8.13	66.07
15	-2.39	10.59	112.23	-1.11	9.31	86.67
22	0.24	4.01	16.05	0.49	3.98	15.82
BLANK	0.27	3.76	14.15	0.04	2.19	4.8

Corrosion of the steel sample embedded in BCV bentonite at laboratory temperature indicates minor corrosion propagating along the initial surface inhomogeneities (Figure 40). Continuous corrosion correlating with the loading period was documented in all steel samples heated up at 150 °C (Figure 41) and 90 °C (Figure 42). After 12 months of loading corrosion affected the steel surface completely. The most extensive corrosion located in the outer parts of steel coupons.

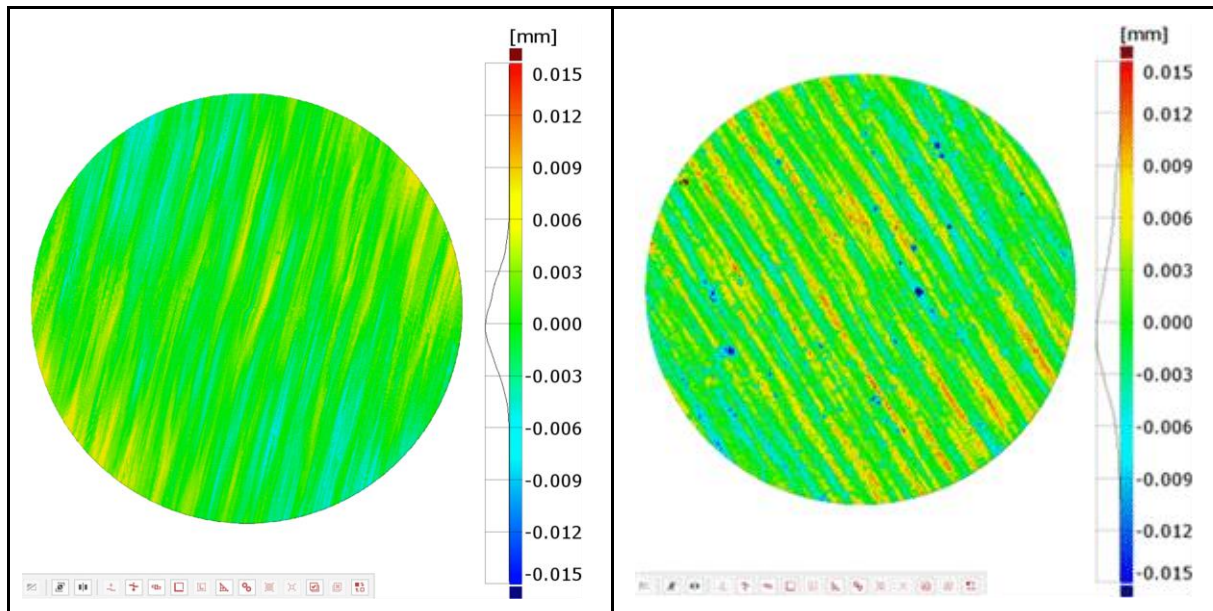
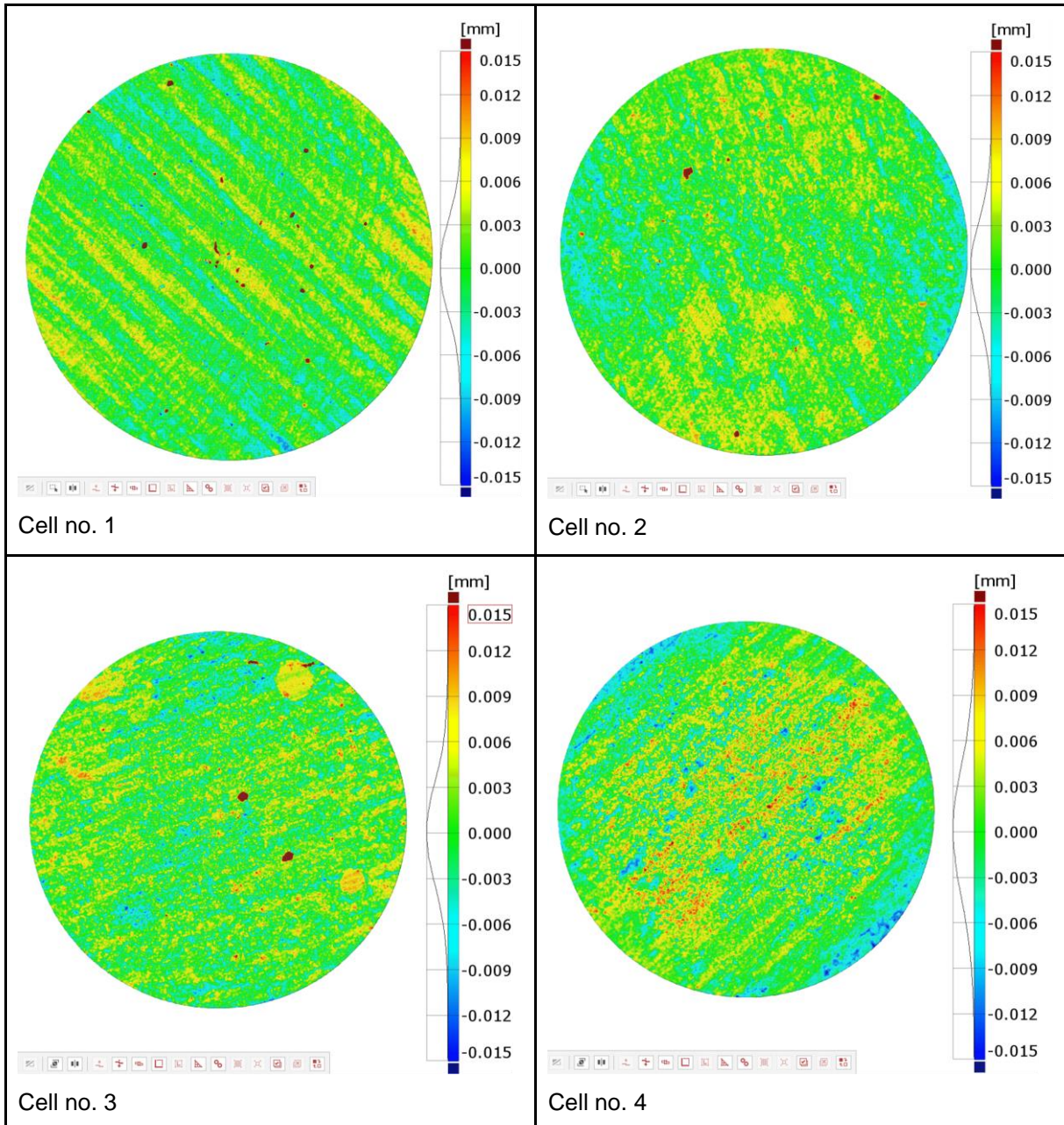


Figure 40 Comparison of the profilometry analysis of the BLANK steel sample (on the left) with unirradiated steel sample loaded in BCV bentonite at laboratory temperature for 12 months (on the right).



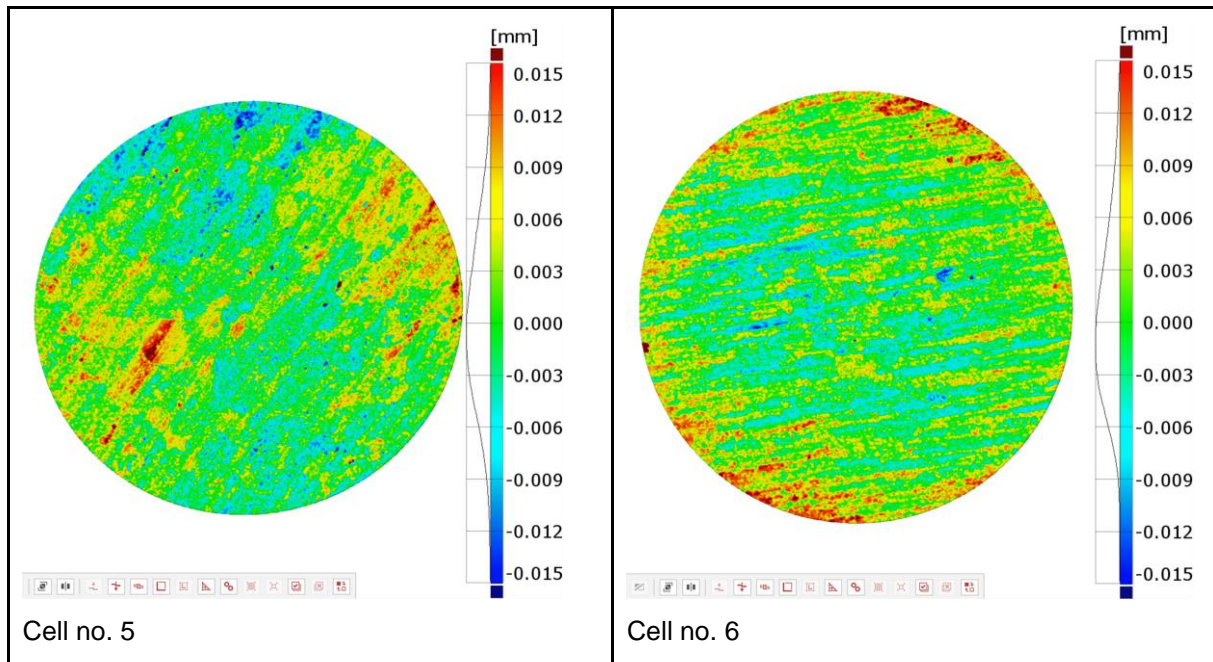


Figure 41 Comparison of the profilometry analysis of steel samples embedded in BCV bentonite heated up at 150 °C and irradiated for 6 (cell no. 1), 9 (cell no. 3) and 12 (cell no. 5) with the unirradiated ones (cells no. 2, 4 and 6).

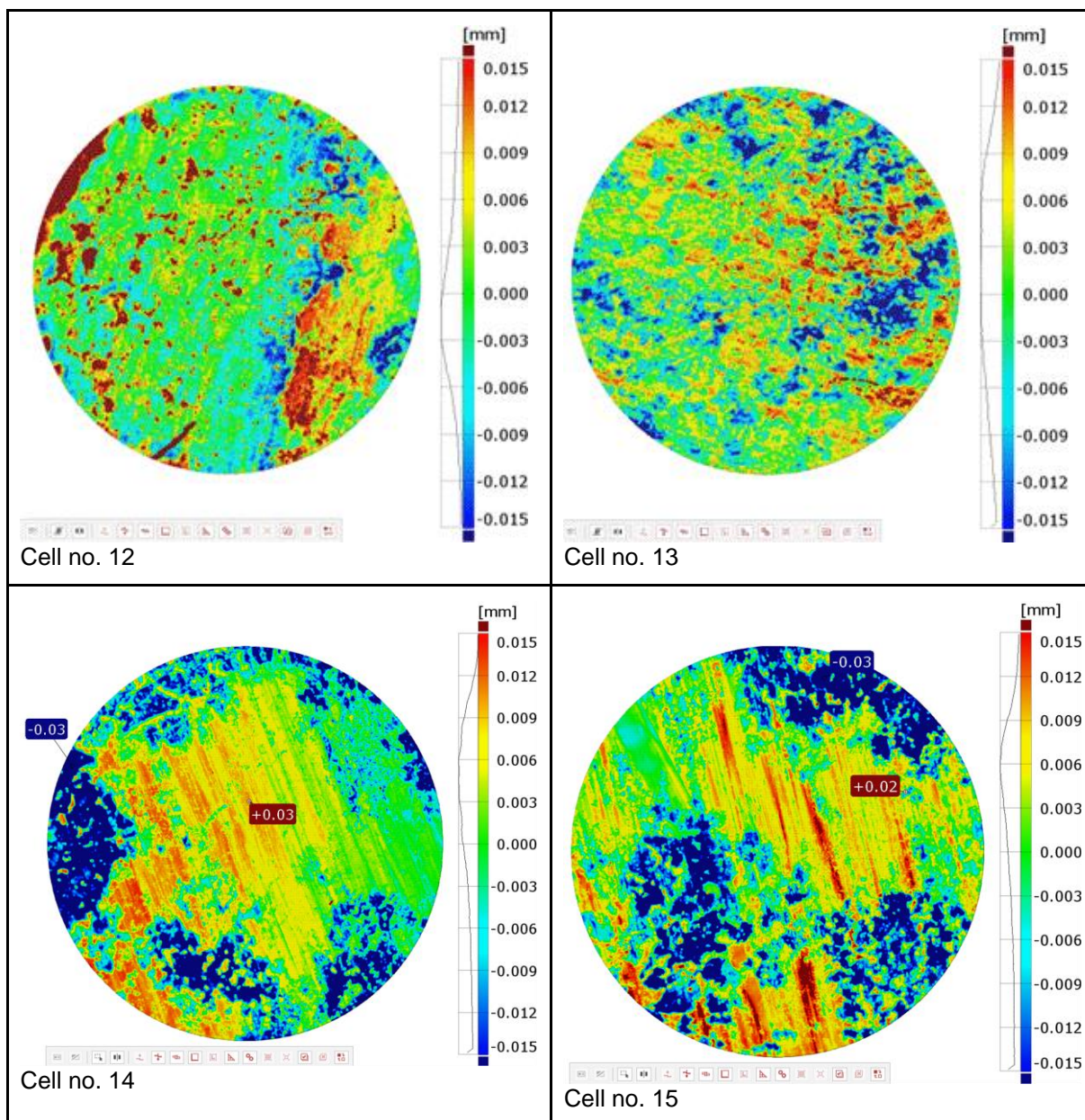


Figure 42 Comparison of the profilometry analysis of steel samples embedded in BCV bentonite heated up at 90 °C and irradiated for 9 (cell no. 12) and 12 (cell no. 14) with the unirradiated ones (cells no. 13 and 15).

2.6.4 XRD and Raman spectroscopy

Bulk mineralogical composition of the BCV bentonite is shown in Table 12. The BCV_input bentonite is dominated by smectite (montmorillonite, $d_{060} \sim 1.50 \text{ \AA}$), accompanied by quartz and kaolinite. Illite, and goethite were analysed in amount $< 5 \text{ wt. \%}$. Anatase, calcite, aragonite, ankerite, siderite, fluorapatite, augite, rutile and sanidine were analysed in amount $< 1 \text{ wt. \%}$. There is expected $\sim 7\text{-}10 \text{ wt. \%}$ of amorphous phases in the BCV bentonite (Červinka et al. 2018). Amorphous phases were not included in the analysis due to inaccuracy connected to its quantification in the bentonite analyses (e.g., Ufer et al. 2008; Heuser 2018).

Heated bentonite showed minor changes in the content of smectite compared to BCV_input sample. Very minor changes in the content of other minerals coincide with the resolution limits of the method. Illite content of heated samples is comparable to those in the BCV_input bentonite which excludes effect

of illitization (e.g., Inoue et al. 1988; Madsen et al. 1988, Pusch and Karnland 1988). Very minor changes in illite reflect very low K⁺ content in SGW3 used as a saturation medium. Increasing K⁺ content combined with increasing temperature and time is regarded as a main factor affecting illitization of smectite (e.g., Mosser-Ruck et al. 1999; Pusch et al. 2010).

Table 12 Semiquantitative XRD of randomly oriented powder mounts.

Sample no.	Smc	Kaol	Ill	Qz	Arg	Cal	Ank	Sd	Gth	Snd	Aug	F-apt	Ant	Rtl
BCV_input	72.5	6.2	2.2	10.0	0.6	1.1	0.3	0.6	2.6	2.0	0.0	0.0	1.9	0.0
BCV_150_IR_6m	72.5	3.6	3.0	9.7	nd	1.2	0.5	0.2	4.0	1.2	0.6	1.2	2.1	0.3
BCV_150_IR_9m	73.1	3.3	2.8	10.2	0.1	0.4	0.5	0.1	4.2	1.1	1.1	1.1	2.1	0.1
BCV_150_6m	73.9	2.9	3.1	9.8	nd	0.3	0.5	0.2	3.7	1.7	0.5	1.2	2.1	0.2
BCV_150_9m	69.7	5.2	2.6	10.8	0.3	1.0	0.5	0.3	3.8	1.7	0.5	1.1	2.3	0.2
BCV_90_IR_9m	70.7	4.9	2.7	11.2	0.1	0.8	0.4	0.2	3.6	1.6	0.1	1.3	2.2	0.2
BCV_90_9m	70.9	5.0	2.6	10.6	0.5	1.1	0.4	0.2	3.2	1.6	0.4	1.2	2.3	0.2
BCV_RT_6m	68.4	6.0	2.8	10.3	1.0	1.1	0.5	0.3	3.5	1.7	0.7	1.3	2.2	0.2
BCV_RT_9m	70.3	5.2	2.6	11.2	0.4	0.8	0.5	0.0	2.6	1.0	nd	0.9	2.0	nd

Fe-rich carbonates and Magnetite were identified as a main corrosion product in the steel samples embedded in BCV bentonite heated up at 90 °C and 150 °C by XRD. Chukanovite and siderite were identified in all samples confirming anoxic conditions of the experiment. In all analyses iron and minerals coming from bentonite (montmorillonite, illite, quartz and calcite) were detected as a relic of surrounding material. Presence of silicate-based corrosion products was not confirmed by XRD. The main reason is regarded in very low amount of corrosion products and their possible amorphous character which complicates their identification.

2.6.5 Bentonite chemical composition

The chemical composition of BCV bentonite (Table 13) indicated increased content of Fe₂O₃ in all samples (Figure 43a) and increased content of MnO in heated up samples (Figure 43b, 90 and 150 °C). The main source of both species is regarded in the steel samples. Due to alteration of steel samples the corrosion products originate forming mixed structures with bentonite.

The CaO content (Figure 43c) decreased rapidly after 6 months in all heated samples and returned to its original values after 12 months of heating up at 150 °C. Continuous decrease of CaO content was observed in bentonite heated up at 90 °C. MgO content decreased in all heated up samples for the whole heating period (6, 9, 12, resp, 18 months, Figure 43d). Increase in K₂O content indicated possible smectite illitization (Figure 43e). Variable loss of ignition reflects partial drying of the samples during the bentonite pulverizing.

Table 13 Chemical composition of BCV bentonite heated up at 150 °C (150), 90 °C (90) and at ambient temperature (RT), irradiated (IR) or unirradiated (NIR) (in wt.%). The data were recalculated to the 0.00 wt.% of loss of ignition.

Bentoni te no.	BCV_I N	BCV- 150- IR-6	BCV- 150- IR-9	BCV- 150- IR-12	BCV- 150- NIR-6	BCV- 150- NIR-9	BCV- 150- NIR- 12	BCV- 90- IR-9	BCV- 90- IR-12	BCV- 90- NIR-9	BCV- 90- NIR- 12	BCV- RT- NIR-6	BCV- RT- NIR-9	BCV- RT- NIR- 12
Na ₂ O	0.35	0.42	0.40	0.35	0.42	0.39	0.42	0.33	0.33	0.35	0.33	0.32	0.31	0.28
MgO	3.34	3.24	3.27	3.02	3.32	3.20	3.13	3.27	3.22	3.29	3.23	3.30	3.28	3.25
Al ₂ O ₃	20.31	19.47	19.00	18.80	19.05	19.08	18.73	19.10	18.92	19.18	18.93	19.31	19.38	19.01
SiO ₂	54.44	55.13	54.99	54.34	54.64	54.54	54.19	54.22	54.42	54.09	54.47	54.60	54.91	54.82
P ₂ O ₅	0.56	0.58	0.56	0.62	0.57	0.58	0.60	0.54	0.58	0.55	0.57	0.54	0.54	0.59
SO ₃	0.04	0.07	0.06	0.08	0.06	0.06	0.12	0.07	0.09	0.08	0.10	0.07	0.07	0.08
K ₂ O	1.04	1.12	1.18	1.18	1.14	1.20	1.17	1.15	1.15	1.14	1.15	1.19	1.18	1.17
CaO	3.29	3.15	3.18	3.28	3.16	3.20	3.32	3.17	3.09	3.12	3.09	3.17	3.14	3.18
TiO ₂	2.92	2.64	2.71	3.02	2.61	2.86	3.00	2.96	3.03	3.07	2.94	2.93	2.83	3.05
V ₂ O ₅	0.05	0.04	0.00	0.00	0.03	0.00	0.00	0.00	0.00	0.00	0.00	0.00	0.00	0.00
Cr ₂ O ₃	0.07	0.08	0.08	0.09	0.09	0.08	0.08	0.08	0.08	0.08	0.08	0.08	0.08	0.08
MnO	0.21	0.23	0.22	0.24	0.24	0.25	0.26	0.23	0.23	0.22	0.23	0.20	0.20	0.26
Fe ₂ O ₃	13.19	13.46	13.97	14.78	14.16	14.41	14.83	14.42	14.71	14.48	14.72	14.14	13.91	14.04
Co ₂ O ₃	0.01	0.01	0.01	0.01	0.01	0.01	0.01	0.01	0.01	0.01	0.01	0.01	0.01	0.01
NiO	0.02	0.03	0.03	0.03	0.03	0.03	0.03	0.03	0.03	0.03	0.03	0.03	0.03	0.03
BaO	0.08	0.23	0.24	0.05	0.31	0.00	0.00	0.13	0.00	0.19	0.00	0.00	0.00	0.04
Others	0.08	0.10	0.12	0.11	0.16	0.12	0.11	0.30	0.11	0.12	0.12	0.12	0.12	0.12
Total	100	100.	100	100	100	100	100	100	100	100	100	100	100	100
LOI	15.95	23.50	20.70	8.02	20.20	18.70	10.30	19.20	9.37	19.20	9.66	18.70	19.50	9.51

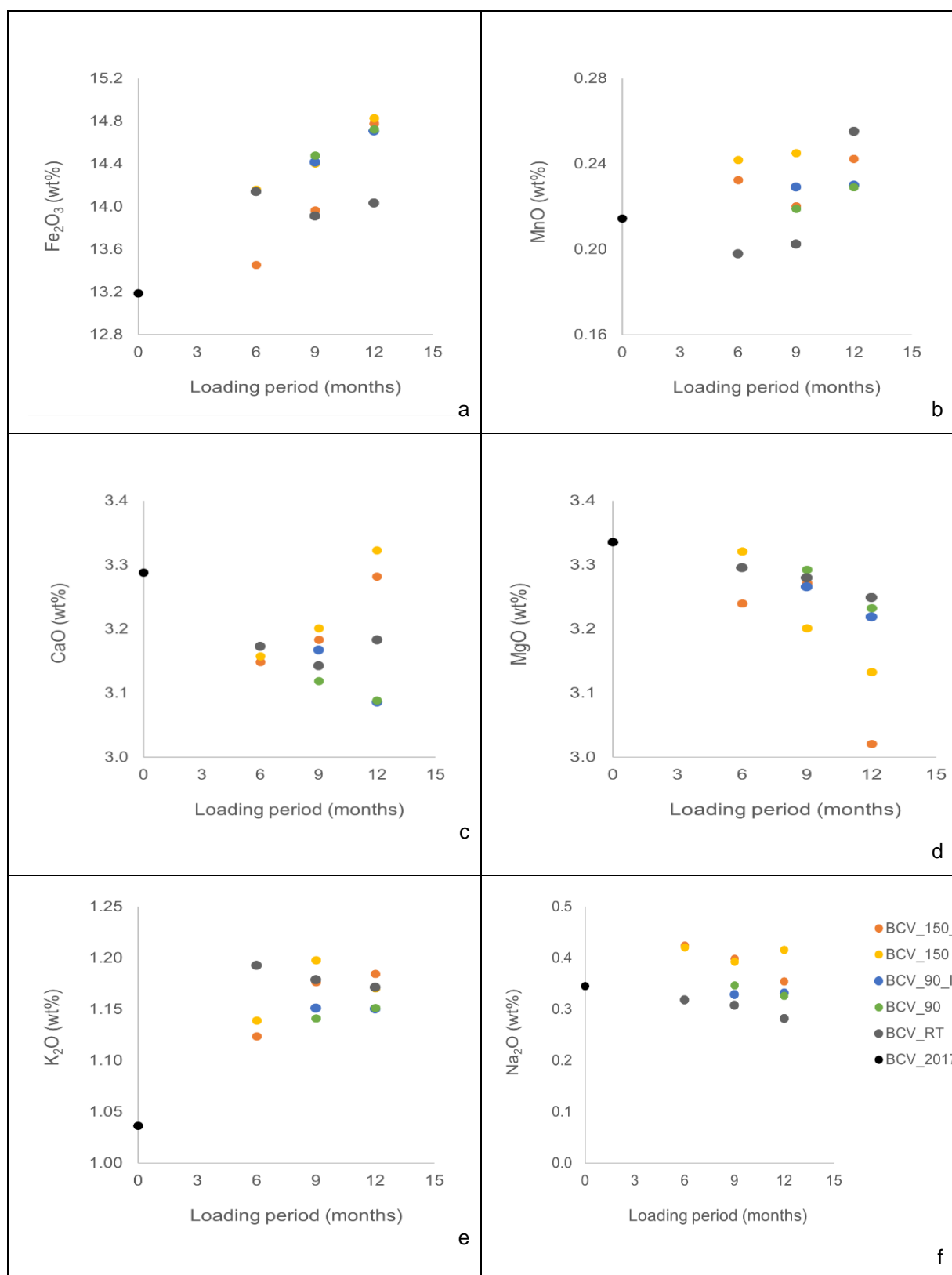


Figure 43 Fe₂O₃ (a), MnO (b), CaO (c), MgO (d), K₂O (e) and Na₂O (f) content in original bentonite (BCV_2017_7) and bentonite heated up at 150 °C (150), 90 °C (90) and at ambient temperature (RT), irradiated (IR) or unirradiated (NIR).

2.6.6 Cation exchange capacity

The BCV_input bentonite is dominated by Mg²⁺ followed by Ca²⁺ in the position of exchangeable cations (Table 14). The CEC analysed spectroscopically (CEC_{vis}) of the BCV_input bentonite equals to 59.4 ±

2.4 meq/100g. The sum of exchangeable cations CEC_{sum} is comparable (59.3 ± 0.5 meq/100g). Heated BCV bentonite exhibited increasing CEC_{sum} and CEC_{vis} values when heated up to 150 °C. Heating led to higher proportion of exchangeable Ca²⁺ and a lower proportion of Mg²⁺ which are phenomena typical for thermal loading of Ca-Mg bentonites (e.g., Kašpar et al. 2021). A slight increase in Na⁺ in exchangeable cation in heated bentonite is explained by higher content of Na⁺ in SGW3. This may be related to CEC_{vis} and CEC_{sum} increase.

Table 14 The CEC analysed spectroscopically (CEC_{vis}), the sum of exchangeable cations (CEC_{sum}) and the proportions of exchangeable cations in the BCV_{input} bentonite and BCV bentonite heated up to 150 °C (150), irradiated (IR) or unirradiated (NIR) for 6 (6m), 9 (9m), 12 (12m) and 18 months (18m).

Sample no.	CEC _{vis}		CEC _{sum}		Ca ²⁺		Mg ²⁺		Na ⁺		K ⁺	
	AVG	± L	AVG	± L	AVG	± L	AVG	± L	AVG	± L	AVG	± L
BCV _{input}	59.4	2.4	59.3	0.5	24.3	0.3	63.9	0.7	9.4	0.5	2.3	0.2
BCV_150_IR_6m	66.4	1.8	63.2	1.1	60.8	0.8	22.9	0.6	13.9	0.2	2.3	0.1
BCV_150_IR_9m	67.2	1.4	64.2	2.9	59.1	0.8	27.0	0.6	11.2	0.3	2.8	0.1
BCV_150_IR_12m	66.4	2.4	69.8	1.1	70.3	0.6	16.3	0.4	10.5	0.1	2.9	0.1
BCV_150_IR_18m	68.4	1.7	70.1	2.6	70.3	0.1	15.2	0.5	12.1	0.6	2.3	0.0
BCV_150_6m	67.7	4.2	63.5	3.1	66.8	0.8	16.3	0.5	14.3	1.0	2.5	0.1
BCV_150_9m	67.4	3.1	61.5	1.6	69.1	1.0	15.5	0.2	12.5	0.7	3.0	0.2
BCV_150_12m	66.7	17.2	70.9	1.7	73.1	0.3	10.5	0.2	13.3	0.0	3.2	0.1
BCV_150_18m	69.7	1.5	72.3	1.1	78.6	0.3	7.7	0.2	11.1	0.2	2.6	0.1

2.6.7 Water leachates

The chemical composition of water leachates of BCV_{input} bentonite and bentonite heated up at 90 and 150 °C indicates prevailing Na-HCO₃ type (Table 15). The concentration is dependent on solid-to-liquid (s : l) ratio (Figure 44). There was observed significant effect of both temperature and irradiation on the concentration of water leachable species.

Thermal loading at 150 °C decreased a concentration of water leachable Na⁺, K⁺ and Mg²⁺ and slightly increased a concentration of Ca²⁺ and Cl⁻. Only minor effect was observed on SO₄²⁻ in unirradiated BCV bentonite. Thermal loading at 90 °C decreased a concentration of water leachable Na⁺ and Mg²⁺ and slightly increased a concentration of K⁺, Ca²⁺, Cl⁻ and SO₄²⁻. Only minor effect was observed on Mg²⁺. A concentration of HCO₃⁻ decreased in all heated up samples.

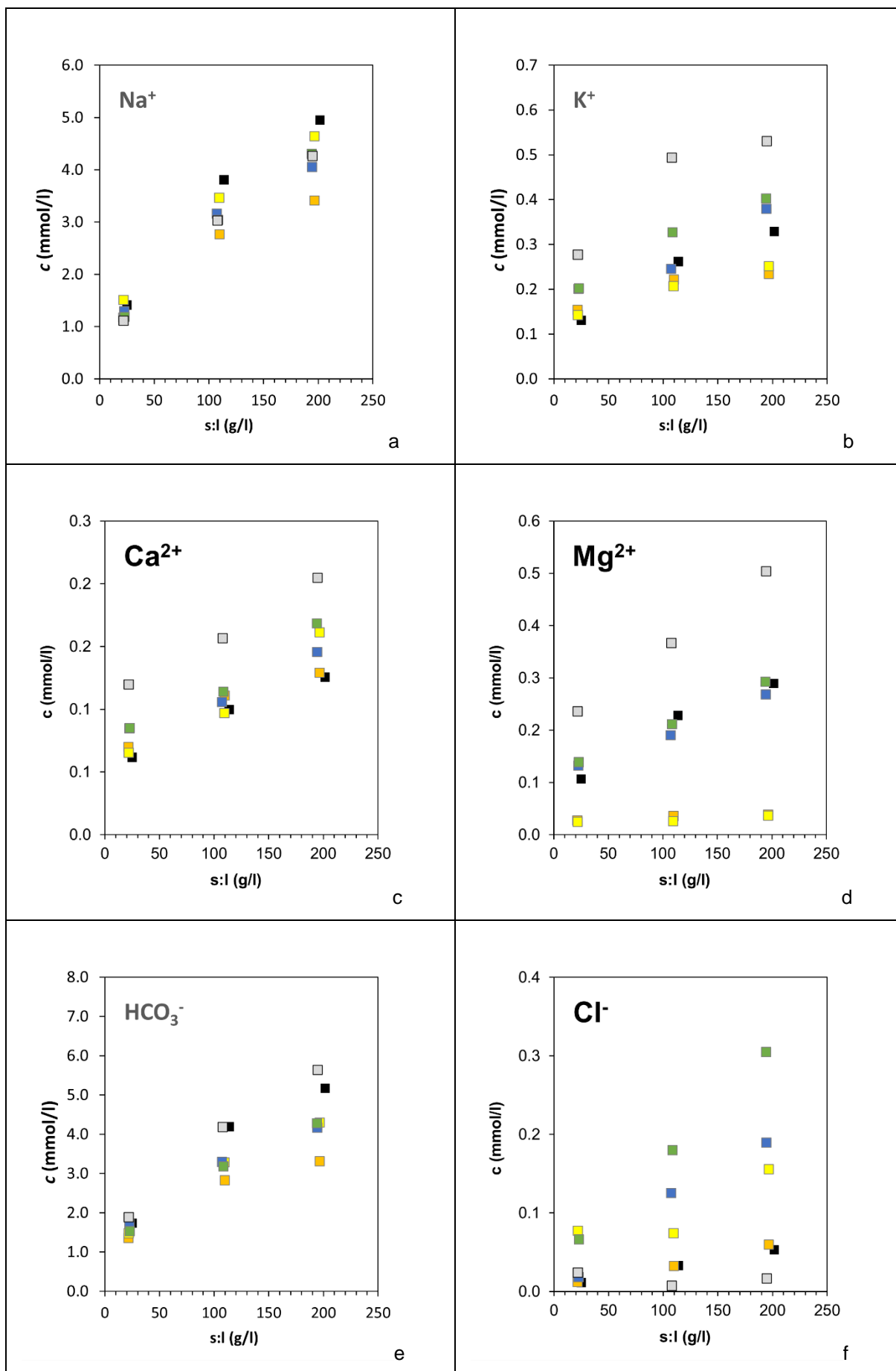
Irradiation decreased the concentration of water leachable Na⁺, Ca²⁺, Cl⁻ and SO₄²⁻. No effect of irradiation was observed on K⁺, Mg²⁺ and HCO₃⁻.

Table 15 Concentration of water leachates in BCV_{input} and BCV heated up at 150 °C (150), 90 °C (90), ambient temperature (RT), irradiated (IR) and unirradiated (NIR).

Sample no.	s : l (g/L)	Na ⁺	K ⁺	Ca ²⁺	Mg ²⁺	Fe ³⁺	Cl ⁻	SO ₄ ²⁻	NO ₃ ⁻	F ⁻	HCO ₃ ⁻
BCV _{input}	25.18	1.41	0.13	0.06	0.11	bdl	0.01	0.06	bdl	0.03	1.73
	114.03	3.80	0.26	0.10	0.23	bdl	0.03	0.25	bdl	0.09	4.19
	201.94	4.95	0.33	0.13	0.29	bdl	0.05	0.44	bdl	0.10	5.17
BCV150IR6	23.82	1.51	0.12	0.04	0.03	bdl	0.04	0.09	bdl	bdl	1.54
	115.97	3.14	0.16	0.06	0.04	bdl	0.10	0.29	bdl	bdl	2.81
	209.18	4.09	0.20	0.10	0.05	bdl	0.16	0.45	bdl	bdl	3.52
BCV150NIR6	23.55	1.56	0.12	0.05	0.02	bdl	0.04	0.11	bdl	bdl	1.57
	113.39	3.36	0.18	0.08	0.03	bdl	0.12	0.28	bdl	bdl	3.06
	203.69	4.47	0.22	0.12	0.03	bdl	0.20	0.43	bdl	bdl	3.93
BCV150IR9	118.10	2.73	0.22	0.06	0.04	bdl	0.06	0.28	bdl	bdl	2.56

EURAD Deliverable 15.8 – Synthesis of irradiation results under repository conditions

BCV150NIR9	22.67	1.31	0.14	0.04	0.02	bdl	0.05	0.10	bdl	bdl	1.32
	113.22	2.64	0.19	0.07	0.02	bdl	0.11	0.27	bdl	bdl	2.36
	203.12	3.50	0.22	0.11	0.02	bdl	0.13	0.38	bdl	bdl	3.09
BCV150IR12	21.82	1.17	0.15	0.07	0.03	bdl	0.01	0.08	bdl	bdl	1.36
	109.75	2.76	0.22	0.11	0.04	bdl	0.03	0.21	bdl	bdl	2.82
	196.70	3.41	0.23	0.13	0.04	bdl	0.06	0.30	bdl	bdl	3.31
BCV150NIR12	21.93	1.50	0.14	0.07	0.02	bdl	0.08	0.11	0.04	bdl	1.48
	109.47	3.46	0.21	0.10	0.03	bdl	0.07	0.28	bdl	bdl	3.28
	196.60	4.64	0.25	0.16	0.04	bdl	0.16	0.42	bdl	bdl	4.30
BCV90IR9	117.54	3.20	0.29	0.11	0.21	bdl	0.11	0.31	bdl	bdl	3.39
BCV90NIR9	119.87	3.19	0.26	0.11	0.19	bdl	0.14	0.42	bdl	bdl	3.06
BCV90IR12	22.81	1.29	0.20	0.08	0.13	bdl	0.02	0.09	bdl	bdl	1.72
	107.29	3.16	0.25	0.11	0.19	bdl	0.13	0.29	bdl	bdl	3.29
	194.58	4.05	0.38	0.15	0.27	bdl	0.19	0.45	bdl	bdl	4.16
BCV90NIR12	22.89	1.18	0.20	0.08	0.14	bdl	0.07	0.12	bdl	bdl	1.53
	108.48	3.04	0.33	0.11	0.21	bdl	0.18	0.33	bdl	bdl	3.18
	194.33	4.30	0.40	0.17	0.29	bdl	0.30	0.52	bdl	bdl	4.27
BCVRTNIR6	116.32	2.91	0.39	0.11	0.27	bdl	0.05	0.26	bdl	bdl	3.49
BCVRTNIR9	22.77	1.19	0.25	0.10	0.22	bdl	0.04	0.11	bdl	bdl	1.83
	112.12	2.86	0.39	0.11	0.29	bdl	0.05	0.26	bdl	bdl	3.51
BCVRTNIR12	22.03	1.11	0.28	0.12	0.24	bdl	0.02	0.10	bdl	bdl	1.88
	107.87	3.03	0.49	0.16	0.37	bdl	0.01	0.19	bdl	bdl	4.18
	194.91	4.26	0.53	0.20	0.50	bdl	0.02	0.28	bdl	bdl	5.64



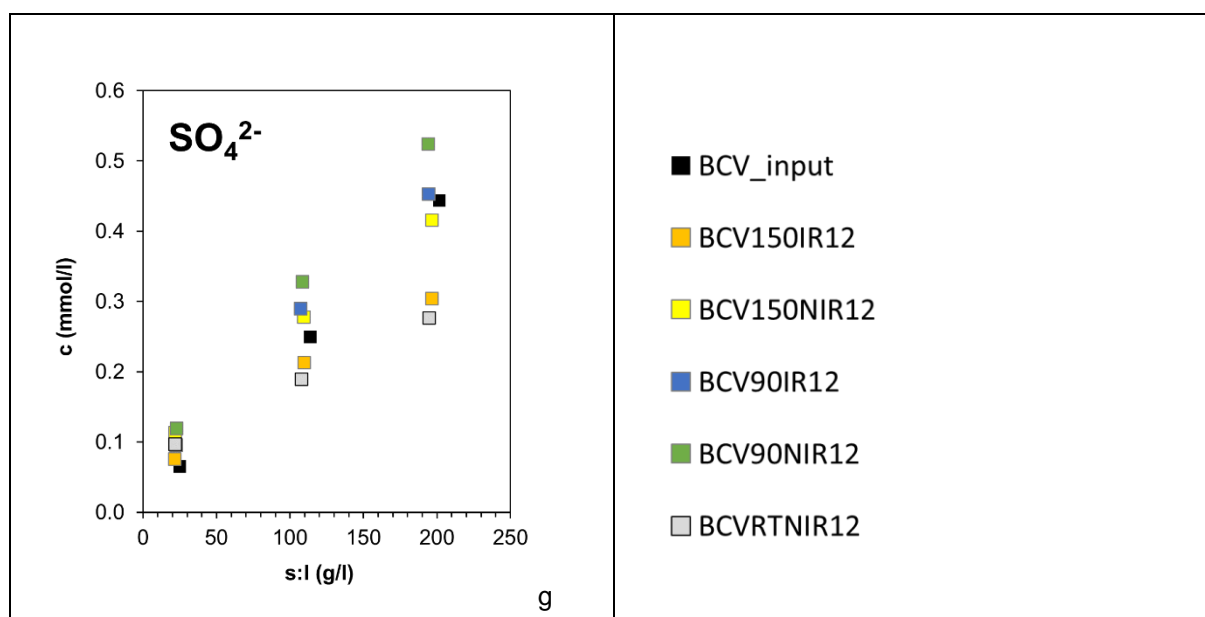


Figure 44 Concentration of Na^+ (a), K^+ (b), Ca^{2+} (c), Mg^{2+} (d), HCO_3^- (e), Cl^- (f) and SO_4^{2-} (g) in water leachates from BCV bentonite heated up at 150 °C (150), 90 °C (90) or laboratory temperature (RT), irradiated (IR) or unirradiated (NIR), loaded for 12 months.

2.7 Discussion

2.7.1 Factors affecting steel corrosion rate

Temperature and degree of saturation are the main factors affecting corrosion rates of steel samples embedded in bentonite. Inhomogeneous saturation of experimental cells increased confidence intervals of corrosion rate of steel embedded in several cells. Unevenly distributed corrosion connected to heterogeneous saturation was observed previously in various clay/bentonite environments (e.g., King 2008; Zuna et al. 2023). Corrosion rates in model environments range from units to tens of $\mu\text{m}/\text{year}$ for most authors (e.g., Neff et al. 2010, Smart et al. 2012). It well corresponds to the corrosion rates analysed in the heated BCV and MX-80 bentonite. Irradiation was found decreasing the corrosion rate of steel samples in BCV bentonite at both loading temperatures (150 and 90 °C). This trend was confirmed by corrosion rates calculated based on mass loss and by mean values and deviations calculated based on profilometry analysis. Similar trend was indicated in MX80 bentonite heated up at 150 °C. Very minor effect of irradiation on steel corrosion was observed in MX80 bentonite heated up at 90 °C.

2.7.2 Factors affecting composition of corrosion products

Fe-oxide and Fe-carbonates were analysed on steel-BCV bentonite surface heated up at 90 °C. A formation of Fe-Si-O(OH) layer was analysed in samples heated up at 150 °C. No or very minor difference was found in the composition of corrosion products regarding to the irradiation.

The thickness of corrosion layer well correlated with the heating temperature and length of loading period. More extensive and thicker layer was identified on steel samples heated up at 90 °C. This feature is explained by higher saturation of bentonite and higher water content, which can facilitate formation of corrosion products. Regarding to the bentonite parameters, irradiation decreased the content of CaO and MgO in the loaded BCV bentonite. Irradiation also decreased concentration of water leachable Na^+ , Ca^{2+} , Cl^- and SO_4^{2-} . No effect of irradiation was observed on water leachable K^+ , Mg^{2+} and HCO_3^- .

Formation of Fe-Si-rich corrosion layers was found dependent on heating temperature up to 150 °C. The source of silica is regarded in the amorphous phases in bentonite. Theoretical models of corrosion

product formation (Gondolli et al. 2018) predict the formation of magnetite as the main corrosion product, as well as siderite and chukanovite as minor corrosion products in the early stages of environmental development. Greenalite, chamosite and Fe-illite should be present in the system according to the long-term models. Magnetite, chukanovite and siderite were confirmed in the experiments. This is in accordance with the expected model. Absence of silicate-based corrosion products is explained by short loading period (e.g., King et al. 2008; Stoullil et al. 2013).

2.8 Summary and conclusions of UJV testing

The steel samples embedded in the BCV bentonite heated up at 150 °C indicate lower corrosion rate when irradiated compared to unirradiated samples. Combination of 150 °C and irradiation led to the surface corrosion indicating almost constant corrosion rate for the whole testing period. Unirradiated samples heated up to 150 °C showed the highest corrosion rate after 6 months with decreasing tendency when the loading period was prolonged up to 18 months. The decreasing corrosion rate was observed in both irradiated and unirradiated steel samples heated up at 90 °C correlating with increasing loading period. Minimum corrosion rate was found in steel samples embedded in water saturated BCV bentonite stored under laboratory temperature without irradiation. Inhibiting effect of irradiation on steel corrosion was observed when the steel samples were embedded in MX80 bentonite heated up at 150 °C. Almost no effect of irradiation was observed when the MX80 bentonite was heated up at 90 °C.

Longer loading period led to the formation of higher amount of corrosion products facilitating their identification. Hematite and Fe-rich carbonates (chukanovite, siderite) were confirmed forming corrosion layers on the steel surface. The thickness of the corrosion layer varied, ranging from 10 to 45 µm, and was directly correlated with the duration of loading. Steel samples that remained unirradiated and were heated up at 90 °C exhibited corrosion layers up to 45 µm in thickness after 12 months of loading. In contrast, irradiation and thermal loading at 150 °C led to the formation of thinner corrosion layers, typically ranging from 10 to 20 µm. Corrosion layer composed of Fe-Si-O was identified on the surface of steel subjected to thermal loading of 150 °C. The layer was identified only by SEM-EDS indicating amorphous or poorly crystalline structure. The origin of Fe-Si-rich corrosion products needs to be confirmed by future research.

3. Corrosion tests performed by CIEMAT under gamma irradiation conditions

3.1 Overview

The corrosion of materials selected as canister for confining high-level radioactive waste in deep geological repositories (DGRs) has been extensively studied in the past under many relevant conditions (Abdelouas et al, 2022 and references there-in; Frankl et al. 2023). Canister corrosion will depend on the material characteristics and will be controlled by physico-chemical and specific environmental conditions established by the radioactive waste and by the other engineered and geological barriers, which will evolve over time (King and Padovani, 2011), including radiation, thermal, hydraulic, mechanical, chemical and biological processes, as well as external perturbations.

Past studies were mainly devoted to analyse the impact of different processes on container corrosion on an individual basis, but far fewer studies analysed corrosion considering the evolving coupled phenomena expected along the life of the repository. Amongst others, there are still uncertainties regarding the corrosion behaviour of the container materials within the early post-closure period.

Conceptually, four main evolution phases are identified at the canister / bentonite interface from the time of repository emplacement up to one million years (Landolt et al., 2009), considering the expected temperature, the bentonite water saturation degree and the established aerobic/anaerobic redox conditions:

- Phase 1 – Initial aerobic dry phase
- Phase 2 – Aerobic and unsaturated water hydration phase ()
- Phase 3 – Anaerobic unsaturated water hydration phase ()
- Phase 4 – Long-term cool, anoxic phase with fully water-saturated conditions.

In a repository, the radiation emitted by the radioactive waste itself is added to the temperature, redox, and water hydration degree, all expected to impact the canister corrosion and the clay barrier properties (Abdelouas et al, 2022 and references there-in).

The studies developed by CIEMAT (ES) for WP ConCorD - Task 3 aimed to investigate the impact of gamma radiation at the canister / bentonite barrier. Two main sets of experiments were carried out. (1) First experiments were designed to simulate, at laboratory scale, expected conditions at the canister / bentonite interface at the early stage of a DGR (Phase 2). (2) Second type of experiments was designed to analyse the evolution and impact of radiation on already released corrosion products at this interface.

A natural bentonite was selected to prepare compacted samples at different dry densities (1.4 and 1.6 g/cm³). Bentonite samples were pre-hydrated with corresponding pore water, at different water saturation degree (w.c. 60% or 100 %). In Phase 2, unsaturated water conditions are expected, but we considered as well fully water saturation degree (100 %) for comparison.

To analyse the impact of gamma irradiation accumulated dose on the container corrosion at the bentonite barrier, specific cells consisting of thin Cu-OFP or carbon steel coupons, simulating metal containers in waste repositories, placed over one surface of compacted bentonite samples, confined and closed, were prepared. These two metal materials were respectively supplied by the Swedish Nuclear Fuel and Waste Management Company (SKB) and the Swiss National Cooperative for the Disposal of Radioactive Waste (NAGRA) and are representative of different canister options being considered by many countries worldwide.

The second type of experiments simulated the canister / bentonite surface considering that oxides were already produced by steel or copper corrosion and were released to the bentonite surface. For the selection of oxides, it was considered that, in the initial stages of the repository, the oxidic corrosion consumes oxygen and can potentially buffer possible oxidant intrusions in the evolution of the system (Duro et al., 2012, Wersin and Kober, 2017, Fernández et al., 2018; Hadi et al., 2019). For this scenario, powder samples of selected copper and iron oxides were characterised before and after irradiation to

analyse the radiation impact. Moreover, compacted bentonite samples prepared with a thin layer of magnetite were irradiated under the same conditions to analyse their behaviour.

All CIEMAT samples simulating metal canister / bentonite interface were prepared in triplicate to consider (i) unirradiated conditions, (ii) gamma radiation at accumulated dose of 14 kGy and (iii) gamma radiation at accumulated dose of 140 kGy. Considering present repository designs (i.e. NAGRA), 14 kGy of accumulated dose is within the range of gamma radiation doses expected at the canister/bentonite interface in the early stage of the repository. The accumulated dose of 140 kGy was selected as ten times above the initial gamma radiation dose.

After irradiation, samples were characterised to evaluate metal corrosion rates, corrosion products presence and evolution and induced changes in bentonite. Main results obtained are here discussed.

Within ConCorD project Task 4, CIEMAT carried out complementary studies to analyse the impact of microbial activity in equivalent samples, under aerobic and anaerobic conditions, in collaboration with UGR (ES). Results are summarised in ConCorD Deliverable 15.9 (2024). The impact of higher temperatures and redox gradients, on equivalent metal/bentonite samples was analysed in Task 5, results summarised in ConCorD Deliverable 15.12 (2024).

3.2 Test specimens

3.2.1 Metal coupons

3.2.1.1 Carbon steel

The carbon steel (C-steel) material used by CIEMAT (ES) for obtaining the coupons for irradiation experiments is ASTM A694-08 F65 and was provided by Jacobs (UK). A circular sector of around 2 kg of C-steel (*Figure 45a*) came from a prototype representative of the canister material designed by the Swiss National Cooperative for the Disposal of Radioactive Waste (NAGRA) (Patel et al, 2012 ~~2024~~). This material was previously treated to represent the condition of the canister anticipated prior to disposal. At CIEMAT (ES), cylinder shaped tests of several diameters were extracted to further obtain thin flat coupons (*Figure 45b*), which were cut up with a lathe, adjusting the desired thickness by face turning, to be used for different purposes and experiments. The size of C-steel discs used for irradiation experiments were 1.9 cm in diameter and an average thickness of 1.5 mm (*Figure 45c*).

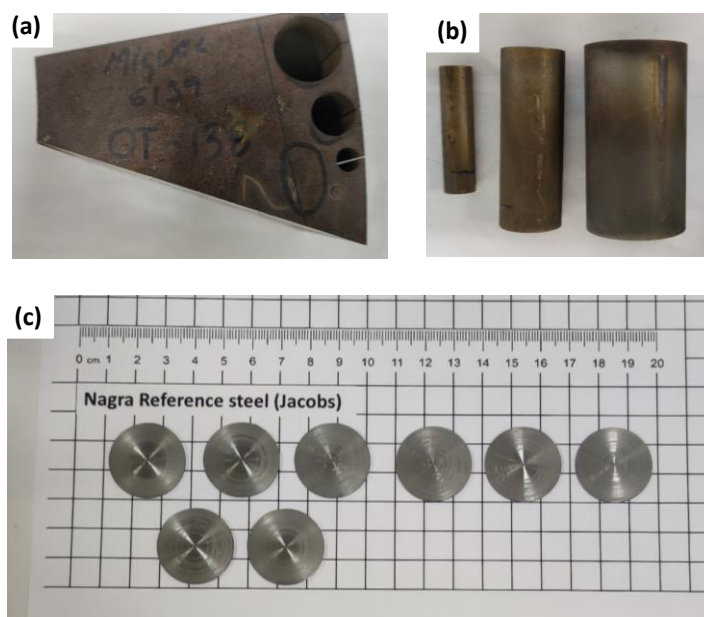


Figure 45 – (a) Carbon steel sample sent by Jacobs (UK) of material representative of canister design by NAGRA (CH). (b) Cylindrical test tubes extracted to obtain metal coupons of different diameter. (c) Carbon steel discs of 1.9 cm in diameter and 1.6 mm thickness used for irradiation experiments.

3.2.1.2 Copper

Copper samples were provided to CIEMAT by the Swedish Nuclear Fuel and Waste Management Company (SKB, SE). Different cylindrical tubes of oxygen-free phosphorus-doped copper (Cu-OFP) material were received by CIEMAT (ES). The rod used to obtain copper coupons is referred as T102 190° -224° (Figure 46a). Coupons were obtained by cutting up with a lathe, adjusting the desired thickness by face turning. The coupons had a diameter of 1.9 cm and average thickness of 1.5 mm (Figure 46b). The composition of the Cu-OFP material was included in Table 16. It was composed of Cu 99.99 % with small traces of other elements.

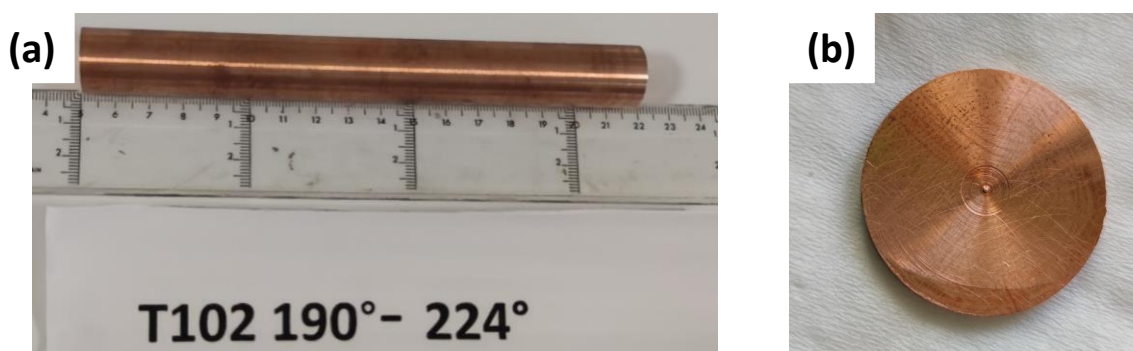


Figure 46 – (a) Cylindrical test tube reference T102 190°-224° of Cu-OFP, representative material of their canister design of SKB (SE) sent to CIEMAT (ES). (b) Example of Cu-OFP coupons of 1.9 cm in diameter and 1.6 mm thickness cut for irradiation experiments.

Table 16 – Composition of Cu-OFP sample reference T102 190° -224° provided by SKB (SE). Traces concentration indicated in part per million (ppm).

Cu	Traces (ppm)										
	Ag	Al	As	Bi	Cd	Co	Cr	Fe	H	Mn	Ni
99.99%	15.1	0.1	0.4	0.7	<0.3	0.35	0.3	0.4	0.5	<0.1	0.6
	O	P	Pb	S	Sb	Se	Si	Sn	Te	Zn	Zr
	1.9	58.3	1.7	4.6	1.3	<0.6	1.3	0.9	<2.7	<1.1	<0.1

3.2.2 Metal cleaning procedure

Before use, all metal samples were cleaned following this procedure: Metal coupons were first degreased in a ultrasonics bath for 5 min in a vial containing ethanol of analytical grade. Afterwards, samples were cleaned with Type I deionised water and swilled to remove any residual ethanol. Coupons were immersed in another vial containing ~ 1·10⁻³ M nitric acid and subjected to 5 min of sonication. This procedure was repeated three times. Coupons were dried with N₂ gas and stored in closed glass vessels.

This cleaning procedure was also applied after samples disassembling, to remove corrosion and degradation products over the metal surfaces, to estimate corrosion rates by mass loss weighting, following ASTM main recommendations (ASTM, 2011 1999).

3.2.3 Selected iron and copper oxides

A review on typical corrosion products usually formed from C-steel and copper materials in environments representative of deep geological repositories, considering oxic and anoxic environments, ambient or high temperature, radiation, pore water chemistry, etc, was carried out at the beginning of the project (EURAD Milestone MS264, 2021).

In the case of copper, the expected corrosion products at reducing or oxidizing conditions are Cu(I) and Cu(II) oxides, respectively.

Oxide films formed on metallic iron after corrosion are composed of magnetite and hematite (Little and Lee, 2007). Ferric oxyhydroxides, which can later crystallize to maghemite (γ-Fe₂O₃) and hematite (α-Fe₂O₃). Fe(III)/Fe(II)-containing magnetite (Fe₃O₄) may be also present (i.e. Saheb et al., 2014).

Under oxic conditions, aerobic corrosion leads to the formation of Fe(III)-rich or Cu(II) corrosion products, while under anoxic conditions Fe(II) and Cu(I) phases are expected.

Selected powder oxides for irradiation studies included Cu and Fe oxides in different both oxidation states are shown in *Figure 47*:

- CuO: Copper (II) oxide nanopowder < 50 nm (purchased in Sigma Aldrich).
- Cu₂O: Copper (I) oxide > 99.99 % trace metal basis (purchased in Thermo Scientific™).
- Fe₂O₃: Fe(III) oxide nanopowder <50 nm particle size (purchased in Sigma Aldrich)
- Fe₃O₄: Fe(II, III) oxide nanopowder 50-100 nm particle size (SEM), 97% trace metals basis (purchased in Sigma Aldrich).
- α-FeOOH: Fe(III) oxide, goethite laboratory prepared as described in (Missana et al. 2009).



Figure 47 – Selected corrosion products. From Left to Right: Fe_2O_3 , Fe_3O_4 , Cu_2O and CuO commercial nano-powder oxides.

Cu_2O and Fe_3O_4 oxides were preserved in an anoxic chamber under N_2 atmosphere to avoid oxidation. Powder samples were fully characterised before and after irradiation to analyse their main characteristics, mainly oxide phase, particle size, and surface properties.

3.2.4 Bentonite

FEBEX bentonite, from the Cortijo de Archidona deposit (Almería) was selected. This clay takes the name from the FEBEX (*Full-scale Engineered Barriers Experiment*) project (Huertas et al., 2000). FEBEX has a montmorillonite content greater than 90 %, with quartz, plagioclase, potassic feldspar, calcite and trydimite as accessory minerals. There may be illite/smectite interstratifications up to 15 %. The cation exchange capacity is 100 meq/100g, and in the exchange complex 42 % Ca, 33 % Mg, 23 % Na and 2 % K are present.

For the ConCorD project, 2.5 kg of bentonite from the batch referenced as FEBEX 70-IMA-3-4-0 (Huertas et al, 2000) were separated. Prior to compaction, the FEBEX clay was ground and sieved to a fraction < 0.5 mm (Figure 48). Raw FEBEX clay was used in these experiments without any additional treatment or purification.

Complete mineralogical, physical, chemical and microbial characterisation of this clay was carried out before and after experiments.



Figure 48 – (a) Powder FEBEX bentonite grounded and sieved to a fraction < 0.5 mm. (b) Example of compacted bentonite sample hydrated with porewater at desired saturation degree.

3.2.5 Bentonite porewater

The water used to saturate the compacted bentonite samples were the respective FEBEX pore waters, corresponding to each compaction density (1.4 and 1.6 g/cm^3), respectively named PW-1.4 and PW-1.6. These synthetic waters were prepared following the recipes proposed in (Fernandez & Rivas, 2005).

The salt content required for the preparation of pore water characteristic of each dry density are included in Table 17.

For verification, aliquots of both waters were sent to the Chemical Division of CIEMAT for complete chemical analysis. The elemental compositions of initial recipes were confirmed.

Table 17 – Chemical composition (M) of synthetic pore waters respectively prepared for FEBEX bentonite samples compacted at 1.4 (PW-1.4) and 1.6 g/cm³ (PW-1.6). Recipes from (Fernandez & Rivas, 2005).

Reference Density	KCl (M)	CaCl ₂ ·2H ₂ O (M)	MgCl ₂ ·6H ₂ O (M)	Na ₂ SO ₄ (M)	NaCl (M)	NaHCO ₃ (M)	pH
PW-1.4	1.01·10 ⁻³	1.36·10 ⁻²	1.48·10 ⁻²	4.87·10 ⁻²	5.79·10 ⁻³	1.10·10 ⁻³	7.56
PW-1.6	1.09·10 ⁻³	1.50·10 ⁻²	1.66·10 ⁻²	4.59·10 ⁻²	2.16·10 ⁻²	1.01·10 ⁻³	7.55

3.3 Experimental set-ups

3.3.1 Set-up to analyse powder materials: unirradiated and gamma irradiated

Reference powder samples of FEBEX bentonite and selected iron and copper oxides (described in Section 3.2.3) (Table 18) representative of corrosion products were separately placed in high-density polyethylene (HDPE) tubes, without any additional preparation (Figure 49), to be subjected to gamma irradiation under the same conditions applied for samples simulating canister /bentonite interface.

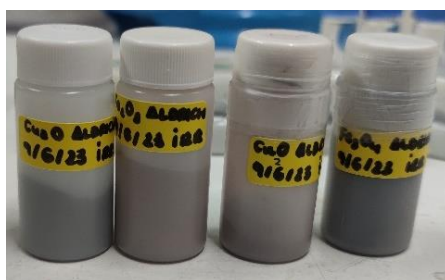


Figure 49 – Selected corrosion products, powder oxides in high-density polyethylene tubes for irradiation experiments.

Table 18 – Nature and conditions of selected powder materials that were characterised under three conditions: (i) unirradiated, (ii) gamma irradiated at accumulated dose of 14 kGy and (iii) gamma irradiated at accumulated dose of 140 kGy.

REFERENCE POWDER SAMPLES				
Reference	Material	Type of reactor / device	Temperature	Redox conditions
Ref-FEBEX	Powder FEBEX bentonite	HDPE tube	ambient	aerobic
Ref-CuO	Powder CuO	HDPE tube	ambient	aerobic
Ref-Cu ₂ O	Powder Cu ₂ O	HDPE tube	ambient	aerobic
Ref-Hematite	Powder Fe ₂ O ₃	HDPE tube	ambient	aerobic
Ref- Magnetite	Powder Fe ₃ O ₄	HDPE tube	ambient	aerobic
Ref- Goethite	Powder α -FeOOH:	HDPE tube	ambient	aerobic

These samples were analysed as reference to independently detect relevant structural or physico-chemical changes in the materials induced by gamma - radiation that are not exclusive or not attributable to specific environmental conditions at the canister/bentonite interface.

The integrity of the HDPE tubes after irradiation was verified by RAMAN spectroscopy.

3.3.2 Set-up to analyse metal corrosion in water: unirradiated and gamma irradiated

Triplicate sets of six different samples were prepared with Cu-OFP and C-steel metal coupons separately introduced in polypropylene isotactic tubes where 5 mL of different waters were added (Figure 50) FEBEX bentonite porewater representative of 1.4 g/cm³ compaction density (PW-1.4), FEBEX bentonite porewater representative of 1.6 g/cm³ compaction density (PW-1.6) and deionised water (DW). The composition of selected waters was presented in Table 8.

Samples were prepared in triplicate to account for three gamma-irradiation conditions: (1) unirradiated, (2) irradiated at 14 kGy and (3) irradiated at 140 kGy gamma-accumulated doses.

Table 19 presents the list of these 18 metal samples immersed in water their experimental characteristics: The type of sample according to the irradiation, the reference, the type of metal coupon, the bentonite type and compaction dry density (none in this case), the type of added water (Table 8), the saturation conditions and added volume, the redox conditions, temperature and type of device used for irradiation.



Figure 50 – Samples of different metal coupons immersed in 5 mL of different bentonite porewater (PW-1.4, PW-1.6, composition in Table 8) or deionised water (DW) prepared in isotactic polypropylene tubes.

Table 19 – List of metal samples immersed in waters for irradiation. The table includes the type of sample according to the gamma radiation dose, the reference, the type of metal coupon or oxide, the bentonite type and compaction dry density (none in this case), the type of added water (Table 8), the saturation conditions and added volume, the redox conditions, temperature and type of device used for irradiation.

METAL SAMPLES IMMersed IN WATER										
Type of sample / Radiation dose	Reference	Metal /oxide	Bentonite	Density	Hydration water	Water saturation conditions	Water Volume (mL)	Redox	Temperature	Type of reactor / device
Unirradiated	T3-19*	Cu-OFP	none	none	PW-1.4	immersion	5	aerobic	ambient	polypropylene tube
	T3-20*	Cu-OFP	none	none	PW-1.6	immersion	5	aerobic	ambient	polypropylene tube
	T3-21*	C-steel	none	none	PW-1.4	immersion	5	aerobic	ambient	polypropylene tube
	T3-22*	C-steel	none	none	PW-1.6	immersion	5	aerobic	ambient	polypropylene tube
	T3-23*	Cu-OFP	none	none	DW	immersion	5	aerobic	ambient	polypropylene tube
	T3-24*	Cu-OFP	none	none	DW	immersion	5	aerobic	ambient	polypropylene tube
Gamma Irradiated 14 kGy (dose rate 66 Gy/h)	T3-19	Cu-OFP	none	none	PW-1.4	immersion	5	aerobic	ambient	polypropylene tube
	T3-20	Cu-OFP	none	none	PW-1.6	immersion	5	aerobic	ambient	polypropylene tube
	T3-21	C-steel	none	none	PW-1.4	immersion	5	aerobic	ambient	polypropylene tube
	T3-22	C-steel	none	none	PW-1.6	immersion	5	aerobic	ambient	polypropylene tube
	T3-23	Cu-OFP	none	none	DW	immersion	5	aerobic	ambient	polypropylene tube
	T3-24	Cu-OFP	none	none	DW	immersion	5	aerobic	ambient	polypropylene tube
Gamma Irradiated 140 kGy (dose rate 697 Gy/h)	T3-33	Cu-OFP	none	none	PW-1.4	immersion	5	aerobic	ambient	polypropylene tube
	T3-34	Cu-OFP	none	none	PW-1.6	immersion	5	aerobic	ambient	polypropylene tube
	T3-35	C-steel	none	none	PW-1.4	immersion	5	aerobic	ambient	polypropylene tube
	T3-36	C-steel	none	none	PW-1.6	immersion	5	aerobic	ambient	polypropylene tube
	T3-37	Cu-OFP	none	none	DW	immersion	5	aerobic	ambient	polypropylene tube
	T3-38	Cu-OFP	none	none	DW	immersion	5	aerobic	ambient	polypropylene tube

* unirradiated

3.3.3 Metal coupons / bentonite samples

The pieces, materials and installation procedure of the closed cells designed for samples simulating metal canister/bentonite interface at different experimental conditions are shown in *Figure 51*:

Closed cell (*Figure 51a*) is made of a vinyl polychloride (PVC) open cylinder with an external thread in which a plastic disc is placed at the bottom to act as a lid (a). (*Figure 51b*) A cylindrical bentonite sample of 1.9 cm in diameter and 1 cm thickness is compacted to the desired density and hydrated with the required water to achieve the degree of saturation (60 or 100%). (*Figure 51c*) The bentonite tablet is inserted in the PVC ring (*Figure 51d*) and the metal disc is placed over the clay tablet (*Figure 51e*). Finally, the entire cell is assembled by closing with two Delrin® caps which provide the required confinement (*Figure 51f*). The integrity of cell components upon irradiation was checked after disassembling by visual inspection and by comparing RAMAN spectra before and after irradiation. No degradation was appreciated at sight.

The compacted bentonite sample dimensions, the amount of bentonite clay weighted for each compaction density (1.4 g/cm^3 or 1.6 g/cm^3) and the added water to achieve the desired degree of saturation (w.c. in %) are indicated in *Table 20*. The average clay mass of 1.4 g/cm^3 samples was 4.5 g and 5.1 g for 1.6 g/cm^3 . The water content at is 0.8 mL at 1.4 g/cm^3 and 60 % saturation, 1.4 mL at 1.4 g/cm^3 and 100 % saturation, 0.7 mL at 1.6 g/cm^3 and 60 % saturation, 1.2 mL at 1.6 g/cm^3 and 100 % saturation. Porewater corresponding to its density was added to each compacted sample (*Table 8*).

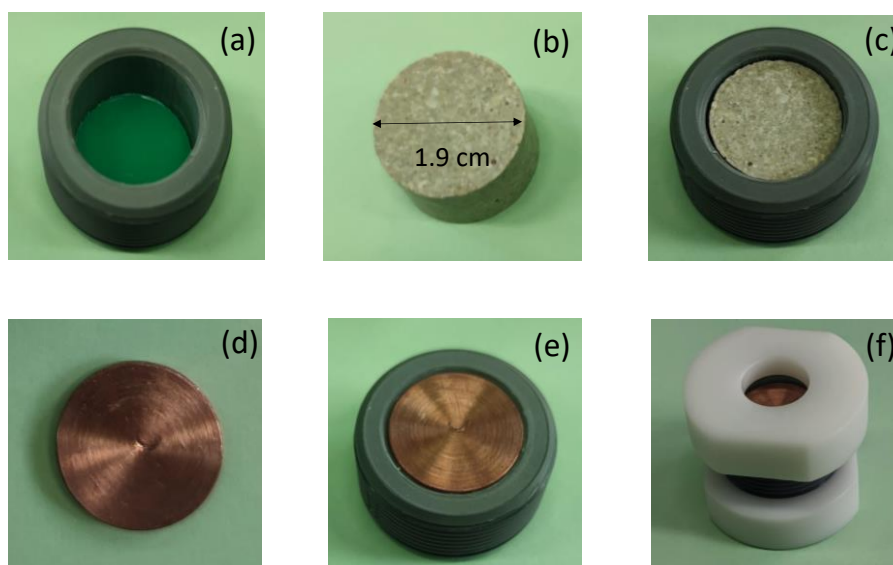


Figure 51 – Closed cell designed for samples simulating metal canister/bentonite interface: (a) PVC open cylinder, (b) compacted bentonite sample. (c) bentonite inserted in the PVC ring, (d) copper metal disc (e) copper disc placed on the surface of the clay tablet, (f) closed cell.

As shown in *Figure 52*, sixteen different samples were basically prepared with bentonite at different compaction densities (1.4 or 1.6 g/cm^3), hydrated at two saturation degrees (60 % and 100%), four without any metal (reference irradiated clay), four with copper coupons, other four with carbon- steel and additional four with magnetite. Most of them were prepared in triplicate to account for three gamma-irradiation conditions: (1) unirradiated (*Table 21*) (2) gamma-irradiated at 14 kGy with a dose of 66 Gy/h (*Table 22*) and (3) gamma- irradiated at 140 kGy with a dose of 697 Gy/h (*Table 23*). Not all samples were irradiated at higher doses.

Table 20 – Dimensions and characteristics of compacted bentonite samples prepared at different compaction densities, with different water saturation degree (w.c. in %).

Compacted bentonite samples	1.4 g/cm ³ w.c. 60 %	1.4 g/cm ³ w.c. 100 %	1.6 g/cm ³ w.c. 60 %	1.6 g/cm ³ w.c. 100 %
Diameter (cm)	0.95	0.95	0.95	0.95
Thickness (cm)	1	1	1	1
Compaction density (g/cm ³)	1.4	1.4	1.6	1.6
Clay initial humidity (%)	13	13	13	13
Weighed clay (g)	4.5	4.5	5.1	5.1
Clay specific weight (g/cm ³)	2.7	2.7	2.7	2.7
Desired saturation degree (%)	60	100	60	100
Necessary water for saturation (mL)	0.8	1.4	0.7	1.2
Initial water (humidity) (mL)	0.5	0.5	0.6	0.6
Added Porewater (mL)	0.3	0.9	0.1	0.6

3.3.1 Set up to analyse magnetite / bentonite samples: unirradiated and gamma irradiated

Compacted bentonite samples with a thin surface layer (1-2 mm) of magnetite (Fe₃O₄) were prepared to analyse the impact of irradiation on released corrosion products.

The same closed cell shown in *Figure 51* was used for this experiment, but the metal coupon (*Figure 51d & e*) was substituted by a thin layer of powder magnetite, described in (*Figure 51*) (*Figure 52*). Eight different cells were prepared with bentonite compacted at two densities and saturated at two degrees, four of them were not irradiated to be used as reference (samples referenced T3-13* to T3-16* in *Table 21*) and other four were gamma-irradiated with an accumulated dose of 14 kGy (samples referenced T3-13 to T3-16 in *Table 22*). After irradiation samples were dismantled to evaluate changes on magnetite physico-chemical characteristics and induced degradation in the compacted bentonite samples.



Figure 52 – Picture of sixteen closed cells installed with copper and carbon steel metal coupons, or magnetite oxide, placed over one surface of compacted bentonite samples, at different conditions (*Table 22*) prepared for gamma radiation experiments under aerobic conditions.

Table 21 – List of metal / bentonite samples prepared as reference unirradiated. The table includes the type of sample according to received radiation, the reference, the type of metal coupon or oxide included, the bentonite type and compaction dry density, the type of added water (Table 8), the saturation degree and water volume, the redox conditions, temperature and type of device used for irradiation.

METAL COUPONS / BENTONITE SAMPLES										
Type of sample	Reference	Metal /oxide	Bentonite	Density	Hydration water	Water saturation conditions	Water Volume (mL)	Redox	Temperature	Type of reactor / device
Unirradiated	T3-01*	none	FEBEX	1.4	PW-1.4	60%	0.8	aerobic	ambient	Closed cell
	T3-02*	none	FEBEX	1.4	PW-1.4	100%	1.4	aerobic	ambient	Closed cell
	T3-03*	none	FEBEX	1.6	PW-1.6	60%	0.7	aerobic	ambient	Closed cell
	T3-04*	none	FEBEX	1.6	PW-1.6	100%	1.2	aerobic	ambient	Closed cell
	T3-05*	Cu	FEBEX	1.4	PW-1.4	60%	0.8	aerobic	ambient	Closed cell
	T3-06*	Cu	FEBEX	1.4	PW-1.4	100%	1.4	aerobic	ambient	Closed cell
	T3-07*	Cu	FEBEX	1.6	PW-1.6	60%	0.7	aerobic	ambient	Closed cell
	T3-08*	Cu	FEBEX	1.6	PW-1.6	100%	1.2	aerobic	ambient	Closed cell
	T3-09*	C-steel	FEBEX	1.4	PW-1.4	60%	0.8	aerobic	ambient	Closed cell
	T3-10*	C-steel	FEBEX	1.4	PW-1.4	100%	1.4	aerobic	ambient	Closed cell
	T3-11*	C-steel	FEBEX	1.6	PW-1.6	60%	0.7	aerobic	ambient	Closed cell
	T3-12*	C-steel	FEBEX	1.6	PW-1.6	100%	1.2	aerobic	ambient	Closed cell
	T3-13*	<i>magnetite</i>	FEBEX	1.4	PW-1.4	60%	0.8	aerobic	ambient	Closed cell
	T3-14*	<i>magnetite</i>	FEBEX	1.4	PW-1.4	100%	1.4	aerobic	ambient	Closed cell
	T315*	<i>magnetite</i>	FEBEX	1.6	PW-1.6	60%	0.7	aerobic	ambient	Closed cell
	T3-16*	<i>magnetite</i>	FEBEX	1.4	PW-1.6	100%	1.2	aerobic	ambient	Closed cell

* unirradiated

Table 22 – List of metal / bentonite samples prepared for gamma-irradiation at 14 kGy. The table includes the type of sample according to received radiation, the reference, the type of metal coupon or oxide included, the bentonite type and compaction dry density, the type of added water (Table 8), the saturation degree and water volume, the redox conditions, temperature and type of device used for irradiation.

METAL COUPONS / BENTONITE SAMPLES										
Type of sample	Reference	Metal /oxide	Bentonite	Density	Hydration water	Water saturation conditions	Water Volume (mL)	Redox	Temperature	Type of reactor / device
Gamma Irradiated 14 kGy (dose rate 66 Gy/h)	T3-01	none	FEBEX	1.4	PW-1.4	60%	0.8	aerobic	ambient	closed cell
	T3-02	none	FEBEX	1.4	PW-1.4	100%	1.4	aerobic	ambient	closed cell
	T3-03	none	FEBEX	1.6	PW-1.6	60%	0.7	aerobic	ambient	closed cell
	T3-04	none	FEBEX	1.6	PW-1.6	100%	1.2	aerobic	ambient	closed cell
	T3-05	Cu-OFP	FEBEX	1.4	PW-1.4	60%	0.8	aerobic	ambient	closed cell
	T3-06	Cu-OFP	FEBEX	1.4	PW-1.4	100%	1.4	aerobic	ambient	closed cell
	T3-07	Cu-OFP	FEBEX	1.6	PW-1.6	60%	0.7	aerobic	ambient	closed cell
	T3-08	Cu-OFP	FEBEX	1.6	PW-1.6	100%	1.2	aerobic	ambient	closed cell
	T3-09	C-steel	FEBEX	1.4	PW-1.4	60%	0.8	aerobic	ambient	closed cell
	T3-10	C-steel	FEBEX	1.4	PW-1.4	100%	1.4	aerobic	ambient	closed cell
	T3-11	C-steel	FEBEX	1.6	PW-1.6	60%	0.7	aerobic	ambient	closed cell
	T3-12	C-steel	FEBEX	1.6	PW-1.6	100%	1.2	aerobic	ambient	closed cell
	T3-13	<i>magnetite</i>	FEBEX	1.4	PW-1.4	60%	0.8	aerobic	ambient	closed cell
	T3-14	<i>magnetite</i>	FEBEX	1.4	PW-1.4	100%	1.4	aerobic	ambient	closed cell
	T315	<i>magnetite</i>	FEBEX	1.6	PW-1.6	60%	0.7	aerobic	ambient	closed cell
	T3-16	<i>magnetite</i>	FEBEX	1.4	PW-1.6	100%	1.2	aerobic	ambient	closed cell

Table 23 – List of metal / bentonite samples prepared for gamma-irradiation at 140 kGy. The table includes the type of sample according to received radiation, the reference, the type of metal coupon or oxide included, the bentonite type and compaction dry density, the type of added water (Table 8), the saturation degree and water volume, the redox conditions, temperature and type of device used for irradiation.

METAL COUPONS / BENTONITE SAMPLES										
Type of sample	Reference	Metal /oxide	Bentonite	Density	Hydration water	Water saturation conditions	Water Volume (mL)	Redox	Temperature	Type of reactor / device
Gamma Irradiated 140 kGy (dose rate 697 Gy/h)	T3-25	Cu-OFP	FEBEX	1.4	PW-1.4	60%	0.8	aerobic	ambient	closed cell
	T3-26	Cu-OFP	FEBEX	1.4	PW-1.4	100%	1.4	aerobic	ambient	closed cell
	T3-27	Cu-OFP	FEBEX	1.6	PW-1.6	60%	0.7	aerobic	ambient	closed cell
	T3-28	Cu-OFP	FEBEX	1.6	PW-1.6	100%	1.2	aerobic	ambient	closed cell
	T3-29	C-steel	FEBEX	1.4	PW-1.4	60%	0.8	aerobic	ambient	closed cell
	T3-30	C-steel	FEBEX	1.4	PW-1.4	100%	1.4	aerobic	ambient	closed cell
	T3-31	C-steel	FEBEX	1.6	PW-1.6	60%	0.7	aerobic	ambient	closed cell
	T3-32	C-steel	FEBEX	1.6	PW-1.6	100%	1.2	aerobic	ambient	closed cell

3.4 Irradiation conditions

Different irradiation shifts were carried out by CIEMAT along ConCorD project duration to achieve the different objectives. Before irradiation, samples were introduced in a watertight metal container equipped to be introduced at a depth of 4 m into the irradiation pool facility, to be placed in the compartments (Figure 53a) containing the necessary ^{60}Co sources to achieve desired accumulated dose.

Samples were irradiated at the Nayade installation available at CIEMAT (Figure 53b). The Nayade facility is pool-type (1.2 m wide by 4.5 m deep) that uses water as shield, allowing direct vision for positioning the sources and extracting of samples. The irradiation facility includes 12 ^{60}Co cylindrical sources (15 mm diam. x 135 mm long) distributed in a circle. Two configurations are available: High flux; $\leq 8.3 \times 10^3$ Gy/h within a 60mm diam. x 100 mm high volume and Low flux; $\leq 1.2 \times 10^2$ Gy/h within a 200 mm diam. x 100 mm high volume (in the low flux configuration the sources can be rotated along an outer circle for uniform dose).

In each irradiation round, a preliminary study was carried out to determine how many ^{60}Co sources and how much time was necessary to reach the required emitted and cumulative gamma doses. In CIEMAT experiments for Task 3, two radiation conditions were mainly applied: (1) Cumulative gamma dose of 14 kGy, with dose rate of 66 Gy/h and (2) cumulative dose of 140 kGy, with dose rate of 697 kGy/h. The time of irradiation was equivalent in all cases.

Dosimetry was performed with vial normal Fricke dosimeters, ensuring dose uniformity in all samples.

After irradiation, samples were introduced inside an anaerobic jar under N_2 atmosphere and transferred to the different laboratories for analyses.

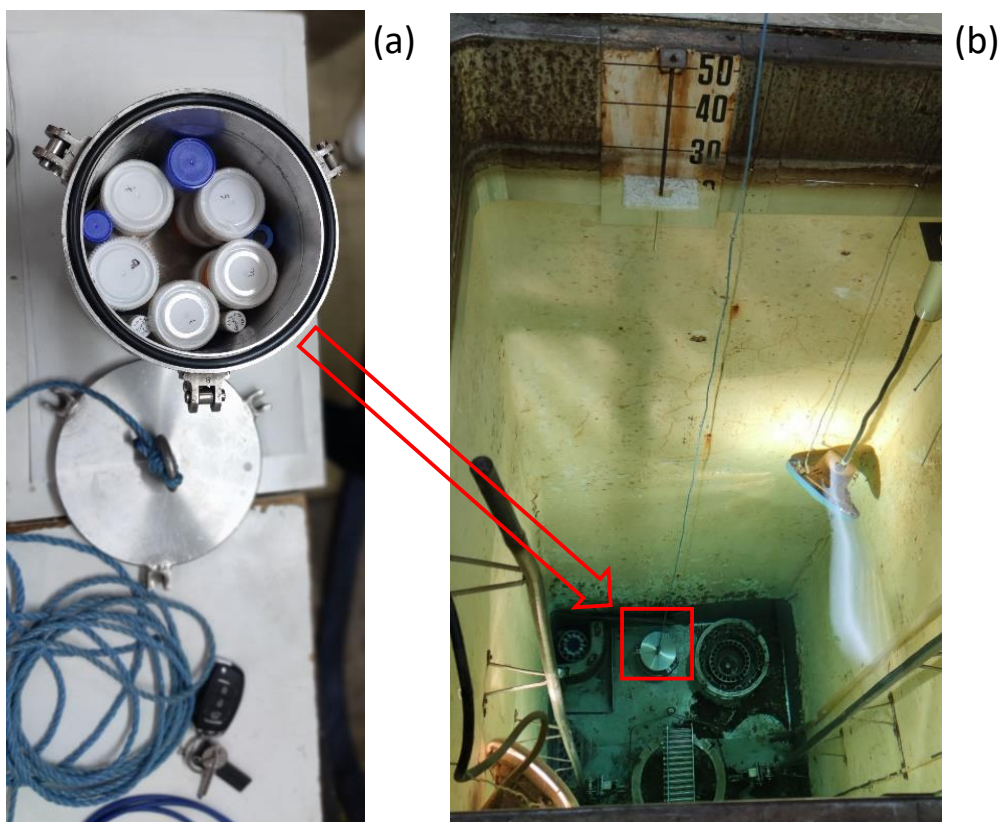


Figure 53 – (a) Samples introduced in a watertight metal container equipped to be introduced at a depth of 4 m into the irradiation pool facility to be placed in the circular compartments containing the ^{60}Co sources. (b). Samples inside CIEMAT's Nayade ^{60}Co gamma irradiation pool facility.

3.5 Disassembly and post-test analyses

Powder materials (*Figure 47; Table 18*) were analysed before and after irradiation at 14 kGy or 140 kGy to determine phase changes. Additional experiments are being carried out to evaluate induced changes on surface characteristics that may be relevant for radionuclide retention, out of the scope of ConCorD project.

In the case of metals that were immersed in selected waters, the performed analyses after irradiation included the evaluation of metal corrosion by different techniques and the quantification of dissolved Cu or Fe in the aqueous phase.

For the samples simulating the canister /bentonite interface, main analyses were focused in Task 3 on determining the corrosion rates by mass loss, the identification of the main corrosion products, and also on bentonite analyses.

3.5.1 Disassembly and visual inspection

The disassembling and sampling procedure were adapted to the type of samples and experiments.

3.5.1.1 Powder samples

Powder samples were directly sampled in the test tubes and were separated into fractions, of different quantities, for each type of analysis focused at present on detecting phase changes.

3.5.1.2 Metal disc immersed in water

Metal discs were extracted from the water and photographed to visually compare their degradation. When appreciable alteration was detected on the disc surface, the altered surface layer was carefully retrieved with a spatula and stored for analyses. Metal samples were cleaned a few times with the same procedure described in section 3.2.2, to eliminate degradation products, following standard practices (ASTM, 1999). After cleaning, samples were weighed to estimate corrosion rate by mass loss.

Aliquots of the contact water were sampled to determine the dissolved Fe or Cu, by chemical analysis.

3.5.1.3 Metal /bentonite samples

The procedure for disassembling samples simulating the metal canister/bentonite interface required additional care. Photographs were taken of the samples through the procedure to better evaluate induced changes or damage.

Figure 54 shows a cell opening, showing that the size of the metal disc not contacting the bentonite surface looks like unaltered (*Figure 54a*). In some cases, the sample extraction required the use of the same press used to compact the bentonite samples. After sample extraction from the PVC ring, the metal discs were usually stuck to the surface of the hydrated bentonite (*Figure 54b*) and were carefully separated from the clay with tweezers. Once metal and bentonite surfaces are separated (*Figure 54c*), the alteration and degradation products (mixture of corrosion products and bentonite phases or salts) can be seen over both surfaces.

First attempt aimed to analyse these degradation products directly on the metal or clay surfaces, by applying non-destructive characterization techniques.

The degraded / corroded surface layers were then carefully retrieved from the metal samples with a spatula and stored for further analyses.

Metal samples were cleaned a few times with the same procedure described in section 3.2.2 to eliminate degradation products. After cleaning, samples were weighed to estimate corrosion rate by mass loss measurements..

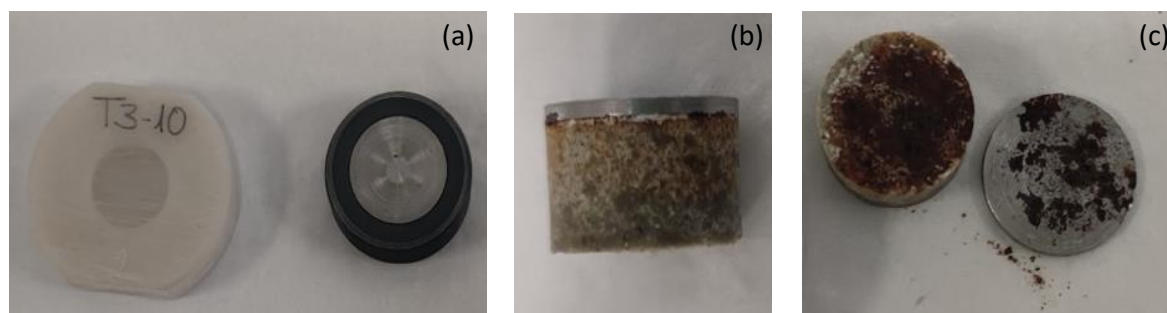


Figure 54 – Picture of disassembling of a closed cell containing a sample simulating metal canister / bentonite interface after irradiation.

3.5.2 Water analyses

The different waters in which metal discs were immersed and subjected to irradiation were sampled to analyse the Fe and Cu content. Prior to analyses some samples were filtered by 0.2 μm and sent as well for analyses, to evaluate if Cu and Fe are present as particles or dissolved. Samples were acidified with 1 N HNO_3 to be analysed by Inductively Coupled Plasma Optical Emission spectroscopy (ICP-OES) with a VARIAN 735 ES equipment at the Chemistry Division of CIEMAT.

3.5.3 Mass loss measurements

To calculate the average corrosion rate of the specimens, the mass loss measurements were conducted.

All metal discs were weighed (initial mass) and measured with calibre (diameter and thickness) prior to assembly. After dismantling, the metal discs were cleaned with the same procedure used for cleaning the specimens prior to installation (section 3.2.2) following ASTM recommendations (ASTM, 1999). After cleaning the metal disc were reweighed. This procedure was repeated until the weighed mass was the same, measured with two different high precision balances (average final mass).

The mass loss due to corrosion of the metal coupons was calculated by difference between the initial mass and the average final mass. The contact times considered to calculate corrosion rates, 12 days (288 h), includes the time from preparation to radiation exposure, the radiation exposure (approximately 200 h) and the time for disassembly. The average densities considered for Cu-OFP and C-steel samples were 8.96 and 7.86 g/cm^3 respectively, typical values for these materials. Bentonite, oxides alteration and degradation products

All powder and compacted samples were characterised, with different techniques, before and after irradiation to identify relevant changes induced by studied coupled processes and the nature of degradation and corrosion products.

3.5.3.1 X-ray diffraction (XRD)

XRD patterns were obtained from random powders in order to identify the mineralogical species. The powders were analysed with a Philips X'Pert –PRO MPD diffractometer, using an anticathode Cu-K α at 45 kV and 40 mA, equipped with a fixed divergence slit (0.1245° size), Scientific X'celerator detector. The samples were investigated from 2° to 70° 2 θ with a step size 0.017° 2 θ , and a scan rate of 50 s per step for the powder samples. The XRD database used for mineral identification has been the Power Diffraction File from the International Center for Diffraction Data (ICDD).

3.5.3.2 Fourier transform IR spectra (FT-IR)

To detect structural changes, Fourier transform IR (FT-IR) spectra were obtained on powder samples by transmission in the mid-IR region ($4000-400\text{ cm}^{-1}$), using a Nicolet Is50 with a DTGS KBr detector (resolution 4 cm^{-1} , 32 scans) and atmospheric CO_2 . Two milligrams of powder air-dried samples were dispersed in 200 mg of KBr and pressed to a clear disc. The pressed samples were analysed at room temperature after heating in an oven overnight at $110\text{ }^\circ\text{C}$. The spectra were examined in the OH stretching region ($3400-3800\text{ cm}^{-1}$) and below 1200 cm^{-1} . Spectra were analysed with OMNIC software.

3.5.3.3 Scanning electron microscopy (SEM).

A ZEISS EVO LS 15 SEM microscope coupled to a X LINK LZ_5 energy dispersive X-ray energy spectrometer (XEDS) was used to identify possible alteration products.

3.5.3.4 RAMAN spectroscopy

Raman spectra were obtained with a Thermo Scientific DXR3 Smart Raman spectrometer. The high-power laser mainly used was of 532 nm , in the spectral range of $1800-50\text{ cm}^{-1}$.

3.5.3.5 Surface characteristics

Different techniques were used to analyse the impact of gamma radiation on surface characteristics of oxide and bentonite particles.

Zeta potential measurements (Hunter, 2013) were performed with a Zeta Master Malvern equipment in suspensions of irradiated and unirradiated Cu and Fe oxides and on bentonite as a function of pH.

To assess changes in the surface electrical charge, pHpzc is determined in both samples by electrolyte titration [4]. Finally, potentiometric titrations were carried out in the glovebox chamber. Potentiometric acid-base titrations are commonly used to determine acidity constants and concentration of weak hydroxyl surface sites on the solid surfaces (Schulthess & Sparks. 1986).

3.6 Results by CIEMAT

3.6.1 Irradiated powder materials

3.6.1.1 Fe and Cu oxides

Figure 55 shows X-ray diffraction (XRD) patterns obtained on unirradiated and irradiated powder samples at 14 kGy and 140 kGy, for comparison. The XRD patterns measured on unirradiated samples confirmed the phase of all selected oxides: CuO, Cu₂O, Fe₂O₃, Fe₃O₄ and α -FeOOH. Moreover, the same XRD patterns were measured after exposure to gamma-radiation at 66 Gy/h with a cumulative dose of 14 kGy, which indicate that the oxide structure of all analysed Cu(I), Cu(II), Fe(II) and Fe(III) remained stable, unaltered by radiation. This stability upon the exposure to gamma radiation doses was also confirmed by FT-IR and RAMAN spectroscopies, since no appreciable changes were appreciated in any of the irradiated oxide samples.

The surface characterisations of irradiated oxides were conducted post irradiation and compared to that of unirradiated oxides. As mentioned, the analyses included zeta potential measurements to evaluate the surface electrostatic charge, the point of zero charge and potentiometric titrations.

Some differences on zeta potential measurements were detected on the oxides irradiated at 14 kGy (dose rate 66 Gy/h) or 140 kGy (dose rate 697 Gy/h), mainly displacement of point of zero charge and some variations on the magnitude, but the analyses deserve further confirmation by other methodologies. The observed differences may have an impact of the irradiated oxides retention capability towards different radionuclides, and this aspect deserves future studies.

3.6.1.2 Irradiated FEBEX bentonite

Figure 55 shows the comparison of X-ray diffraction patterns obtained on unirradiated and irradiated powder FEBEX bentonite at 14 kGy and 140 kGy. As well as in the case of irradiated powder oxides, the XRD patterns did not suggest any change on the bentonite mineralogy.

The comparison of FTIR spectra (Figure 56) shows the main bands associated to di-octahedral smectites like FEBEX as well as their corresponding group, neither showed any structural change due to radiation. This indicated that the bentonite is very stable upon the gamma radiation doses analysed.

The zeta potential measurements carried out on irradiated and unirradiated samples did not show appreciable changes in this case. At present, the cation exchange capacities of the irradiated samples are being determined since, it has been reported in previous studies that over a certain dose of γ -radiation (>10-20 Gy/h) the bentonite properties might be affected: decreasing CEC and swelling capacity and variation in specific surface area (Allard and Calas 2009; Allard et al., 2012). An eventual change in CEC or on sorption sites may affect the radionuclide retention properties of bentonite. Contradictory results have been obtained on the surface reactivity evolution with radiation (Allard and Calas, 2009; Allard et al, 2012, Allard and Calas 2009).

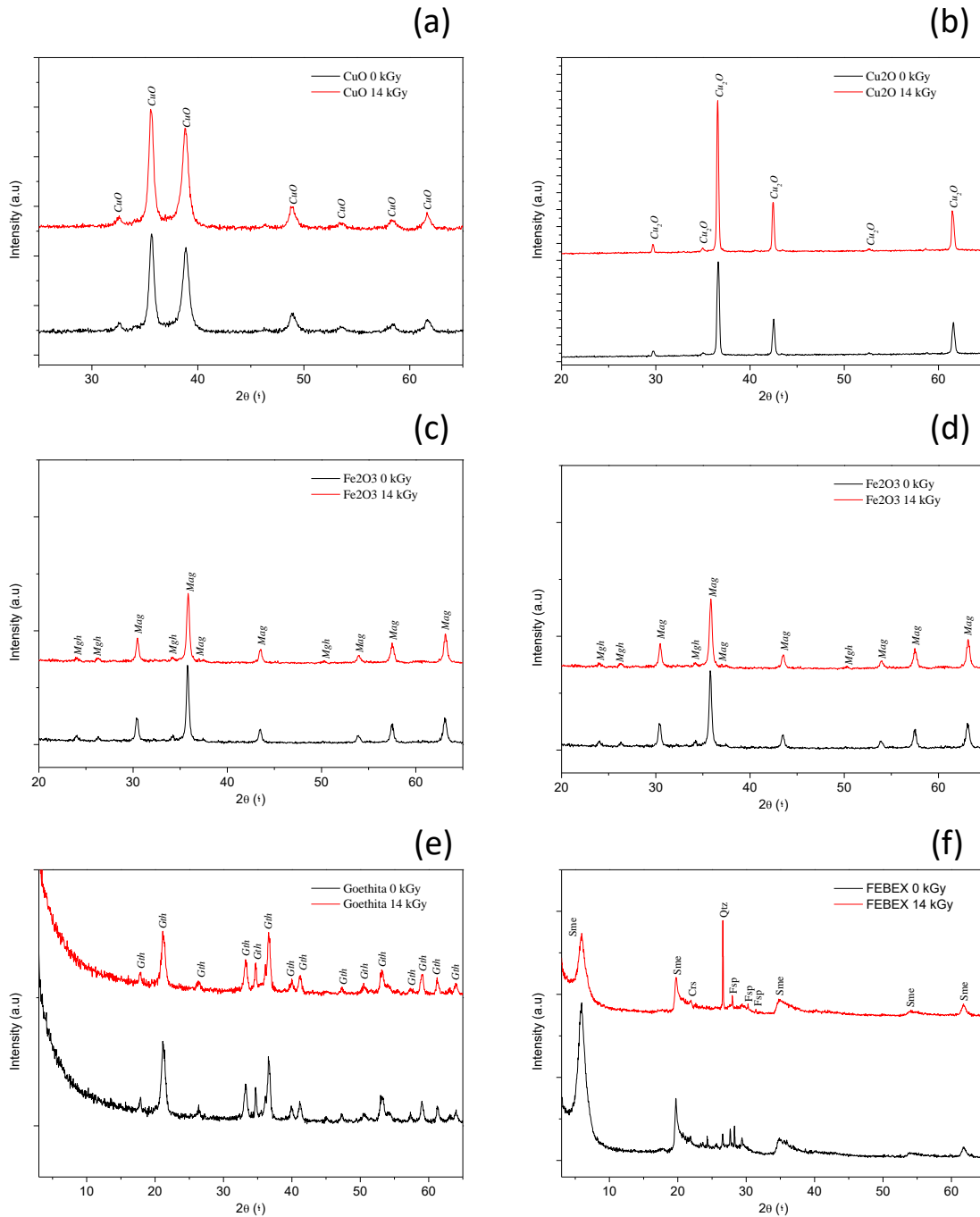


Figure 55 – XRD patterns measured on selected powder Cu and Fe oxides (Table 18) and on FEBEX bentonite, comparing unirradiated powder samples and gamma-irradiated at 14 kGy accumulated dose (dose rate 66 Gy/h).

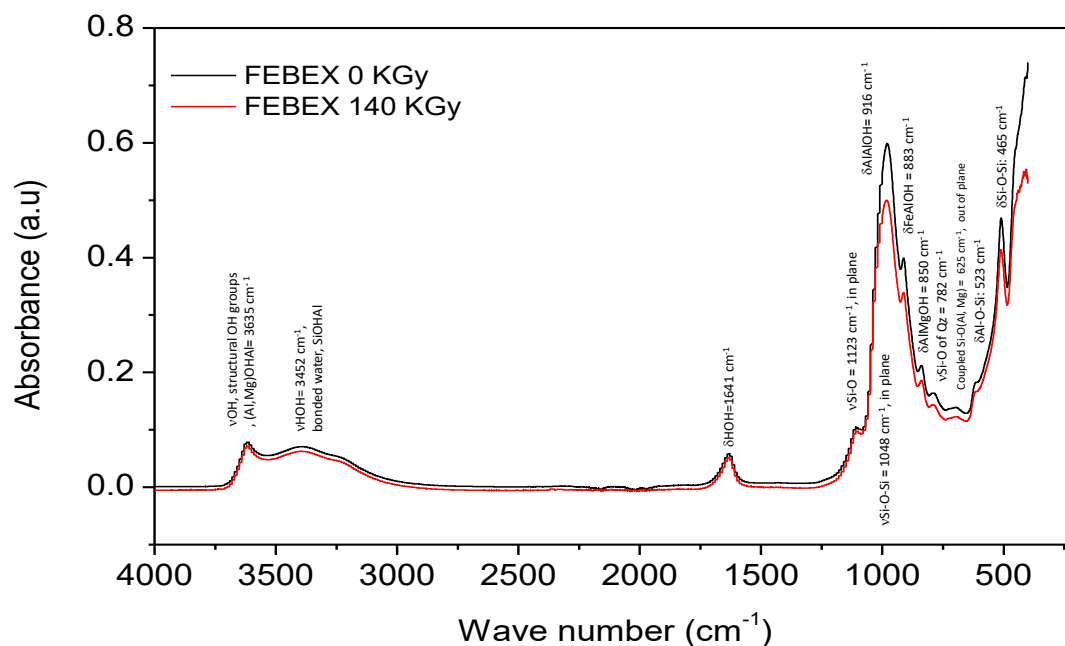


Figure 56 – Comparative FT-IR spectra obtained on powder unirradiated FEBEX bentonite clay and after gamma-irradiation at 140 kGy (dose rate 697 Gy/h). The main bands and groups representative of di-octahedral smectites are indicated.

3.6.2 Metal corrosion in different bentonite porewaters: unirradiated and irradiated

Figure 57 shows the photographs of the Cu-OFP metal discs dismantled after immersion in high saline bentonite porewaters (Section 68) or deionised water under three conditions: (Left) unirradiated, (Middle) gamma irradiated with accumulated dose of 14 kGy and (Right) gamma irradiated, with accumulated dose of 140 kGy. Pictures show the comparison of altered (uncleaned surfaces) and cleaned surfaces for evaluating mass loss. Figure 58 shows the same results but for the C-steel discs.

Table 24 shows the results on corrosion rates estimated by mass loss weighting after cleaning the specimens, considering 12 days of experiment.

Comparatively, the alteration due to water attack was much more pronounced on the C-steel discs than on the Cu-OFP ones, and accordingly the corrosion rates were higher (Table 24).

Cu-OFP showed higher alteration when irradiated compared to unirradiated, but not very big differences were appreciated on irradiated samples (14 and 140 kGy) despite increasing ten times the dose (140 kGy). After cleaning procedure most of the copper discs recovered their initial appearance, indicating low alteration.

In the absence of radiation, the corrosion rate of Cu-OFP was around $\sim 3 \mu\text{m}/\text{y}$, but subjected to gamma-irradiation exposure to 14 and 140 kGy, the corrosion rates increased, but no clear effect increasing the dose was appreciated since in average $\sim 49 \mu\text{m}/\text{y}$ were measured with 14 kGy and $25 \mu\text{m}/\text{y}$ with 140 kGy. Substantial increase in corrosion rate in the presence of radiation is reported in the tests performed by Jacobs (ConCorD Deliverable 15.7, 2024), the lower value measured at higher corrosion rate suggest that the rates are equivalent in our case.

Most of the C-steel discs were covered by an orange layer (Figure 58), attributed to a mixture of Fe(III) oxides, mainly hematite. After cleaning procedure, the surface of the C-steel discs was still altered.

The corrosion rates of C-steel immersed in porewater were higher in the PW 1.6, with slightly higher NaCl content. Unirradiated samples corrosion rates were lower than irradiated, but similar corrosion

rates were measured for C-steel immersed in porewaters during gamma-irradiation exposure to 14 and 140 kGy.

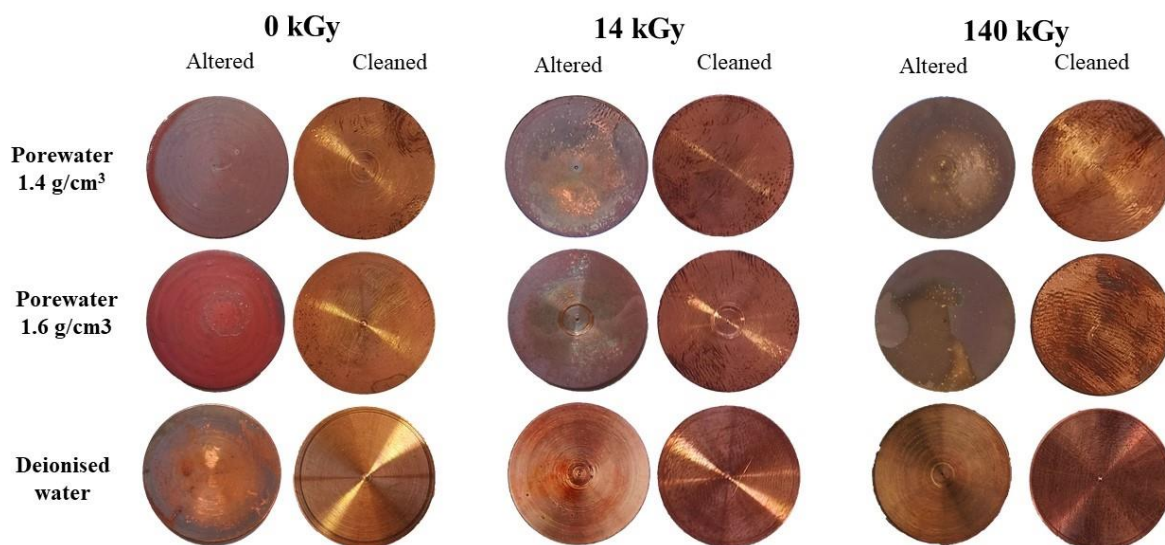


Figure 57 – Appearance of the Cu-OFP metal discs dismantled after immersion in bentonite porewaters (Table 17) and deionised water under three conditions: (Left) unirradiated (middle) gamma irradiated with accumulated dose of 14 kGy and (Right) gamma irradiated with accumulated dose of 140 kGy. Pictures showed the comparison of altered (uncleaned surfaces) and cleaned surfaces for mass loss measurements.

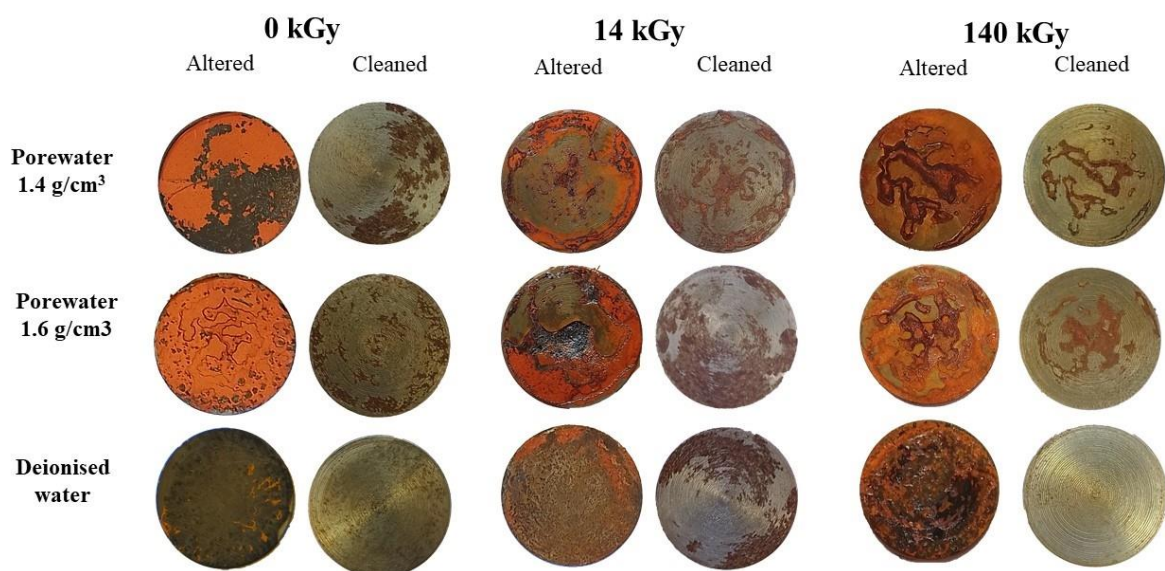


Figure 58 – Appearance of the C-steel metal discs dismantled after immersion in bentonite porewaters (Table 17) and deionised water under three conditions: (Left) unirradiated (middle) gamma irradiated with accumulated dose of 14 kGy and (Right) gamma irradiated with accumulated dose of 140 kGy. Pictures showed the comparison of altered (uncleaned surfaces) and cleaned surfaces for evaluating mass loss measurements.

Table 24 – Corrosion rate determined for Cu-OFP and C-steel discs, immersed in 5 mL different bentonite porewaters (*Table 17*) and deionised water. Samples were unirradiated, irradiated at 14 kGy and irradiated at 140 kGy. Corrosion rates were estimated considering 12 days of experiment and are based on mass loss measurements. (n.d.: not determined)

Irradiation	Sample	Material	Water type	Mass loss (g)	Loss (µm)	Contact time (Days)	Corrosion rate (µm/year)
Unirradiated	T3-19*	Cu-OFP	PW1.4	0.0003 ± 0.0003	0.109	12	3.3
	T3-20*	Cu-OFP	PW1.6	0.0003 ± 0.0003	0.103	12	3.1
	T3-23*	Cu-OFP	DW	0.0005 ± 0.0001	0.174	12	5.3
	T3-21*	C-steel	PW1.4	0.0112 ± 0.0001	4.858	12	147.8
	T3-22*	C-steel	PW1.6	0.0247 ± 0.0002	10.714	12	325.9
	T3-24*	C-Steel	DW	0.0137 ± 0.0002	5.943	12	180.8
Gamma Irradiated 14 kGy (dose rate 66 Gy/h)	T3-19	Cu-OFP	PW1.4	0.0040 ± 0.0013	1.52	12	46.2
	T3-20	Cu-OFP	PW1.6	0.0045 ± 0.0003	1.71	12	51.9
	T3-23	Cu-OFP	DW	n.d.	n.d.	12	n.d.
	T3-21	C-steel	PW1.4	0.0176 ± 0.0005	7.63	12	232.2
	T3-22	C-steel	PW1.6	0.0262 ± 0.0004	11.36	12	345.7
	T3-24	C-Steel	DW	0.0137 ± 0.0003	5.94	12	180.8
Gamma Irradiated 140 kGy (dose rate 697 Gy/h)	T3-33	Cu-OFP	PW1.4	0.0017 ± 0.0005	0.64	12	19.6
	T3-34	Cu-OFP	PW1.6	0.0026 ± 0.0006	0.99	12	30.0
	T3-37	Cu-OFP	DW	0.0006 ± 0.0003	0.23	12	6.9
	T3-35	C-steel	PW1.4	0.0237 ± 0.0001	10.81	12	328.7
	T3-36	C-steel	PW1.6	0.0224 ± 0.0004	9.72	12	295.5
	T3-38	C-Steel	DW	0.0203 ± 0.0003	8.81	12	267.8

The Cu and Fe concentrations measured in solution (unfiltered) after the different irradiation experiments is shown in Figure 59. The concentration of Cu in solution was low in all cases, being lower than that of Fe, in agreement with the higher corrosion measured for C-steel. In both cases, higher Fe and Cu values were measured in solution exposed to higher radiation doses, but measured concentration values in solution were lower than the values obtained from mass loss measurements for both e Cu or Fe , which indicates that most of the oxidized Cu or Fe were precipitated on the surface. It was also interesting that the Fe and Cu concentrations measured in solution after filtering the samples by 0.2 µm filter are very low (> 30 ppm in the case of Fe), which indicates that most of the Cu and Fe present in solution was in particulate form.

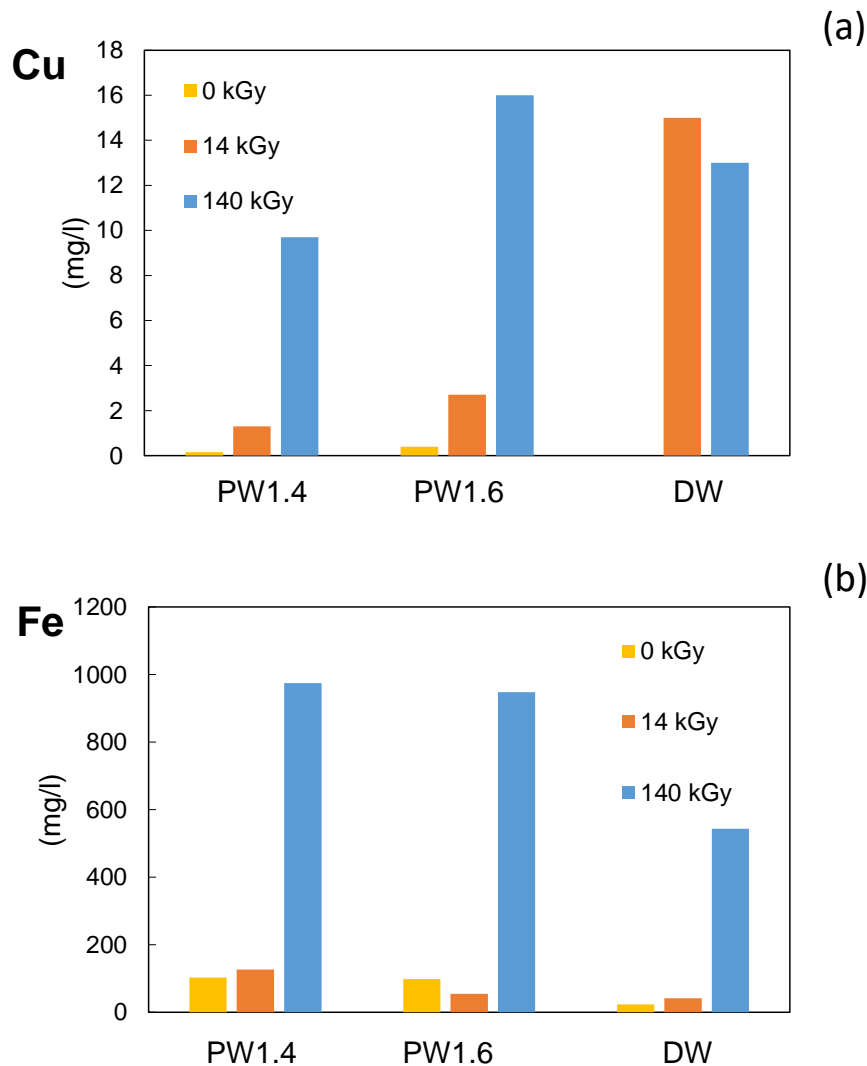


Figure 59 – Metal concentrations measured in unfiltered solution after metal disc immersion in 5 mL of different bentonite porewaters PW1.4 and PW1.6 (Table 17) and in deionised water (DW) irradiated at different conditions (0, 14 kGy and 140 kGy). (a) Cu in solution in mg/l (Cu-OFP experiments) and (b) Fe in solution in mg/l (C-steel experiments).

3.6.3 Magnetite / bentonite samples

The disassembly of closed cells containing a thin surface layer (1-2 mm) of magnetite (Fe₃O₄) over a compacted bentonite samples under different conditions: unirradiated (samples referenced T3-13* to T3-16* in Table 21) or gamma-irradiated with an accumulated dose of 14 kGy (samples referenced T3-

13 to T3-16 in Table 22) was rather complex because the bentonite is compacted, hydrated and confined, so it swells and is stuck to the cell walls, and it is not easy to disassemble.

After irradiation, the upper layer of magnetite oxide appeared very similar to the initial state. The XRD analyses carried out on the oxides after irradiation did not show appreciable differences in respect to the unirradiated magnetite (Mag) (Figure 60), but the presence of bentonite phases is also detected in the contact sample (quartz (Qz), smectite (Sme), feldspar (Fsp), cristobalite (CrS)). Results indicated that overall, no major changes were induced on the whole magnetite layer, and that the impact of 14 kGy gamma dose was very limited to the magnetite /bentonite contact surface.

The surface of the bentonite sample was covered by the oxide, and the colour distribution suggests changes in the magnetite phase to Fe(III) phases, as well to maghemite (Mgh).

No appreciable differences were measured on the samples prepared at different conditions, unirradiated and irradiated, but the quantification of changes and the identification of new phases, promoted by the FEBEX bentonite contact and high-saline porewater presence is being further investigated. The release of corrosion products to the bentonite barrier may have an impact on bentonite overall properties, especially on their retention capability.

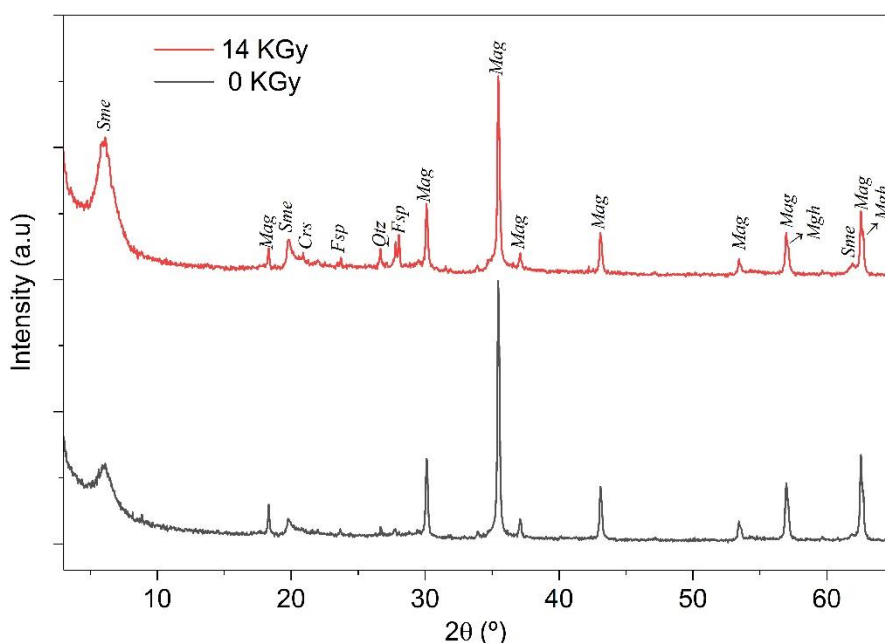


Figure 60 – Comparison of XRD patterns measured on (red) magnetite contacting bentonite compacted sample at 1.4 g/cm³, hydrated at 100% saturation and gamma-irradiated at 14 kGy accumulated dose (dose rate 66 Gy/h) and on (black) unirradiated powder magnetite.

3.6.4 Metal canister /bentonite samples

Figure 61 shows the photographs of the Cu-OFP metal discs dismantled after contact with compacted bentonite at two compaction densities and at two degrees of water saturation, under three conditions: (Left) unirradiated, (middle) Gamma irradiated with accumulated dose of 14 kGy (right) Gamma irradiated with accumulated dose of 14 kGy. Figure 62 shows the same results but for C-steel samples.

Both figures show uncleaned surfaces, photographed after cell disassembly (altered) which include corrosion and alteration products mixed with bentonite. The same surface, after cleaning procedure to estimate corrosion rates by mass loss weighting, is also shown in all cases.

The obtained corrosion rates are gathered in Table 25.

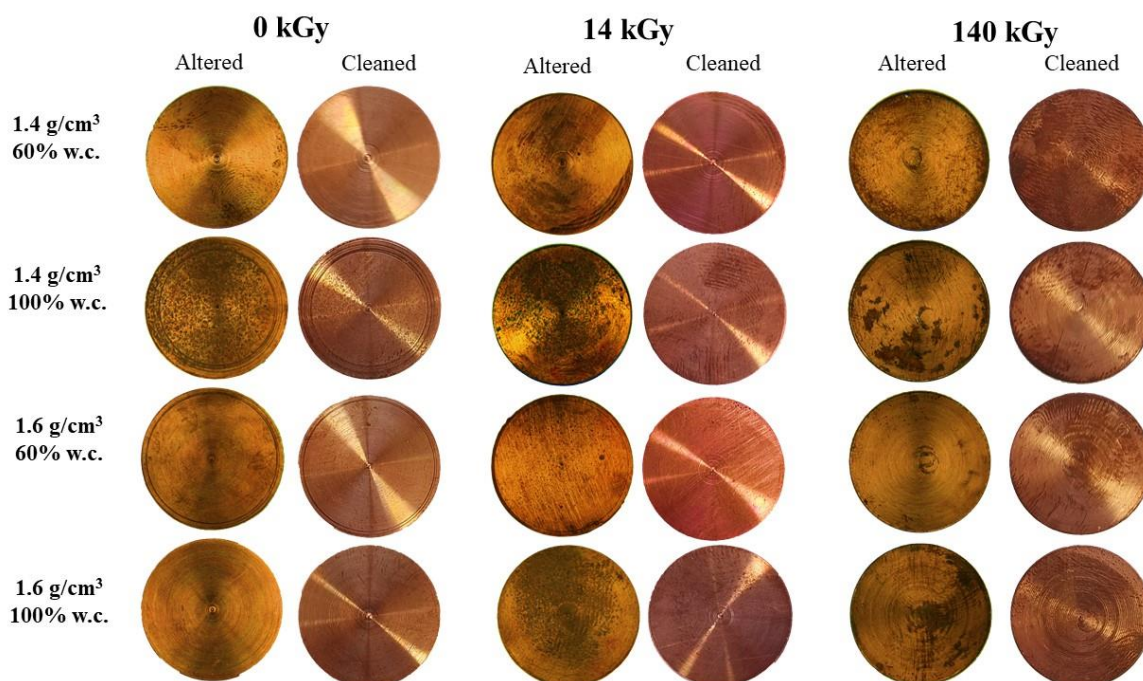


Figure 61 – Appearance of the Cu-OFP metal discs dismantled after contact with compacted bentonite at two compaction densities and with two degrees of water saturation, under three conditions: (Left) Unirradiated, (middle) Gamma irradiated with accumulated dose of 14 kGy ((right) Gamma irradiated with accumulated dose of 140 kGy. . Pictures show the discs altered after opening and later cleaned.

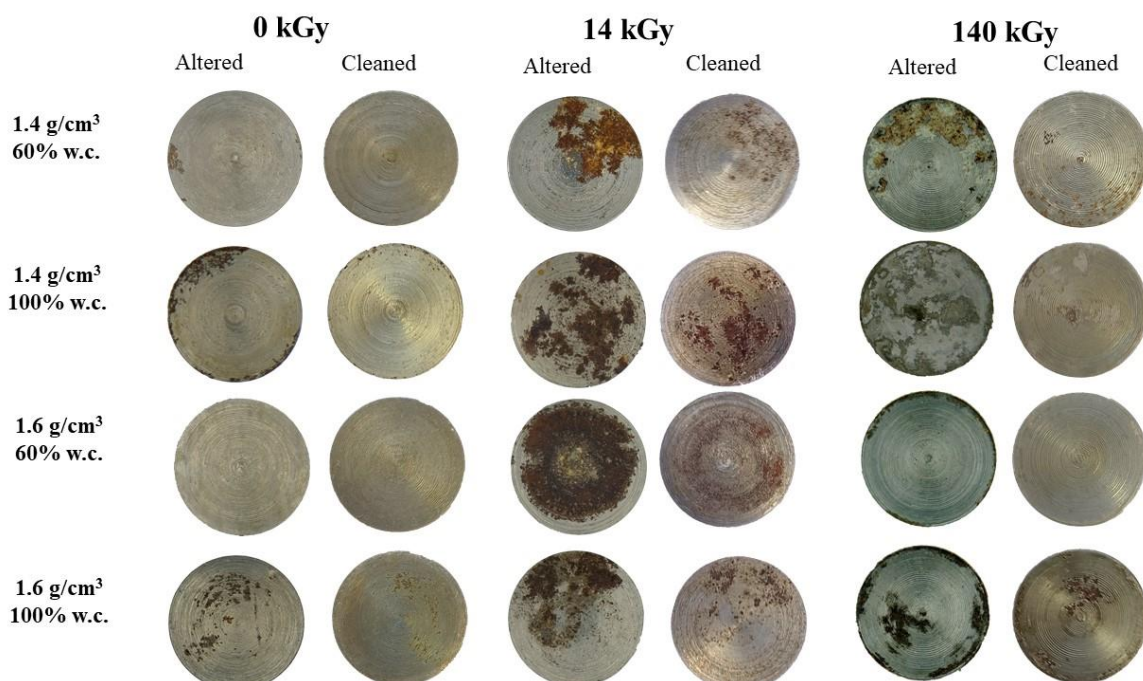


Figure 62 – Appearance of the C-steel metal discs dismantled after contact with compacted bentonite at two compaction densities and with two degrees of water saturation, under three conditions: (Left) Unirradiated, (middle) Gamma irradiated with accumulated dose of 14 kGy ((right) Gamma irradiated with accumulated dose of 140 kGy. . Pictures show the discs altered after opening and later cleaned.

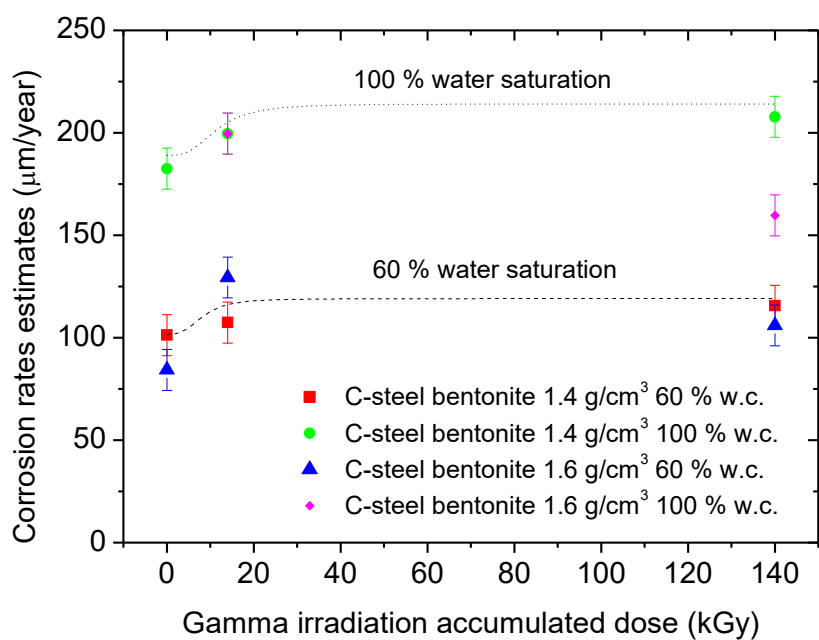


Figure 1. Corrosion rates determined on C-steel samples contacted to FEBEX bentonite compacted samples at two different densities (1.4 and 1.6 g/cm³), hydrated with correspondent porewater at different saturation degree (60 or 100 w.c.%) measured unirradiated or gamma irradiated at 14 kGy or 140 kGy.

Table 25 Corrosion rates determined for Cu-OFP and C-steel discs contacting compacted bentonite samples at two different compaction densities and hydration at two saturation degrees (w.c. %). Triplicate samples were unirradiated, irradiated at 14 kGy and irradiated at 140 kGy. Corrosion rates were estimated considering 12 days of experiment and are based on mass loss measurements.

	Sample	Material	Compaction (g/cm ³)	% water content	Mass loss (g)	Loss (µm)	Contact time (days)	Corrosion rate (µm/year)
Unirradiated	T3-05*	Cu-OFP	1.4	60%	0.0019 ± 0.0003	0.721	12	21.9
	T3-06*	Cu-OFP	1.4	100 %	0.0006 ± 0.0001	0.228	12	6.9
	T3-07*	Cu-OFP	1.6	60%	0.0001 ± 0.0002	0.038	12	1.2
	T3-08*	Cu-OFP	1.6	100 %	0.0000 ± 0.0004	0.000	12	0.0
	T3-09*	C-steel	1.4	60%	0.0071 ± 0.0003	3.080	12	93.7
	T3-10*	C-steel	1.4	100 %	0.0132 ± 0.0004	5.726	12	174.2
	T3-11*	C-steel	1.6	60%	0.0061 ± 0.0005	2.646	12	80.5
	T3-12*	C-steel	1.6	100 %	0.0111 ± 0.0006	4.815	12	146.4
Unirradiated Gamma Irradiated 14 kGy (dose rate 66 Gy/h)	T3-05	Cu-OFP	1.4	60%	0.0004 ± 0.0007	0.15	12	4.4
	T3-06	Cu-OFP	1.4	100 %	0.0004 ± 0.0002	0.14	12	4.4
	T3-07	Cu-OFP	1.6	60%	0.0004 ± 0.0001	0.15	12	4.5
	T3-08	Cu-OFP	1.6	100 %	0.0004 ± 0.0004	0.14	12	4.1
	T3-09.1	C-steel	1.4	60%	0.0078 ± 0.0006	3.38	12	102.9
	T3-10.1	C-steel	1.4	100 %	0.0145 ± 0.0002	6.29	12	191.3
	T3-11.1	C-steel	1.6	60%	0.0094 ± 0.0003	4.08	12	124.0
	T3-12.1	C-steel	1.6	100 %	0.0145 ± 0.0001	6.29	12	191.3
Gamma Irradiated 140 kGy (dose rate 697 Gy/h)	T3-25	Cu-OFP	1.4	60%	0.0000 ± 0.0003	0.00	12	0.0
	T3-26	Cu-OFP	1.4	100 %	0.0002 ± 0.0006	0.08	12	2.3
	T3-27	Cu-OFP	1.6	60%	0.0000 ± 0.0006	0.00	12	0.0
	T3-28	Cu-OFP	1.6	100 %	0.0000 ± 0.0007	0.00	12	0.0
	T3-29	C-steel	1.4	60%	0.0084 ± 0.0005	3.64	12	110.8
	T3-30	C-steel	1.4	100 %	0.0151 ± 0.0002	6.55	12	199.2
	T3-31	C-steel	1.6	60%	0.0077 ± 0.0007	3.34	12	101.6
	T3-32	C-steel	1.6	100 %	0.0116 ± 0.0005	5.03	12	153.0

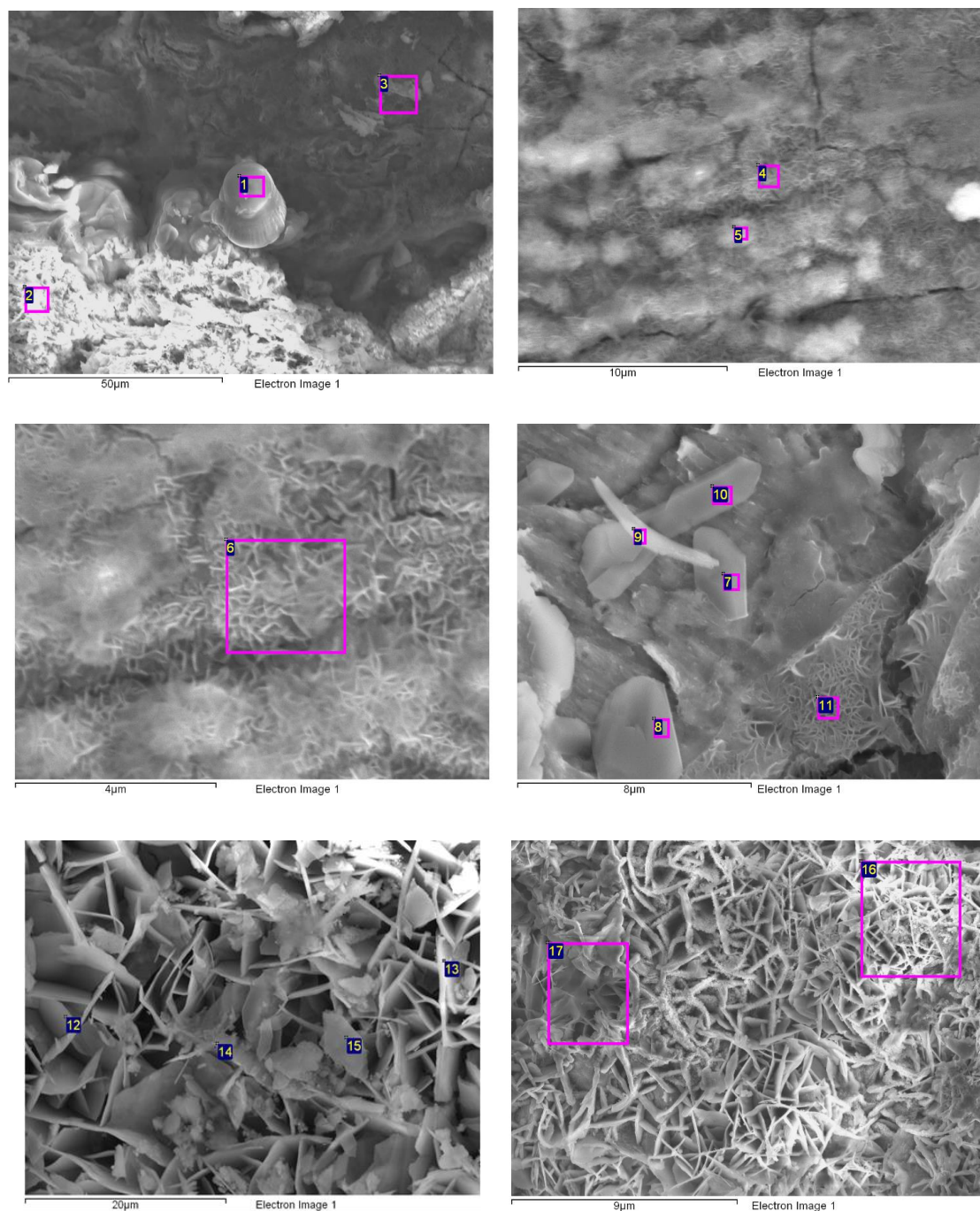


Figure 63 Example of SEM images obtained on the surface of a C-steel disc of experiment reference T3-10, which corresponds to a sample contacted to compacted bentonite at 1.4 g/cm³ and 100% water content, irradiated at 14 kGy, where higher corrosion rate was measured. The number in the images are areas analysed by EDAX.

Once again, the alteration of Cu-OFP specimens was very limited compared to that of C-steel samples. The higher corrosion rates were measured in C-steel discs contacting bentonite samples at lower compaction density (1.4 g/cm³) and with higher degree of water saturation. This indicates that the high salinity of the porewater is the main corrosive agent in the system. In fact, higher corrosion rates were even measured on the samples directly immersed in the porewater (Table 24).

Higher corrosion rates were measured on irradiated C-steel samples, compared to unirradiated ones, but no differences are measured between the two irradiation doses investigated (14 kGy and 140 kGy).

SEM, FTIR and RAMAN studies were carried out on both metal samples (uncleaned) and on the bentonite contact surface to identify the alteration products.

Very little material is appreciated on the Cu-OFP disc surfaces, but the main corrosion products were identified as Cu(II) oxides.

Figure 59 shows an example of SEM images obtained on the surface of C-steel disc of experiments (T3-10), which corresponds to a sample contacted by compacted bentonite at 1.4 g/cm³ and 100% water content, irradiated at 14 kGy, where higher corrosion rate was measured. Very different phases are identified on the surface, showing a mixture of Fe-phases and bentonite minerals, as well as precipitated salts. EDXA analyses indicated presence of Fe-Cl phases, Ca-Fe phases, as well as Fe oxides, mixed with residual bentonite particles (suggested by the presence of Si, Al, Mg and Ca).

The nature of alteration products was very similar on all C-steel coupons contacted to compacted bentonite samples under different conditions.

The main Fe-phases identified by RAMAN spectroscopy were hematite, goethite and ferrihydrite. Figure 2 shows an example of measured RAMAN spectra on a bentonite compacted sample (experiment reference T3-12), corresponding to a sample with a C-steel disc contacting a compacted bentonite sample at 1.6 g/cm³ and 100 % hydrates. It can be appreciated that the RAMAN spectrum of the corroded product released from the C-steel fits with that of goethite.

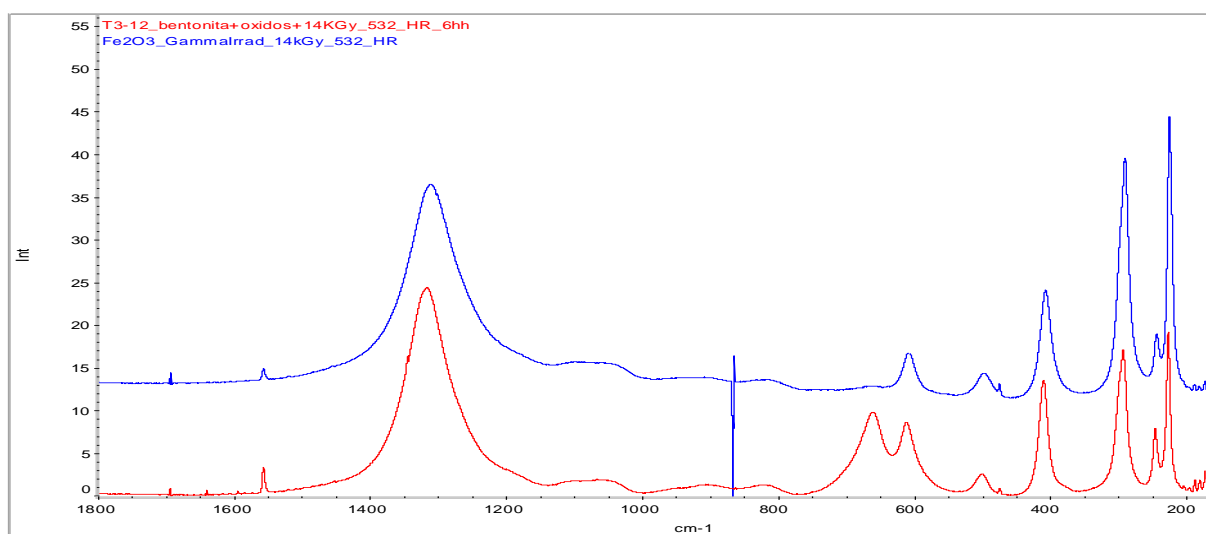


Figure 64 Comparative RAMAN spectra obtained on the bentonite surface of sample T3-12, corresponding to a C-steel disc contacting a compacted bentonite sample at 1.6 g/cm³ and 100 % hydrates. The spectra fits with that of a goethite sample measured at the same conditions.

3.6.5 Irradiated compacted bentonite samples (no metal)

Finally, the state of the compacted bentonite samples after irradiation was also analysed (not including metal discs) but exposed to gamma-radiation (14 kGy or 140 kGy) was analysed by XRD and FT-IR.

Figure 2 shows the XRD patterns measured on compacted bentonite samples at two compaction densities irradiated at 14 kGy. No changes on bentonite mineralogy or structure were detected on irradiated bentonite samples.

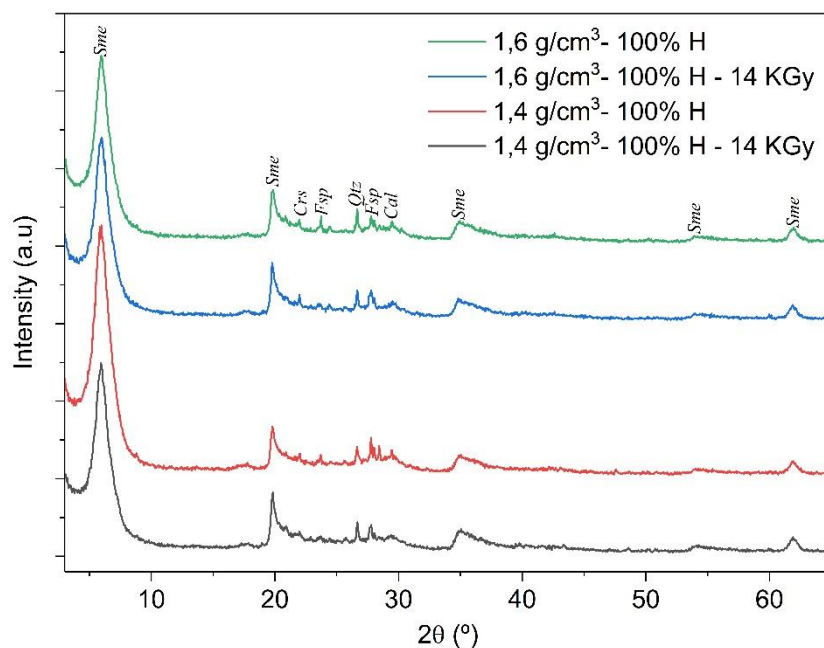


Figure 65 Comparative XRD patterns measured on bentonite samples which were irradiated in compacted state (14 or 1.6 g/cm³) and full water saturated.

3.7 Summary and conclusions by CIEMAT

CIEMAT carried out experiments to analyse the impact of gamma irradiation on different samples simulating the canister / bentonite interface of a deep geological repository within the framework of Task 3 - ConCorD.

CIEMAT experiments were designed to simulate canister/bentonite interface, considering a representative repository scenario at the early stage in which bentonite is not fully water saturated, gamma irradiation accumulated dose is around 14 kGy and conditions are still aerobic, usually defined as Phase 2 – Aerobic unsaturated phase (oxic and unsaturated conditions).

CIEMAT carried out irradiation experiments during short times considering two main cases: (I) Copper and C-steel coupons immersed in synthetic representative bentonite porewaters. and (2) copper or C-steel coupons contacting compacted bentonite samples at two compaction densities (1.4 and 1.6 g/cm³) and hydrated with each corresponding synthetic porewater at two water saturation conditions (w.c. 60% or 100 %), for comparison.

Compacted bentonite samples with a thin surface layer of Fe-oxide (Fe₃O₄) were analysed to investigate the impact of irradiation on released corrosion products. In parallel, reference samples were used to better elucidate key processes induced by gamma radiation: Iron and copper powder oxides (relevant corrosion products) and powdered bentonite.

All CIEMAT samples were prepared in triplicate to consider (i) unirradiated conditions, (ii) gamma radiation at accumulated dose of 14 kGy and (iii) gamma radiation at accumulated dose of 140 kGy.

CIEMAT results corroborated the limited corrosion of copper specimens compared to that of C-steel ones. In general, higher corrosion rates were measured on gamma-irradiated C-steel samples contacting bentonite at lower compaction density where higher volume of porewater is available. Higher corrosion rates were measured in irradiated than in unirradiated samples but no significant changes in corrosion rates were detected for irradiated samples achieving 14 or 140 kGy of accumulated dose, suggesting an inhibiting effect at higher doses.

References

- Allard, Th, E. Balan, G. Calas, C. Fourdrin, E. Morichon, and S. Sorieul. 2012. "Radiation-Induced Defects in Clay Minerals: A Review." *Nuclear Instruments and Methods in Physics Research, Section B: Beam Interactions with Materials and Atoms* 277:112–20. doi: 10.1016/j.nimb.2011.12.044.
- Allard, Th, and G. Calas. 2009. "Radiation Effects on Clay Mineral Properties." *Applied Clay Science* 43(2):143–49. doi: 10.1016/j.clay.2008.07.032.
- Ammann L., Bergaya F., Lagaly G. 2005. Determination of the Cation Exchange Capacity of Clays with Copper Complexes Revisited. *Clay Min.* 40: 441–453, doi:10.1180/0009855054040182.
- ASTM, 2011. ASTM-G1: Standard Practice for Preparing, Cleaning, and Evaluating Corrosion Test Specimens. ASTM International, West Conshohocken, PA, USA.
- Bergmann J., Friedel P., Kleeberg R. 1998. BGMN – a new fundamental parameters-based Rietveld program for laboratory X-ray sources, its use in quantitative analysis and structure investigations. *CPD Newsl. (Commission of Powder Diffraction, International Union of Crystallography)* 20: 5–8
- Bergmann J., Monecke T., Kleeberg R. 2001. Alternative algorithm for the correction of preferred orientation in Rietveld analysis. *J. Appl. Crystallogr.* 34: 16 - 19
- Červinka R., Gondolli J., Havlová V., Rukavičková L. 2016. Selection of representative groundwater and preparation of its synthetic equivalents (in Czech). SURAO Technical report no. 41/2016, SURAO, Prague, Czech Republic.
- Červinka R., Vašíček R., Večerník P., Kašpar V. 2018. SÚRAO report no. 419/2019: Complete characterization of the BCV 2017 bentonite (in Czech). SURAO, Prague, Czech Republic.
- ConCorD Deliverable 15.7 (2024). Clayton Bevas (Jacobs), James Hesketh (Jacobs), Andy Rance (Jacobs), Leigh-Anne Stevenson (Jacobs), Shorubhi Uthayakumaran (Jacobs) Ben Pateman (Jacobs), Cristiano Padovani (Jacobs), Šárka Šachlová (UJV), Vlastislav Kašpar (UJV), David Dobrev (UJV), Daniel Götz (UJV), Kateřina Kolomá (UJV), Petr Večerník (UJV). (2024): Elucidation of the effect of radiation on the corrosion of canister materials. Final version as of 06/02/2024 of deliverable D15.7 of the HORIZON 2020 project EURAD. EC Grant agreement no: 847593.
- ConCorD Deliverable 15.9 (2024). Impact of irradiation, bentonite dry density and particle size on the microbial community. Final version of deliverable D15.9 of the HORIZON 2020 project EURAD. EC Grant agreement no: 847593.
- ConCorD Deliverable 15.12 (2024). Identification of the effect of transient processes on corrosion. Final version of deliverable D15.9 of the HORIZON 2020 project EURAD. EC Grant agreement no: 847593.
- ČSN 75 7373 (757373) Water quality - Calculation of carbon dioxide forms (species). Czech Normalization Institute
- ČSN EN 10210-1 Hot finished structural hollow sections of non-alloy and fine grain steels - Part 1: Technical delivery conditions. Czech Normalization Institute
- Degen T., Sadki M., König E. U., Nénert G. 2014. The HighScore suite. *J. Pow. Diff.* 29 (sup.S2): S13-S18, doi: 10.1017/S0885715614000840
- Döbelin N., Kleeberg R. 2015 Profex: a graphical user interface for the Rietveld refinement program BGMN. *J. Appl. Cryst.* 48: 1573-1580. doi:10.1107/S1600576715014685
- Duro, L., Bruno, J., Grivé, M., Montoya, V., Kienzler, B., Altmaier, M., Buckau, G., 2014. Redox processes in the safety case of deep geological repositories of radioactive wastes. Contribution of the European RECOZY Collaborative Project. *Applied Geochemistry* 49, 206-217.
- EURAD Milestone MS.264. Revision of existing data for the selection of Cu and Fe-corrosion products. (2021). ConCord project. Authored A.M. Fernandez, U. Alonso.

- Ebert, W. L., Hoburg, R. F., & Bates, J. K. (1991). The sorption of water on obsidian and a nuclear waste glass. *Physics and chemistry of glasses*, 32(4), 133-137.
- Fernandez, A.M., Rivas, P. (2005). Pore water chemistry of saturated FEBEX bentonite compacted at different densities. *Advances in Understanding Engineered Barriers*. Alonso & Ledesma (eds). Taylor and Francis Group, London. Pp 505- 514 ISBN 04-1536-544-9 (2005).
- Fernández, A.M.; Sánchez-Ledesma, D.M.; Melón, A.; Robredo, L.M.; Rey, J.J.; Labajo, M.; Clavero, M.A.; Fernández, S.; González, A.E., 2018. Thermo-hydro-chemical (THC) behaviour of a Spanish Bentonite after dismantling Heater#1 and Heater#2 of the FEBEX in situ test at the Grimsel Test Site. *Nagra Working Reports*. NAB 16-25, 583 pp. NAGRA, 2018.
- Frankl, M., Wittel, M., Diomidis, N., Vasiliev A., Ferroukhi H., Pudollek S. (2023) Criticality assessments for long-term post-closure canister corrosion scenarios in a deep geological repository. *Annals of Nuclear Energy Volume 180*, January 2023, 109449.
- Heuser M. (2018) The interaction between bentonite and water vapor. Ph.D. thesis. RWTH Aachen University, Aachen, Germany.
- Hofmanová E., Červinka R., Vopálka D., Baborová L., Brázda L., Pecková A., Vetešník A., Viglašová E., Vašíček R. (2019): Transport of radionuclides from a repository / Input parameters and process models for evaluation of radionuclide transport across engineering barriers: Final report of the project. Technical report no.. 420/2019, SÚRAO, Prague, Czech Republic.
- Huertas, F., Fariña, P., Farias, J., García-Siñeriz, J.L., Villar, A.M., Fernández, A.M., Martín, P.L., Elorza, F.J., Gens, A., Sánchez, M., Lloret, A., Samper, J., Martínez, M.A., 2006. FEBEX Project. Full-scale engineered barriers experiment for a deep geological repository for high level radioactive waste in crystalline host rock. Updated Final Report 1994-2004. Technical Publication ENRESA 5-0/2006, 590 pp. Madrid.
- Hunter, R. J., Ottewill, R. H., & Rowell, R. L. (2013). *Zeta Potential in Colloid Science*. Elsevier Gezondheidszorg.
- ICSD database FIZ Karlsruhe, Germany, release 2022/2, 2022
- Inoue A., Velde B., Meunier A., Touchard G. 1988. Mechanism of illite formation during smectite to illite conversion in a hydrothermal system. *Am. Miner.* 73: 1325–1334
- King F. 2008. Corrosion of carbon steel under anaerobic conditions in a repository for SF and HLW in Opalinus Clay, Nagra Technical Report 08-12, Nagra, Switzerland.
- King, F., Padovani, C., 2011. Review of the corrosion performance of selected canister materials for disposal of UK HLW and/or spent fuel. *Corrosion Engineering, Science and Technology*, 46, 82-90.
- Kloprogge, J.T. 2005. The application of vibrational spectroscopy to clay minerals and layered double hydroxides. *CMS Workshop Lectures 13*. The Clay Minerals Society. 285 pp.
- Landolt, D., Davenport, A., Payer, J., & Shoosmith, D. (2009). Review of Materials and Corrosion Issues Regarding Canisters for Disposal of Spent Fuel and High-level Waste. Opalinus Clay. Nagra Technical Report 09-02.
- Little, J., Lee, J.S. (2007) *Microbiologically Influenced Corrosion*. Wiley Series in Corrosion. John Wiley and Sons, Inc., Hoboken, N.J.
- Madejová, J., Komadel, P., 2001. Baseline studies of the Clay Minerals Society Source Clays: Infrared methods. *Clays and Clay Minerals* 49, pp. 410-432.
- Madsen F.T. (1998): Clay mineralogical investigations related to nuclear waste disposal. *Clay Miner.* 33? 109–129
- Malaret, F., & Yang, X. S. (2022). Exact calculation of corrosion rates by the weight-loss method. *Experimental Results*, 3, e13.

- Meier L.P., Kahr G. 1999. Determination of the Cation Exchange Capacity (CEC) of Clay Minerals Using the Complexes of Copper(II) Ion with Triethylenetetramine and Tetraethylenepentamine. *Clays Clay Miner.* 47: 386–388, doi:10.1346/CCMN.1999.0470315.
- Missana, T., Alonso, U., Scheinost, A.C., Granizo, N., Garcia—Gutierrez, M. (2009)- Selenite retention by nanocrystalline magnetite: Role of adsorption, reduction and dissolution/co-precipitation processes. *Geochimica et Cosmochimica Acta* 73, 6205–6217
- Mosser-Ruck R., Cathelineau M., Baronnet A., Trouiller A. 1999. Hydrothermal reactivity of K-smectite at 300 C and 100 bar: dissolution–crystallisation process and non-expandable dehydrated smectite formation. *Clay Miner.* 34: 275–290.
- NACE, A. (2012). Standard guide for laboratory immersion corrosion testing of metals. ASTM Int., 1-9.
- Necib,, T., S., Diomidis, N., Keech, P. & Nakayama, M. (2017): Corrosion of carbon steel in clay environments relevant to radioactive waste geological disposals, Mont Terri rock laboratory (Switzerland). *Swiss Journal of Geosciences*, 110, 329-342.
- Neff D., Saheb M., Monnier J., Perrin S., Descostes M., LHostis V., Crusset D., Millard A., Dillmann P. 2010. A review of the archaeological analogue approaches to predict the long-term corrosion behaviour of carbon steel overpack and reinforced concrete structures in the French disposal systems, *J. Nucl. Mat.* 402: 196-205
- O'brien, F. E. M. (1948). The control of humidity by saturated salt solutions. *Journal of Scientific Instruments*, 25(3), 73.
- Patel, R., Punshon, C., Nicholas, J., Bastid, P., Zhou, R. C., Schneider, N., Bagshaw, D., Howse, E., Hutchinson, R., Asano, and F. King (2012). “Canister Design Concepts for Disposal of Spent Fuel and High Level Waste, Technical Report, NTB 12-06, Nationale Genossenschaft für die Lagerung radioaktiver Abfälle (Nagra), Wettingen, Switzerland.
- PDF-4+ database, International Centre for Diffraction Data, Newtown Square, PA, U.S.A. release 2023.
- Pitzer, K. S., Bradley, D. J., Rogers, P. S. Z., & Peiper, C. (1979). Thermodynamics of high temperature brines.
- Pospiskova I., Dobrev D., Kouril M., Stouilil J., Novikova D., Kotnour P., Matal O. 2017. Czech national programme and disposal canister concept. *Corrosion Engineering, Science and Technology* 52(sup.1): 6-10, DOI: 10.1080/1478422X.2017.1300379
- Pusch R., Karnland O. 1988. Hydrothermal effects on montmorillonite. A preliminary study. SKB Technical Report 88-15, Svensk Kärnbränslehantering AB, Stockholm, Sweden.
- Pusch R., Kasbohm J., Thao H.T.M. 2010. Chemical stability of montmorillonite buffer clay under repository-like conditions—A synthesis of relevant experimental data. *Appl. Clay Sci.* 47: 113–119
- Rietveld H.M. 1969. A profile refinement method for nuclear and magnetic structures, *J. Appl. Crystallogr.* 2: 65-71
- Robira, M. (2018). Propriétés physico-chimiques et comportement différé des matériaux cimentaires sous irradiations gamma (Doctoral dissertation, Ecole nationale supérieure Mines-Télécom Atlantique).
- Roy W. R. 1993. Adsorption-Desorption Methodologies and Selected Estimation Techniques for Transport-Modeling Parameters. Migration and Fate of Pollutants in Soils and Subsoils. In: (Petruzzelli D., Helfferich F.G., Eds.) NATO ASI Series G 32: 169–188, doi:10.1007/978-3-642-77862-9_8
- Saheb, M., Marsal, F., Matthiesen, H., Neff, D., Dillmann, P., Pellegrini, D., 2011. Fluctuation of redox conditions in radioactive waste disposal cell: characterisation of corrosion layers formed on archaeological analogues. *Corrosion Engineering, Science and Technology* 46, 199-204. doi.org/10.1179/1743278210Y.0000000006
- Schulthess CP, Sparks DL. 1986. Backtitration technique for proton isotherm modeling of oxide surfaces. *Soil Sci. Soc. Am. J.* 50:1406–1411.

- Smart N. R., Rance A., Reddy B., Fennell P., Winsley R. 2012. Analysis of SKB MiniCan Experiment 3. SKB TR-12-09, Svensk Kärnbränslehantering AB, Stockholm, Sweden.
- Smart, N.R., Reddy, B., Rance, A.P., Nixon, D.J., Fritschi, M., Bernier-Latmani, R. & Diomidis, N. (2017): The anaerobic corrosion of carbon steel in compacted bentonite exposed to natural Opalinus Clay porewater containing native microbial populations. *Corrosion Engineering Science and Technology*, 52 S1 (2017) 101-112.
- SoTA, 2021. ConCorD Deliverable 2.1: State-of-the-art Report of the HORIZON 2020 project EURAD. EC Grant agreement no: 847593.
- Stoulil J., Kaňok J., Kouřil M., Parschová H., Novák P. 2013. Influence of temperature on corrosion rate and porosity of corrosion products of carbon steel in anoxic bentonite environment. *J. Nucl. Mat.* 443(1–3): 20-25, DOI:10.1016/j.jnucmat.2013.06.031.
- Tarafter, P.K., Thakur, R., 2012. An optimised 1,10-Phenanthroline method for the determination of ferrous and ferric oxides in silicate rocks, soils and minerals. *Geostandards and Geoanalytical research* 37, pp. 155-168.
- Ufer K., Stanjek H., Roth G., Dohrmann R., Kleeberg R., Kaufhold S. 2008. Quantitative phase analysis of bentonites by the rietveld method. *Clays Clay Min.* 56: 272–282.
- Van der Marel, H.W., Beutelspacher, H., 1976. Atlas of infrared spectroscopy of clay minerals and their mixtures. Elsevier, Amsterdam, 396 pp.
- Wersin, P., Kober, F., 2017. FEBEX-DP. Metal Corrosion and Iron-Bentonite Interaction Studies. Nagra Working Report NAB 16-016.
- Young, J. F. (1967). Humidity control in the laboratory using salt solutions—a review. *Journal of Applied Chemistry*, 17(9), 241-245.
- Zuna M., Steinová J., Šachlová Š., Dobrev D., Mendoza Miranda A. N., Kolomá K., Kašpar V., Jankovský F., Večerník P. (2023): Corrosion test in natural granitoid environment – involvement in the MaCoTe project. Final report. SURAO Technical report no. 712/2023, SÚRAO, Prague, Czech Republic.

Appendix

A.1 Subatech samples

A.1.1 Steel alone samples

Sample Code	Sample Configuration	Temperature (°C)	Relative Humidity (%)	Atmosphere	Total Dose (kGy)	Cell Number	Dose Rate	Irradiation time (days)	Estimated Real Dose Received (kGy)
F 46	S	25	Ambient	Argon	100	B12	412	10.00	98.81
F 47	S	25	Ambient	Argon	100	B12	412	10.00	98.81
L 11	S	25	Ambient	Argon	50	B12	412	10.00	98.81
L 19	S	25	Ambient	Argon	50	B12	412	10.00	98.81
L 20	S	25	Ambient	Argon	200	23	474	20.00	227.33
L 25	S	25	Ambient	Argon	200	23	474	20.00	227.33
F 17	S+Sol	25	63	Argon	200	2	360	21.00	181.29
F 18	S+Sol	25	63	Argon	200	2	360	21.00	181.29
F 19	S+Sol	25	76	Argon	200	8	403	21.00	202.96
F 20	S+Sol	25	76	Argon	200	8	403	21.00	202.96
F 21	S+Sol	25	99	Argon	200	1	349	21.00	175.64
F 22	S+Sol	25	99	Argon	200	1	349	21.00	175.64
F 23	S+Sol	25	63	Argon	400	25	411	42.00	414.59
F 24	S+Sol	25	63	Argon	400	25	411	42.00	414.59
F 33	S+Sol	25	63	Argon	50	2	360	10.00	86.33
F 34	S+Sol	25	63	Argon	50	2	360	10.00	86.33
F 36	S+Sol	25	76	Argon	50	8	403	10.00	96.65
F 37	S+Sol	25	76	Argon	50	8	403	10.00	96.65
F 38	S+Sol	25	99	Argon	50	1	349	10.00	83.64
F 39	S+Sol	25	99	Argon	50	1	349	10.00	83.64
F 40	S+Sol	25	63	Argon	100	2	360	10.00	86.33
F 41	S+Sol	25	63	Argon	100	2	360	10.00	86.33
F 42	S+Sol	25	76	Argon	100	8	403	10.00	96.65
F 43	S+Sol	25	76	Argon	100	8	403	10.00	96.65
F 44	S+Sol	25	99	Argon	100	1	349	10.00	83.64
F 45	S+Sol	25	99	Argon	100	1	349	10.00	83.64
F 72	S+Sol	25	76	Argon	400	5	421	39.00	393.59
F 73	S+Sol	25	76	Argon	400	5	421	39.00	393.59
F 74	S+Sol	25	99	Argon	400	G12	471	36.00	407.03
F 75	S+Sol	25	99	Argon	400	G12	471	36.00	407.03
F 80	S+Sol	25	76	Air	100	B8	429	9.00	92.64
F 82	S+Sol	25	76	Air	100	B8	429	9.00	92.64
F 94	S+Sol	25	63	Air	100	B7	386	13	120.49
F 95	S+Sol	25	63	Air	100	B7	386	13	120.49
F 96	S+Sol	25	63	Air	50	B8	429	5	51.47
F 97	S+Sol	25	63	Air	50	B8	429	5	51.47
F 98	S+Sol	25	63	Air	200	22	398	21	200.59
F 99	S+Sol	25	63	Air	200	22	398	21	200.59

A.1.2 Steel+clay samples

Sample Code	Sample Configuration	Temperature (°C)	Relative Humidity (%)	Atmosphere	Total Dose (kGy)	Cell Number	Dose Rate	Irradiation time (days)	Estimated Real Dose Received (kGy)
F 1	S+C+Sol	25	63	Argon	100	25	366	12.00	105.44
F 2	S+C+Sol	25	63	Argon	100	25	366	12.00	105.44
F 3	S+C+Sol	25	63	Argon	100	25	366	12.00	105.44
F 4	S+C+Sol	25	76	Argon	100	5	471	9.00	101.76
F 5	S+C+Sol	25	76	Argon	100	5	471	9.00	101.76
F 6	S+C+Sol	25	76	Argon	100	5	471	9.00	101.76
F 8	S+C+Sol	25	99	Argon	100	4	398	9.00	85.97
F 9	S+C+Sol	25	99	Argon	100	4	398	9.00	85.97
F 10	S+C+Sol	25	63	Argon	50	22	366	7.00	61.50
F 11	S+C+Sol	25	63	Argon	50	22	366	7.00	61.50
F 12	S+C+Sol	25	76	Argon	50	5	398	7.00	66.86
F 13	S+C+Sol	25	99	Argon	100	4	398	9.00	85.97
F 14	S+C+Sol	25	76	Argon	50	5	398	7.00	66.86
F 15	S+C+Sol	25	99	Argon	50	4	471	7.00	79.14
F 16	S+C+Sol	25	99	Argon	50	4	471	7.00	79.14
F 27	S+C+Sol	25	76	Argon	400	5	421	42.00	423.86
F 28	S+C+Sol	25	76	Argon	400	5	421	42.00	423.86
F 29	S+C+Sol	25	99	Argon	400	G12	471	42.00	474.87
F 30	S+C+Sol	25	99	Argon	400	G12	471	42.00	474.87
F 31	S+C+Sol	25	63	Argon	400	22	398	42.00	401.18
F 32	S+C+Sol	25	63	Argon	400	22	398	42.00	401.18
F 48	S+C+Sol	25	63	Argon	200	23	411	23.00	227.04
F 49	S+C+Sol	25	63	Argon	200	23	411	23.00	227.04
F 50	S+C+Sol	25	76	Argon	200	5	421	23.00	232.12
F 51	S+C+Sol	25	76	Argon	200	5	421	23.00	232.12
F 52	S+C+Sol	25	99	Argon	400	G12	471	37.00	418.34
F 53	S+C+Sol	25	99	Argon	400	G12	471	37.00	418.34
F 54	S+C+Sol	25	99	Argon	200	22	398	23.00	219.70
F 55	S+C+Sol	25	99	Argon	200	22	398	23.00	219.70
F 56	S+C+Sol	25	63	Argon	100	23	411	14.00	138.20
F 57	S+C+Sol	25	63	Argon	100	23	411	14.00	138.20
F 58	S+C+Sol	25	76	Argon	100	5	421	14.00	141.29
F 59	S+C+Sol	25	76	Argon	100	5	421	14.00	141.29
F 60	S+C+Sol	25	99	Argon	100	22	398	14.00	133.73
F 61	S+C+Sol	25	99	Argon	100	22	398	14.00	133.73
F 76	S+C+Sol	25	H2O (~100%)	Argon	200	22	398	21.00	200.59
F 77	S+C+Sol	25	H2O (~100%)	Argon	200	22	398	21.00	200.59
F 81	S+C+Sol	25	76	Air	100	B7	386	9.00	83.42
F 83	S+C+Sol	25	76	Air	100	B7	386	9.00	83.42

A.1.3 Unirradiated reference samples

Sample Code	Sample Configuration	Temperature (°C)	Relative Humidity (%)	Atmosphere	Target Dose Equivalent (kGy)	Starting Date	End Date	Exposure time (days)
F 25	S+C+Sol	25	99	Argon	400	31/07/2023	11/09/2023	42.00
F 35	S+C+Sol	25	99	Argon	400	31/07/2023	11/09/2023	42.00
F 62	S+C+Sol	25	63	Argon	400	13/10/2023	24/11/2023	42.00
F 63	S+C+Sol	25	63	Argon	400	13/10/2023	24/11/2023	42.00
F 64	S+C+Sol	25	76	Argon	400	13/10/2023	24/11/2023	42.00
F 65	S+C+Sol	25	76	Argon	400	13/10/2023	24/11/2023	42.00
F 66	S+C+Sol	25	99	Argon	200	13/10/2023	08/11/2023	26.00
F 67	S+C+Sol	25	99	Argon	200	13/10/2023	08/11/2023	26.00
F 68	S+C+Sol	25	63	Argon	200	27/10/2023	22/11/2023	26.00
F 69	S+C+Sol	25	63	Argon	200	27/10/2023	22/11/2023	26.00
F 70	S+C+Sol	25	76	Argon	200	27/10/2023	22/11/2023	26.00
F 71	S+C+Sol	25	76	Argon	200	27/10/2023	22/11/2023	26.00
F 78	S+C+Sol	25	99	Argon	100	09/11/2023	20/11/2023	11.00
F 79	S+C+Sol	25	99	Argon	100	09/11/2023	20/11/2023	11.00
F 84	S+C+Sol	25	99	Argon	100	20/11/2023	01/12/2023	11
F 85	S+C+Sol	25	99	Argon	100	20/11/2023	01/12/2023	11
F 86	S+Sol	25	63	Argon	400	23/11/2023	04/01/2024	42
F 87	S+Sol	25	63	Argon	400	23/11/2023	04/01/2024	42
F 88	S+Sol	25	99	Argon	400	23/11/2023	04/01/2024	42
F 89	S+Sol	25	99	Argon	400	23/11/2023	04/01/2024	42
F 90	S+Sol	25	63	Argon	200	24/11/2023	20/12/2023	26
F 91	S+Sol	25	63	Argon	200	24/11/2023	20/12/2023	26
F 92	S+Sol	25	99	Argon	200	24/11/2023	20/12/2023	26
F 93	S+Sol	25	99	Argon	200	24/11/2023	20/12/2023	26
F 100	S+Sol	25	63	Air	200	01/12/2023	12/01/2024	42
F 101	S+Sol	25	63	Air	200	01/12/2023	12/01/2024	42